

## Towards estimation of optical and structural ophthalmic properties based on optical coherence tomography

Ghafaryasl, B.

**DOI**

[10.4233/uuid:71f02179-f4e9-4c51-a2a4-945b9679a857](https://doi.org/10.4233/uuid:71f02179-f4e9-4c51-a2a4-945b9679a857)

**Publication date**

2021

**Document Version**

Final published version

**Citation (APA)**

Ghafaryasl, B. (2021). *Towards estimation of optical and structural ophthalmic properties based on optical coherence tomography*. [Dissertation (TU Delft), Delft University of Technology].  
<https://doi.org/10.4233/uuid:71f02179-f4e9-4c51-a2a4-945b9679a857>

**Important note**

To cite this publication, please use the final published version (if applicable).  
Please check the document version above.

**Copyright**

Other than for strictly personal use, it is not permitted to download, forward or distribute the text or part of it, without the consent of the author(s) and/or copyright holder(s), unless the work is under an open content license such as Creative Commons.

**Takedown policy**

Please contact us and provide details if you believe this document breaches copyrights.  
We will remove access to the work immediately and investigate your claim.

Towards estimation of optical and  
structural ophthalmic properties based on  
optical coherence tomography



# Towards estimation of optical and structural ophthalmic properties based on optical coherence tomography

PROEFSCHRIFT

ter verkrijging van de graad van doctor  
aan de Technische Universiteit Delft,  
op gezag van de Rector Magnificus Prof.dr.ir. T.H.J.J. van der Hagen,  
voorzitter van het College voor Promoties,  
in het openbaar te verdedigen op woensdag 16 juni 2021 om 12:30 uur

door

**Babak GHAFARYASL**

Master of Science in Electrical Engineering  
Linnaeus University, Zweden  
geboren te Tehran, Iran.

Dit proefschrift is goedgekeurd door de  
Promotor: Prof.dr.ir. L.J. van Vliet  
Copromotor: Dr.ir. K.A. Vermeer

Samenstelling promotiecommissie:

Rector Magnificus,	voorzitter
Prof.dr.ir. L.J. van Vliet,	Technische Universiteit Delft, promotor
Dr.ir. K.A. Vermeer,	Rotterdam Ophthalmic Institute, copromotor

Onafhankelijke leden:

Prof.dr.ir. R. Benedictus,	Technische Universiteit Delft
Prof.dr. A. Gh. Podoleanu,	University of Kent
Dr. M.E.J. van Velthoven,	Oogziekenhuis Rotterdam
Prof.dr. S. Stallinga,	Technische Universiteit Delft

Overig lid:

Prof.dr. J.F. de Boer,	Vrije Universiteit Amsterdam
------------------------	------------------------------



The work in this thesis was conducted at the Imaging Physics (ImPhys), Faculty of Applied Sciences, Delft University of Technology, and at The Rotterdam Ophthalmic Institute (R.O.I).

This research was funded by the Netherlands Organization for Health Research and Development (ZonMw) TOP grant (91212061).

Cover design: Plot of a Gaussian beam by Etoombs at en.wikipedia under the Creative Commons Attribution 3.0 Unported license.

Printed by: Ipskamp Drukkers

ISBN: 978-94-6421-385-0

Copyright © 2021 by Babak Ghafaryasl

A digital copy can be downloaded from [repository.tudelft.nl](https://repository.tudelft.nl).

Printing of this thesis was kindly sponsored by: Stichting Wetenschappelijk Onderzoek Oogziekenhuis (SWOO) Prof. Dr. H.J. Flieringa

# Contents

1	Introduction .....	9
1.1	Human eye anatomy .....	10
1.2	Retinal anatomy .....	11
1.3	An introduction to OCT systems.....	12
1.4	Challenges in this Thesis.....	14
1.4.1	Attenuation coefficient .....	15
1.4.2	Retinal nerve fibre bundle orientation .....	16
1.5	Thesis outline.....	16
2	Quantitative forward model of spectral-domain optical coherence tomography	
	21	
2.1	Introduction .....	21
2.2	Method .....	22
2.2.1	Method A: The recorded OCT signal in a SD-OCT system .....	22
2.2.2	Method B: A simple model of the OCT signal .....	28
2.3	Experiments .....	28
2.3.1	Measurements .....	28
2.3.2	Simulation.....	33
2.4	Conclusion.....	37
3	Noise-Adaptive attenuation coefficient in spectral domain optical coherence tomography data.....	41
3.1	Introduction .....	42
3.2	Methods.....	45
3.2.1	Subtracting the average noise signal (Method B) .....	45
3.2.2	Excluding the noise region (Method C).....	45
3.2.3	Evaluation of different methods.....	45

3.3	Experiments and results .....	46
3.3.1	Removing the average noise signal (method B).....	47
3.3.2	Excluding the noise region (method C) .....	47
3.3.3	Evaluation of the methods.....	48
3.4	Conclusion.....	49
	References.....	51
4	Analysis of attenuation coefficient estimation in Fourier-domain OCT of semi-infinite media.....	53
4.1	Introduction .....	54
4.2	Method.....	56
4.2.1	Estimating the model parameters.....	56
4.2.2	Model selection and evaluation.....	57
4.3	Results .....	59
4.3.1	Model selection by Cramér-Rao analysis .....	59
4.3.2	Experiment design by Cramér-Rao analysis .....	61
4.3.3	Estimation accuracy and precision: Monte Carlo simulation .....	63
4.3.4	Experimental setup.....	65
4.3.5	Estimating the model parameters using multiple B-Scans.....	68
4.4	Discussion.....	69
	References.....	71
5	Attenuation coefficient estimation in Fourier-domain OCT of multi-layered phantoms.....	75
5.1	Introduction .....	76
5.2	Method and experiments .....	77
5.2.1	Estimating the model parameters.....	78
5.2.2	Simulation of OCT signal and Monte Carlo simulation.....	80
5.2.3	Phantom experiments.....	81

5.3	Results .....	83
5.4	Discussion.....	95
	References.....	97
6	Automatic estimation of retinal nerve fibre bundle orientation in SD-OCT images using a structure-oriented smoothing filter.....	101
6.1	Introduction .....	102
6.2	Method.....	102
6.3	Experiments and results .....	106
6.4	Conclusion.....	109
	References.....	109
7	Conclusion and future work.....	111
8	Summary.....	115
9	Publications.....	117
10	Acknowledgments.....	119
11	Curriculum Vitae .....	121



# 1 Introduction

---

The human eye is a light-sensitive organ enabling us to sense and observe our surroundings. Partial or complete blindness caused by vision disorders is among one of the worst disabilities. Ophthalmic photography technologies were first developed to enable exploring the human eye and later to assist ophthalmologists in early diagnosis of eye diseases. The history of ophthalmic photography leads back to the late 18<sup>th</sup> century when the first human fundus camera was invented in 1886 [1]. Throughout the next 60 years there had been a slow progress in instrumentation and techniques, due to several technical limitations such as ‘slow’ photographic films, long exposure times and weak light sources. By 1950’s, modern ophthalmology was born with the development of digital cameras and advancements in electronics, laser light sources and optics [2]. Later, several technologies such as the tonometer, visual field test, laser ophthalmoscopy and optical coherence tomography (OCT) were developed for the diagnosis of eye diseases such as glaucoma. These systems in combination with the quantitative information from the tissue help the ophthalmologists and researchers to have a better understanding of structural and functional properties of the human eye. In this thesis, we will introduce new techniques enabling us to obtain a better quantitative description of the various tissues composing the retina using OCT data. For this aim, we will first improve the estimation of the attenuation coefficient of the sample under investigation by taking into account the optical properties of the OCT systems, and later extract the structural properties of the retinal tissues. Our techniques may be used in combination with others for monitoring longitudinal changes in retinal tissue and diagnosis of diseases such as glaucoma.

## 1.1 Human eye anatomy

The human eye is a light-sensitive organ that provides us with colour vision and depth perception (Fig. 1.2). Light passes through the transparent cornea, which acts as a lens providing about two-thirds of the total light refraction. The refracted light passes through aqueous fluid and enters the pupil. The iris controls the amount of light entering the eye by adaptively adjusting the size of the pupil. Behind the pupil one finds the lens, which provides about a third of the refractive power of the eye and focuses the light on the retina using adaptive accommodation of its curvature. The space between the lens and retina is filled with a gel-like substance called vitreous.

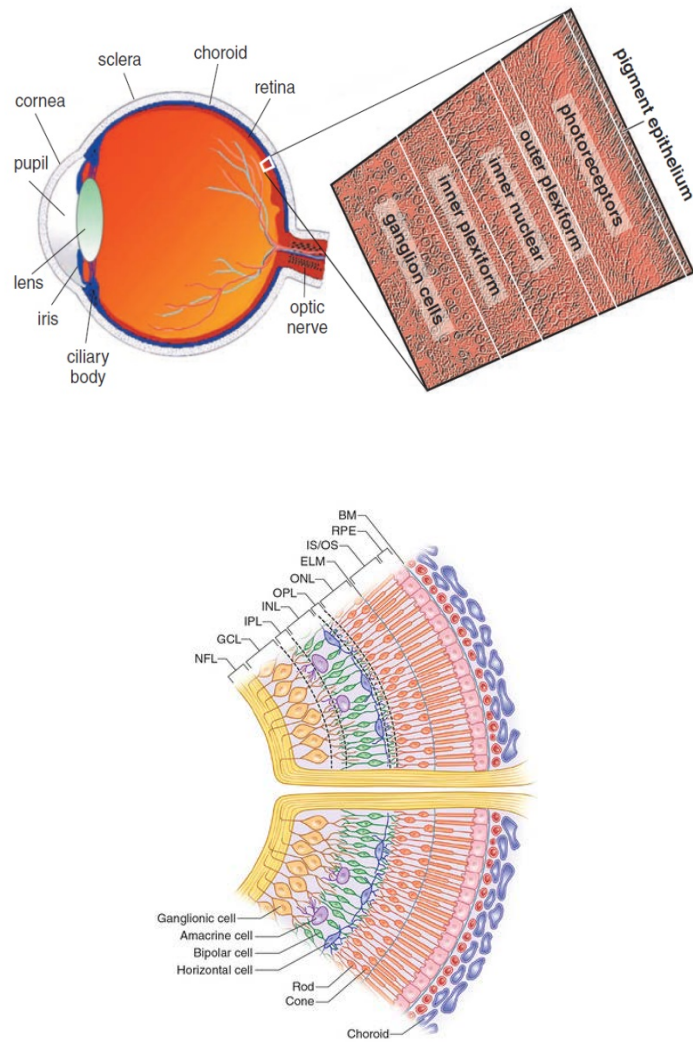


Figure 1.1 General anatomy of the eye and retinal nerve fibre layer [3].

The back of the eye consists of the retina, choroid and sclera. The retina is the innermost layer and consists of two types of photoreceptors, which convert the detected light energy into electrical signals and subsequent neural activity. The functional centre of the retina, where the light is focused on by the cornea and lens, is called macula. Our central vision as well as the ability to see details is provided by the macula, whereas the other locations of the retina provide us with peripheral vision. In the centre of the macula is the fovea, which consists of a high concentration of cones responsible for colour vision and visual acuity when there is a relatively high brightness of incoming light. The optic nerve head (ONH) is depicted by a depression in the retina, located 3-4 mm to the nasal side of the fovea, with an average dimension of 1.7 mm vertically and 1.9 mm horizontally [2]. The received electrical signals from the retina are transferred to the brain through the ONH by the ganglion cell axons, which form the optic nerve after leaving the eye.

Adjacent to retina lays the choroid which is a dense network of vessels and supplies nutrition to the posterior of the retina. Adjacent to the choroid lays the sclera, which is an opaque and protective tissue layer, mainly consisting of collagen.

## **1.2 Retinal anatomy**

The human retina has an average thickness of 0.5 mm and consists of several layers (Fig. 1.1). These layers are laid from the innermost to the outermost retina accordingly: the nerve fibre layer (NFL); the ganglion cell layer (GCL); the inner plexiform layer (IPL); the inner nuclear layer (INL); the outer plexiform layer (OPL); the outer nuclear layer (ONL); the external limiting membrane (ELM); photoreceptor inner/outer segment (IS/OS); the retinal pigmented epithelium (RPE) monolayer; and Bruch's membrane (BM). The retinal NFL (RNFL) consists of nerve fibres, blood vessels, Müller cells and collagen. The nerve fibres are unmyelinated axons of the ganglion cells coursing parallel to the surface of the retina to the optic disk. The thickness of the RNFL is the highest around the ONH where all the fibres accumulate. The distribution of the nerve fibres is shown in Fig. 1.2. The macula contains a large number of fibres and the papillomacular bundles radiate from the macula area to the ONH. The arcuate fibres located on the

temporal periphery arc around the papillomacular bundle and do not cross the temporal raphe. The larger retinal arteries lie in the RNFL, just beneath the ILM. These arteries give rise to a network of capillaries located in the RNFL and ganglion cell layer. The Müller cells and collagen form the architectural support and maintain the structural stability of the retina.

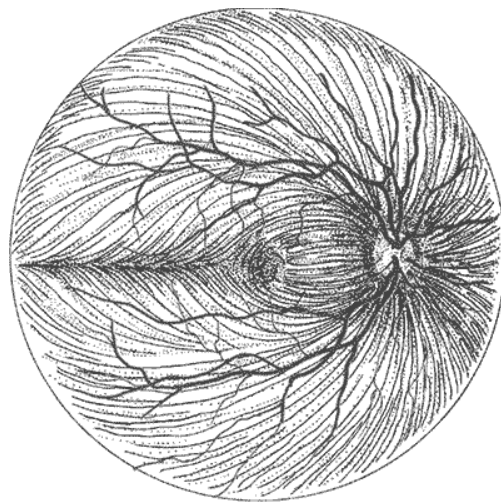


Figure 1.2 Distribution of the retinal nerve fibres superimposed on the main vasculature of the retina [4].

OCT data can be used to provide ophthalmologists with both structural and optical properties of the RNFL. In the last decade, there has been a great interest in using OCT data for the diagnosis of chorioretinal diseases such as glaucoma. The thickness of the RNFL has been used as a biomarker for diagnosis of glaucoma [5-7]. Recently, the use of optical properties of retinal tissues has received interest for early diagnosis of glaucoma [8-10].

### 1.3 An introduction to OCT systems

OCT uses the concept of interferometry to generate in vivo microscopic images of biological tissues. The first in vivo OCT images of retina were acquired in 1993 [11]. In

1996, OCT systems became commercially available, and clinical usage of OCT accelerated when Humphrey Zeiss technology presented the third-generation systems in 2002 [12].

A simplified schematic overview of various OCT systems is shown in Fig. 1.3. Early OCT systems employed the so-called time-domain (TD) OCT principle [13], a technique based on a low-coherence light source using an interferometer with a scanning reference arm to provide depth information. A beamsplitter divides the incoming beam from the light source between the reference arm and sample arm of the interferometer. The reference light beam from source transmits towards a translational mirror located at a certain distance from the beamsplitter. The light in the sample arm propagates into the sample under investigation. The backscattered light from the sample will interfere with the reflected light from the reference arm and is detected at the detector. The interference occurs when the delay between the sample and reference arms beams is within the coherence length [14]. The OCT detector measures the intensity of the interference as a function of depth into the sample by moving the translational mirror; hence forming a so-called A-line.

The advent of Fourier domain (FD) OCT systems provides us with a higher acquisition speed and sensitivity compared to TD-OCT [15,16]. In these systems, the reflectance along a depth profile is measured for a range of wavelengths simultaneously. This could be achieved in two ways: (1) using a broadband light source and a spectrometer consisting of a diffraction grating in *Spectral-domain* (SD) OCT or (2) using a standard photodetector and a wavelength-swept laser in *Swept-source* (SS) OCT [17,18]. A simple illustration of SD-OCT and SS- OCT systems is shown in Fig. 1.4. SS-OCT uses a frequency-swept narrow linewidth laser, which makes the system less sensitive to fringe washouts by sample movement [19] and improves the signal to noise (SNR) [20] compared to SD-OCT. In the next section, we will briefly explain the scope and challenges of this thesis.

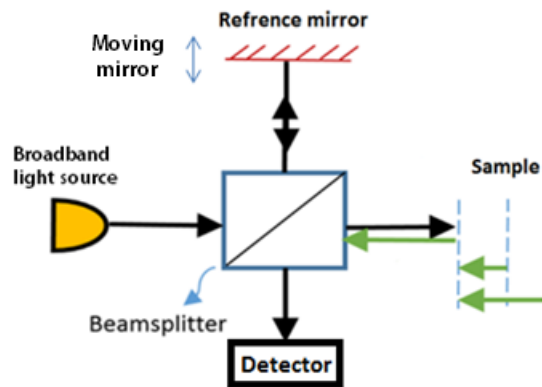


Figure 1.3 A simplified illustration of a TD-OCT system.

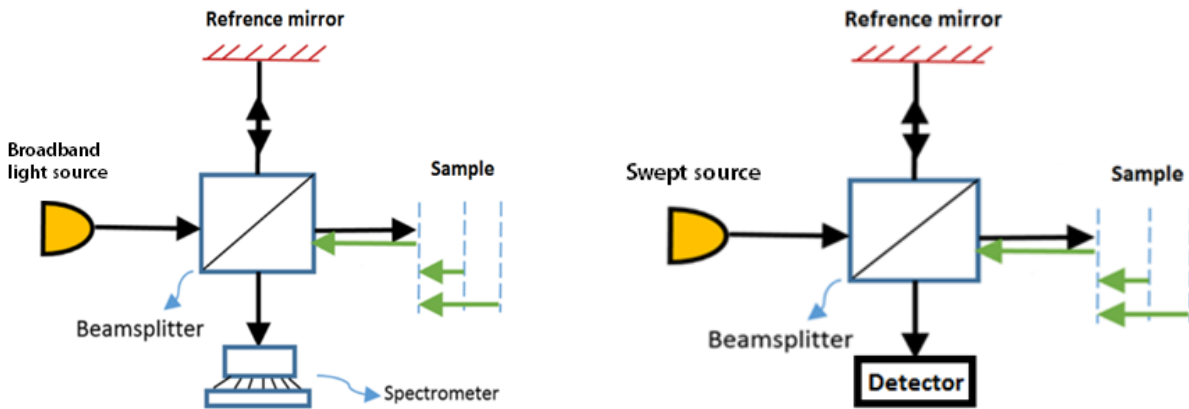


Figure 1.4 Simplified schematic overviews of SD-OCT (left) and SS-OCT (right) systems.

## 1.4 Challenges in this Thesis

The main focus of this thesis is to obtain an unbiased and precise estimate of the attenuation coefficient of retinal tissue by taking into account the optical characteristics of the OCT systems. The attenuation coefficient is an optical property of the tissue and a potential biomarker for the diagnosis and monitoring of chorioretinal diseases [5,6].

In addition, the structural information of the retinal nerve fibre bundles may be used as additional information to the existing methods, i.e. visual field, for diagnosis of RNFL pathologies such as glaucoma. In this section, we will explain the challenges with regard to

the space-variant estimation of the attenuation coefficient in the retinal layers and the necessity of extracting the structural information of retina.

#### 1.4.1 Attenuation coefficient

The intensity of the incident OCT light attenuates while penetrating inside the eye and reaching the tissue layers composing the retina. The backscattered light also attenuates on its way back to the detector. Therefore, OCT images do not fully represent the real characteristics and scattering properties of the tissues. To solve this issue and to obtain a meaningful quantitative analysis of the OCT signal we can model the interaction of light and tissue, resulting in a model-based estimation of the attenuation coefficient. The attenuation coefficient as an optical property of the tissue offers valuable information that can be estimated from the intensity of the OCT signal and provides ophthalmologist with a quantitative measurement to identify the variations of the tissues caused by different chorioretinal diseases such as glaucoma. An accurate estimation of the attenuation coefficients will result in a better understanding of tissue characteristics.

##### *Estimation of the attenuation coefficient*

Several methods have been developed for estimating the attenuation coefficient based on either single [21-24] or multiple [25,26] scattering of light. For all methods that estimate the attenuation coefficient, the OCT signal must be corrected for the depth-dependent noise floor and the depth-dependent signal decay caused by discrete signal detection and resolution limitations of the detection process [27,24]. Compensation for noise and roll-off is nowadays a standard procedure. In the method proposed by Vermeer et al. [24], we observed that excessive image noise below the retina might cause both an underestimation and a significant variation of the estimated attenuation coefficients within and between A-lines. In this work we proposed a method to improve the accuracy of the estimated attenuation coefficients by excluding the noise region.

In addition, in this work, we aim to achieve an accurate estimate of attenuation coefficient by compensating for the effect of the axial point spread function (PSF) on the recorded OCT signal [26]. This approach estimates the axial PSF model parameters and attenuation coefficient by fitting a single scattering model to the recorded OCT signal as obtained from a homogenous sample. Since the retinal tissue has a layered structure, we

will present an extension of our estimation method to multi-layer samples. The method is evaluated by the measurements obtained from a multi-layer sample.

#### **1.4.2 Retinal nerve fibre bundle orientation**

The loss of retinal nerve fibre bundles (RNFB) is a sign of damage to the optic nerve and hence of subsequent loss of vision. Visual field (VF) examination and standard automated perimetry (SAP) have been used widely for diagnosis of the glaucomatous eyes. Hood et al. [29] have shown that in an early stage of glaucoma there is asymmetry of visual field defects where the inferior VF is weaker than the superior one. However, VF data is noisy and not reproducible. Tracing the RNFBs can improve the reliability of the VF data and helps to have an early diagnosis of retinal diseases such as glaucoma [29-32].

Manual tracing of these bundles is a tedious task; therefore, several methods have been developed to estimate RNFB trajectory [33-38]. These methods are based on automatic tracing of RNFBs in fundus images [33,34] or mathematical modelling with parameter fitting [30,35-38]. In this work, we present an automatic technique to estimate the orientation of RNFBs from volumetric OCT scans.

### **1.5 Thesis outline**

The main objective of this thesis is to provide an unbiased and precise estimation of the optical and of the structural properties of the RNFL to facilitate the diagnosis of retinal diseases such as glaucoma. To achieve the first objective, we aim to improve the estimation of the attenuation coefficient by improving and extending existing methods. To achieve the second objective we will investigate the estimation of the nerve fibre orientation from OCT data.

In Chapter 2, two methods are used to simulate an OCT signal by taking into account the shape of the OCT beam. The methods are compared with each other and with actual OCT measurements. The most suitable method is subsequently used in simulations and model-based estimations.

Chapter 3 of this thesis addresses an improvement to an existing method for estimating the attenuation coefficient by detecting and removing the noise regions in the OCT B-Scan. The approach was demonstrated on two normal eyes.

In Chapter 4 a method is presented to estimate the axial PSF model parameters and attenuation coefficient by fitting the selected model in Chapter 3 to the recorded OCT signal as obtained from a homogenous sample. In addition, we employ statistical analysis to obtain the theoretical optimal precision of the estimated parameters for different experimental setups with various systems and sample specifications. The approach was evaluated on the measurements of a single layer phantom.

In Chapter 5 we present an extension of our estimation method to multi-layer samples. The method is evaluated by the measurements obtained from a multi-layer sample by two OCT systems with different Rayleigh lengths.

Chapter 6 describes an automatic technique to estimate the orientation of retinal nerve fibre bundles (RNFB) of the RNFL from volumetric OCT scans. The RNFB orientations of six macular scans from three subjects were used to demonstrate the method.

Finally, the conclusion and scientific contents of this thesis are summarised in Chapters 7 and 8.

## References

- [1] T. Jackman, J. D. Webster, "Photographing the Eye of the Living Human Retina," Photographic News, England, 1886.
- [2] A. Chan, J. S. Duker, T. H. Ko, et al., "Normal macular thickness measurements in healthy eyes using Stratus optical coherence tomography," *Arch Ophthalmol.* **124**, 193-198 (2006).
- [3] <http://www.retinareference.com/anatomy/>.
- [4] W. L. M. Alward, "Glaucoma: the requisites in ophthalmology," Krachmer J. H (Ed). St. Louis: Mosby, 4 (2000)

- [5] J. S. Schuman, M. R. Hee, C. A. Puliafito, et al. “Quantification of nerve fibre layer thickness in normal and glaucomatous eyes using optical coherence tomography,” *Arch Ophthalmol.* **113**, 586-596 (1995).
- [6] J. C. Mwanza, J. L. Warren, D. L. Budenz, “Combining spectral domain optical coherence tomography structural parameters for the diagnosis of glaucoma with early visual field loss,” *Invest. Ophthalmol. Vis. Sci.* **54**, 8393-8400 (2013).
- [7] J. M. Larrosa, J. Moreno-Montanes, J. M. Martinez-de-la-Casa, et al. “A diagnostic calculator for detecting glaucoma on the basis of retinal nerve fibre layer, optic disc, and retinal ganglion cell analysis by optical coherence tomography,” *Invest Ophthalmol Vis Sci.* **56**, 6788-6795 (2015).
- [8] K. A. Vermeer, J. van der Schoot, H. G. Lemij, and J. F. de Boer, “RPE-normalized RNFL attenuation coefficient maps derived from volumetric OCT imaging for glaucoma assessment,” *Invest. Ophthalmol. & Vis. Sci.* **53**, 6102-6108 (2012).
- [9] G. Thepass, H. G. Lemij, K. A. Vermeer, “Attenuation Coefficients From SD-OCT Data: Structural Information Beyond Morphology on RNFL Integrity in Glaucoma,” *Glaucoma* **26**, 1001–1009 (2017).
- [10] J. van der Schoot, K. A. Vermeer, J. F. de Boer, and H. G. Lemij, “The effect of glaucoma on the optical attenuation coefficient of the retinal nerve fiber layer in spectral domain optical coherence tomography images,” *Invest Ophthalmol Vis Sci* **53**, 2424–2430 (2012).
- [11] E. A. Swanson, J. A. Izatt, M. R. Hee, et al. “In vivo retinal imaging by optical coherence tomography,” *Opt Lett.* **18**, 1864–1866 (1993).
- [12] J. Fujimoto and E. Swanson, “The Development, Commercialization, and Impact of Optical Coherence Tomography,” *Invest. Ophthalmol. Vis. Sci.* **57**(9), OCT1–OCT13 (2016).
- [13] D. Huang, E. A. Swanson, et al. “Optical coherence tomography,” *Science.* **254**, 1178–1181 (1991).
- [14] P. Wachulak, A. Bartnik, and H. Fiedorowicz, “Optical coherence tomography (OCT) with 2 nm axial resolution using a compact laser plasma soft X-ray source”, *Sci. Rep.*, **8**, 8494-8502 (2018).
- [15] F. de Boer, B. Cense, et al. “Improved signal-to-noise ratio in spectral-domain compared with time-domain optical coherence tomography,” *Opt. Lett.* **28**, 2067–2069 (2003).
- [15] R. Leitgeb, C. K. Hitzenberger, and A. F. Fercher, “Performance of fourier domain vs. time domain optical coherence tomography,” *Opt. Express* **11**, 889–894 (2003).

- [16] M. A. Choma, M. V. Sarunic, C. H. Yang, J. A. Izatt, "Sensitivity advantage of swept source and Fourier domain optical coherence tomography," *Opt. Express* **11**, 2183–2189 (2003).
- [17] W. Wieser, B. R. Biedermann, T. Klein, C. M. Eigenwillig, R. Huber, "Multi-Megahertz OCT: High quality 3D imaging at 20 million A-scans and 4.5 GVoxels per second," *Opt. Express* **18**, 14685–14704 (2010).
- [18] S. H. Yun, G. J. Tearney, J. F. de Boer, B. E. Bouma, "Pulsed-source and swept-source spectral-domain optical coherence tomography with reduced motion artifacts," *Opt. Express*, **12**, 5614-5624 (2004).
- [19] B. Potsaid, B. Baumann, D. Huang, et al." Ultrahigh speed 1050nm swept source/Fourier domain OCT retinal and anterior segment imaging at 100,000 to 400,000 axial scans per second," *Opt. Exp.* **18**, 20029-20048 (2010).
- [20] J. M. Schmitt, A. Knüttel, M. Yadlowsky, and M. A. Eckhaus, "Optical-coherence tomography of a dense tissue: statistics of attenuation and backscattering," *Phys. Med. Biol.* **39**, 1705-1720 (1994).
- [21] R. O. Esenaliev, K. V. Larin, I. V. Larina, and M. Motamedi, "Non-invasive monitoring of glucose concentration with optical coherence tomography," *Opt. Lett.* **26**, 992-994 (2001).
- [22] A. I. Kholodnykh, I. Y. Petrova, K. V. Larin, M. Motamedi, R. O. Esenaliev, "Precision of Measurement of Tissue Optical Properties with Optical Coherence Tomography," *Appl. Opt.* **42**, 3027-3037 (2003).
- [23] K. A. Vermeer, J. Mo, J. J. Weda, H. G. Lemij, and J. F. de Boer, "Depth-resolved model-based reconstruction of attenuation coefficients in optical coherence tomography," *Biomed. Opt. Exp.* **5**, 322-337 (2013).
- [24] L. Thrane, H. T. Yura, and P. E. Andersen, "Analysis of optical coherence tomography systems based on the extended Huygens Fresnel principle," *J. Opt. Soc. Am.* **17**, 484-490 (2000).
- [25] V. Duc Nguyen, D. J. Faber, E. van der Pol, T. G. van Leeuwen, and J. Kalkman, "Dependent and multiple scattering in transmission and backscattering optical coherence tomography," *Opt. Exp.* **21**, 29145-29156 (2013).
- [26] S. H. Yun, G. J. Tearney, B. E. Bouma, B. H. Park, and J. F. de Boer, "High-speed spectral-domain optical coherence tomography at 1.3  $\mu$ m wavelength," *Opt. Exp.* **11**, 3598-3604 (2003).

- [27] T. G. van Leeuwen, D. J. Faber, and M. C. Aalders, “Measurement of the axial point spread function in scattering media using single-mode fibre-based optical coherence tomography,” *IEEE J. Sel. Top. Quant. Electr.* **9**, 227–233 (2003).
- [28] D. C. Hood and R. H. Kardon, “A framework for comparing structural and functional measures of glaucomatous damage,” *Prog. Retin. Eye Res.* **26**, 688–710 (2007).
- [29] N. M. Jansonius, J. Nevalainen, B. Selig, L. M. Zangwill, P. A. Sample, W. M. Budde, J. B. Jonas, W. A. Lagrèze, P. J. Airaksinen, R. Vonthein, L. A. Levin, J. Paetzold, and U. Schieffer, “A mathematical description of nerve fibre bundle trajectories and their variability in the human retina,” *Vision Res.* **49**, 2157–2163 (2009).
- [30] D.C. Hood, A. S. Raza, C. G. V. de Moraes, J. M. Liebmann, and R. Ritch, “Glaucomatous damage of the macula,” *Prog. Retin. Eye Res.* **32**, 1–21 (2013).
- [31] D. F. Garway-Heath, D. Poinoosawmy, F. W. Fitzke, and R. A. Hitchings, “Mapping the visual field to the optic disc in normal tension glaucoma eyes,” *Ophthalmology* **107**, 1809–1815 (2000).
- [32] J. Denniss, A. Turpin, F. Tanabe, C. Matsumoto, A. M. McKendrick, “Structure-function mapping: variability and conviction in tracing retinal nerve fibre bundles and comparison to a computational model,” *Invest. Ophthalmol. Vis. Sci.* **55**, 728–736 (2014).
- [33] J. Lamparter, R. A. Russell, H. Zhu, R. Asaoka, T. Yamashita, T. Ho, D. F. Garway-Heath, “The influence of intersubject variability in ocular anatomical variables on the mapping of retinal locations to the retinal nerve fibre layer and optic nerve head,” *Invest. Ophthalmol. Vis. Sci.* **54**, 6074–6082 (2013).
- [34] P. J. Airaksinen, S. Doro, J. Veijola, “Conformal geometry of the retinal nerve fibre layer,” *Proc. Natl. Acad. Sci. U.S.A.* **105**, 19690–19695 (2008).
- [35] J. Nevalainen, “Utilisation of the structure of the retinal nerve fibre layer and test strategy in visual field examination,” *Acta Universitatis Ouluensis. D 1057*, 1057 (2010).
- [36] N. S. Erler, S. R. Bryan, P. H. C. Eilers, E. M. E. H. Lesaffre, H. G. Lemij, K. A. Vermeer, “Optimizing structure-function relationship by maximizing correspondence between glaucomatous visual fields and mathematical retinal nerve fibre models,” *Invest. Ophthalmol. Vis. Sci.* **55**, 2350–2357 (2014).
- [37] F. J. Carreras, J. Medina, M. Ruiz-Lozano, I. Carreras, J. L. Castro, “Virtual tissue engineering and optic pathways: plotting the course of the axons in the retinal nerve fibre layer,” *Invest. Ophthalmol. Vis. Sci.* **55**, 3107–3119 (2014).

# 2 Quantitative forward model of spectral-domain optical coherence tomography

---

## 2.1 Introduction

The advent of spectral-domain (SD) OCT systems significantly improved the acquisition speed and sensitivity of OCT systems. In an SD-OCT system, the light beam originating from the source is divided by the beamsplitter and directed into the reference and sample arm. The beam in the reference arm transmits towards a moving mirror located at a certain distance from the beamsplitter. The incident light in the sample arm propagates into the sample under investigation. The backscattered light from the sample will interfere with the reflected light from the reference arm and is directed towards a spectrometer followed by a linear detector array. The OCT detector measures the intensity of the interference spectrum after which a depth profile for a single A-line is computed. A volumetric scan can be obtained by recording the A-lines while scanning the beam over the surface of the sample using a scanning mirror.

In the next sections, we will present two methods to model the OCT signal of a semi-infinite media based on a single-scattering model of light in the sample. The first comprehensive approach, explained in section 2.2.1, uses the interference of the electric fields in the sample and reference arm and takes into account the known characteristics of the OCT system, the shape of the OCT beam, the spatial distribution of attenuation coefficients in the samples and noise. The second more concise approach, discussed in section 2.2.2, is merely based on a simple representation of the OCT signal by taking into account the attenuation coefficient, the shape of the OCT beam and a scaling factor. In addition, the numerical simulations of both methods will be compared with each other and with measured OCT signals obtained from an experimental OCT system. Finally, based on these results, we will decide which method will be used later in this thesis for simulation and modelling of the OCT signal in semi-infinite samples (Chapter 4).

## 2.2 Method

In this section, first the OCT signal of a semi-infinite media is simulated using the interference of the electrical fields of the reference and the sample arm. Later, a simpler model of the OCT signal is described which will be compared with the first method.

### 2.2.1 Method A: The recorded OCT signal in a SD-OCT system

The power spectral density function of a light source  $S(k)$  is the time-averaged power of the electric field amplitude  $s(k, \omega)$ ,

$$S(k) = \langle |s(k, \omega)|^2 \rangle, \quad (2.1)$$

which is a function of the wavenumber  $k = 2\pi/\lambda$  and the angular frequency  $\omega = 2\pi\nu$ . The wavenumber  $k$  denotes the spatial frequencies and  $\omega$  the temporal frequencies of each spectral component of wavelength  $\lambda$ . Note that the wavelength and frequency are coupled by the index of refraction, which is wavelength-dependent in dispersive media.

The wide-band power spectrum of the light source can be modeled by a Gaussian function centered at  $k_c$  and with a peak power for the central wavenumber of  $P_{ref}$  as follows

$$S(k) = P_{ref} e^{-\left(\frac{k-k_c}{\Delta k}\right)^2}, \quad (2.2)$$

where  $\Delta k$  is the wavenumber bandwidth corresponding to the half-width of the source spectrum at  $1/e$  of its maximum.

The incoming electric field  $E_i$  of the interferometer becomes

$$E_i(k) = s(k, \omega) e^{i(kz - \omega t)}. \quad (2.3)$$

For the aforementioned Gaussian-shaped source spectrum, the electric field illuminating the interferometer becomes,

$$E_i(k) = \sqrt{P_{ref}} e^{-\frac{(k-k_c)^2}{2(\Delta k)^2}} e^{i(kz - \omega t)}. \quad (2.4)$$

The Fourier transform of a Gaussian power spectrum  $S(z)$  can be expressed as [1],

$$s(z) = \left[ P_{ref} \frac{\Delta k}{4\pi^{3/2}} e^{-\frac{z^2 \Delta k^2}{4}} \right] e^{ik_c z} \quad \xleftrightarrow{\mathcal{F}} \quad S(k) = P_{ref} e^{-\left(\frac{k-k_c}{\Delta k}\right)^2}$$

In case one is interested in the magnitude only,  $|s(z)|$ , we obtain

$$|s(z)| = P_{ref} \frac{\Delta k}{4\pi^2} e^{-\frac{z^2 \Delta k^2}{4}}. \quad (2.5)$$

### 2.2.1.1 The reference arm

The Gaussian power spectrum of the incoming electrical field is wavelength-independent split into the reference arm and the sample arm of the interferometer. A fraction  $\beta$  of the incoming beam enters the sample arm ( $0 \leq \beta \leq 1$ ). The fraction  $1 - \beta$  enters the reference arm. The reflector at the end of the reference arm has an electric field reflectivity of  $r_R$  and a power reflectivity of  $R_r = |r_R|^2$ . The electrical field returning from the reference reflector at the location of the beam splitter becomes

$$E_R(k) = E_i(k) \sqrt{1 - \beta} r_R e^{ik2z_R}. \quad (2.6)$$

### 2.2.1.2 The sample arm

The sample yields a depth-dependent reflectivity of the electrical field. Only a very small fraction of light is scattered back from the sample and collected by the lens back into the fibre at any given depth. Although the sample and hence the scattering occurs at a continuous depth range, we model the electrical field returning from the sample as a weighted sum of  $N$  weak reflections

$$E_S(k) = E_i(k) \sqrt{\beta} \sum_{n=1}^N \alpha_S(n) e^{ik2z_S(n)}, \quad (2.7)$$

with  $\alpha_S(n)$  the electrical field reflectivity at depth  $z_S(n)$ . In this simplified model, attenuation of the beam penetrating the sample at a depth  $z_S$  due to absorption and scattering in the preceding layers is neglected.

### *Light-tissue interaction and Gaussian shape of the OCT beam*

The relation between the depth-dependent attenuation coefficient,  $\mu_s(z)$ , and the measured electrical field reflectivity of the sample can be modeled as,

$$\alpha_{s_n}(z_{s_n}) \propto \sqrt{e^{-2 \int_0^{z_{s_n}} \mu_s(z) dz}}, \quad (2.8)$$

by assuming a single scattering event for weakly scattering media, while ignoring the other effects such as absorption, the light angle of incident and multiple scattering.

On the other hand, the field is focused into the sample at a depth  $z_0$ . This yields an axial point spread function that can be modeled by a Cauchy distribution [2] and its relation with the sample's electrical field reflectivity can be expressed as,

$$\alpha_{s_n}(z_{s_n}) \propto \sqrt{\frac{1}{\left(\frac{z_{s_n}-z_0}{2z_R}\right)^2 + 1}}, \quad (2.9)$$

where  $z_R$  denotes the Rayleigh length of the focused beam in the medium.

By taking into account both the attenuation coefficient and Gaussian shape of the OCT beam, we can related the measured sample reflectivity in the detector to the real reflectivity of the sample  $r_{s_n}(z_{s_n})$  by,

$$\alpha_{s_n}(z_{s_n}) \propto r_{s_n}(z_{s_n}) \sqrt{\frac{1}{\left(\frac{z_{s_n}-z_0}{2z_R}\right)^2 + 1}} \cdot e^{-2 \int_0^d \mu_s(z) dz}. \quad (2.10)$$

The reconstruction of the measured power reflectivity of the sample,  $|\alpha_{s_n}(z_{s_n})|^2$ , is the main goal of the OCT systems. However, this measured sample's power reflectivity needs to be corrected for the effect of the signal attenuation and the shape of the OCT beam to obtain the samples' reflectivity  $r_{s_n}(z_{s_n})$ .

#### **2.2.1.3 Interference and detection**

The returning electrical fields from the sample and the reference arm interfere at the beam splitter. This intensity may be expressed as

$$I_o(k) = |E_R + E_S|^2 = (E_R + E_S)(E_R + E_S)^*, \quad (2.11)$$

where “\*” indicates the complex conjugate.

This intensity is analyzed by a spectrometer and recorded by a linear CCD array. The detected spectrum is the time-averaged intensity at the output of the interferometer

$$I_D(k) = \langle I_o(k) \rangle = \langle (E_R + E_S)(E_R + E_S)^* \rangle \cdot R(k; w), \quad (2.12)$$

where  $R(k)$ , known as roll-off, denotes the finite spectral resolution of the spectrometer and CCD detector. Note that time averaging due to the finite response time of the detector eliminates the time-dependent terms depending on the temporal frequency  $\nu$ , which leaves an intensity spectrum as a function of the wavenumber  $k$ . The inverse Fourier transform of  $R(k; w)$  becomes

$$r(z; w) \propto \left( \frac{\sin(\Psi)}{\Psi} \right)^2 \exp\left(-\frac{w^2 \Psi^2}{2 \ln(2)}\right), \quad (2.13)$$

where  $w$  indicates the ratio of the spectral resolution to the sampling interval and  $\Psi = (\pi/2) \cdot (z/z_D)$  is the normalized depth to the maximum depth of the image. The first factor originates from the finite pixel size of the CCD array and the second term from the spectrometer.

Expanding the detected intensity comprises three terms [1],

$$\begin{aligned} I_D(k) = & R(k; w) * \{ \beta S(k) [R_{S_1} + R_{S_2} + \dots + R_{S_N}] + (1 - \beta) R_R S(k) \} \quad \text{“DC terms”} \\ & + \sqrt{\beta(1 - \beta)} S(k) \sum_{n=1}^N \alpha_R \alpha_{S_n} \cos[2k(z_R - z_{S_n})] \quad \text{“Interference term”} \\ & + \beta S(k) \sum_{n \neq m=1}^N \alpha_{S_n} \alpha_{S_m} \cos[2k(z_{S_n} - z_{S_m})] \} \quad \text{“Auto-correlation term”}. \end{aligned} \quad (2.14)$$

where  $R_{S_n} = |\alpha_{S_n}|^2$ . The auto-correlation term is the interference between the sample reflectors and can be ignored by increasing the reference arm power with respect to the sample arm.

#### 2.2.1.4 Sampling

In the discrete-domain, the spectrum is sampled at a sampling rate  $\delta_s k = \Delta k/M$  and to avoid aliasing it should be smaller than Nyquist range, half the spectral sampling frequency. Hence, for  $M$  number of pixels on the detector, the continuous spectrum is multiplied by an impulse train [1],

$$I[k] = I(k) \sum_{n=1}^M \delta(k - n\delta_s k). \quad (2.15)$$

The sampling interval in the  $z$ -domain can be obtained by,

$$\delta_s z = \frac{\pi}{\Delta k}. \quad (2.16)$$

The maximum depth  $Z_{max}$  can be obtained by  $M \cdot \delta_s z$  [1].

#### 2.2.1.5 Non-linear spacing and interpolation

The spectra data measured by the spectrometer are non-linearly spaced in wavenumber space. The wavenumber distribution has been modeled previously as a function of the angle of incident light on the grating, the distance between grating lines, the distance between the focusing lens and the CCD/cMOS camera, and the position of the center wavelength on the camera [3]. It has been shown that taking the Fourier transform of the measured intensity results in dispersion [3]. This problem has been solved by a global interpolation, known as zero-filling technique [3]. The procedure starts with zero-padding of the data obtained later in section 2.2.1.9 in the  $z$ -space to increase the data array to  $n \times N$  – where  $N$  is the number of pixels on the detector and  $n$  is an integer value – and a FFT back into  $k$ -space. Afterwards, a linear interpolation is performed on the  $n$ -fold data array and an FFT yields the depth profile. Additionally, as described in Section 2.2.1.4, the sample's power reflectivity is calculated by squaring the depth profile.

#### 2.2.1.6 Contribution of noise

In SD-OCT systems, there are three different contributions of noise: the shot noise, the read-out noise and the relative intensity noise (RIN). The shot noise is the fluctuation of the detected electrons in time caused by quantization of light and charge and has a Poisson distribution. A SD-OCT system is shot-noise limited when the shot noise term dominates the other noise components [1,3].

The light intensity can be obtained by the number of photons on each pixel of the detector. The average number of detected electrons  $\overline{N_e(k)}$  on a certain cell in the camera can be related to the reference power  $P_{ref}$  by [3],

$$\overline{N_e(k)} = \frac{\tau \rho}{E_v(k)} P_{ref}(k) \quad [\# \text{ of electrons}], \quad (2.17)$$

where  $\rho$  is the detector quantum efficiency and  $\tau$  is the integration time of the detector.  $E_v(k) = k \cdot h \cdot c$  is the wavenumber dependent energy of a photon where  $h$  is the reduced Plank constant and  $c$  is the speed of light [3]. The number of detected electrons follows a Poisson distribution with mean and variance value of  $\overline{N_e(k)}$ . After creating different random Poisson distributions for different pixels on the detector, we convert this distribution to the pixel value  $I_D(k)$  by dividing it by  $\Delta e$  (the A/D conversion resolution) and indicate the number of electrons which are needed for increasing a pixel's value by one. The averaged pixel value of the detector for different measurements can be obtained by [3],

$$\overline{I_D(k)} = \frac{\overline{N_e(k)}}{\Delta e} \quad [\text{arb. unit}], \quad (2.18)$$

The variance of the pixel values for different measurements can be obtained by,

$$\sigma_e^2(k) = \frac{\overline{N_e(k)}}{\Delta e^2} = \frac{\overline{I_D(k)}}{\Delta e} \quad [\text{arb. unit.}]. \quad (2.19)$$

### 2.2.1.7 Removing the fixed pattern noise

The structural information of the sample can be obtained by the interference of the beams in the reference and sample arm which results in the modulation of the spectrum. However, other causes of the modulation of the spectrum such as optical interferences in the optical pathway of the reference light, so called fixed pattern noise, and the variations in the measured intensities in the detector [4] can cause artefacts.

Different methods have been proposed to remove the fixed pattern noise from the spectrum [1]. Among them, the artefact can be removed by subtracting the average of a large number of A-lines from the measured spectra while having no sample in the sample arm [1]. This method only removes the DC artefact caused by the reference arm which modifies the Eq. 2.14 to [1],

$$I'_D(k) = R(k; w) * \left[ \sqrt{\beta(1-\beta)} S(k) \sum_{n=1}^N \alpha_R \alpha_{S_n} \cos(2k(z_R - z_{S_n})) + \beta S(k)(R_{S_1} + \dots + R_{S_N}) \right]. \quad (2.20)$$

### 2.2.1.8 Depth profile

As mentioned,  $\alpha_{S_n}$  is the square root of the sample reflectivity at depth  $z_{S_n}$ . Therefore, the depth information can be obtained by squaring the magnitude of the inverse Fourier transform of the fixed pattern noise removed spectra  $I'_D(k)$  [1],

$$|i_D(z)|^2 = r(z; w)^2 \cdot \left[ \sqrt{\beta(1-\beta)} s(z) * \sum_{n=1}^N \alpha_R \alpha_{S_n} \delta(z \pm 2(z_R - z_{S_n})) + \beta s(z)(R_{S_1} + \dots + R_{S_N}) \right]^2. \quad (2.21)$$

### 2.2.2 Method B: A simple model of the OCT signal

In a single-scattering model of light, the Fourier-domain OCT signal at depth  $z$  in a homogeneous sample may be expressed as,

$$S(z) = r(z; w)^2 \cdot \frac{1}{\left(\frac{z-z_0}{2z_R}\right)^2 + 1} \cdot C e^{-2z\mu}, \quad (2.22)$$

where the signal decay is modeled by three factors (from left to right): the roll-off, the axial PSF modeled and the signal attenuation modeled by the scattering coefficient  $\mu$  and scaling factor  $C$ . In the next section, this model will be used to simulate the OCT signal.

## 2.3 Experiments

In this section, the simulation results for both Methods A and B will be shown and compared with real measurements obtained using an experimental OCT system. The specifications of the experimental OCT setup have been used to set the values of the simulation parameters.

### 2.3.1 Measurements

A Ganymede-II-HR Thorlabs spectral domain OCT system (GAN905HV2-BU) was used to obtain the B-scans of three semi-infinite samples with 0.05 w.t.%, 0.1 w.t.% and 0.25 w.t.% of TiO<sub>2</sub> dispersed in silicone with various locations of the focal plane from the

samples' surfaces. The samples were located at 0.4 mm from the zero delay line. The system has a centre wavelength of 900 nm and a bandwidth of 195 nm and a scan lens with 18 mm focal length (LSM02-BB). The system's axial and lateral resolutions were 3  $\mu\text{m}$  and 4  $\mu\text{m}$  in air, respectively, and the axial and lateral physical pixel size in air was  $1.27 \times 2.9 \mu\text{m}$  with 1024 pixels on each A-line.

First, the focus position was manually set to the sample's surface by optimizing the surface structure's sharpness in the enface image created by the OCT camera. Next, 90 B-scans were obtained at various locations of the focal plane by changing the location of the lens in the sample arm with a physical step size of 11.25  $\mu\text{m}$  within a range of  $\pm 0.5$  mm around the initial focus location.

Several pre-processing steps have been performed on the measured spectra. First, the reference arm intensity, which was measured automatically by the system for every acquisition, was removed. Second, to compensate for the nonlinear spacing, the spectra were interpolated based on the reported wavelength distribution on the detector by the system manufacturer. Finally, the OCT signals were generated by squaring the Fourier transform of the interpolated signal. As mentioned in section 2.1, the averaged noise floor was obtained, by averaging over a large number of A-lines while having no sample in the sample arm, and subtracted from the A-lines. Afterwards, the roll-off of the system was measured and the A-lines were corrected for it.

### *Roll-off estimation*

To estimate the roll-off, scans of 0.25 w.t.%  $\text{TiO}_2$  for different locations of the surface within the OCT image depth range were obtained by changing the optical path length of the reference arm. Afterwards, the sensitivity decay was obtained by smoothing and interpolating the average intensities of the corresponding region of interest in the scans (Fig. 1.2). The following roll-off function [5] was fitted to the measurements to estimate the spectral resolution of the spectrometer,  $w$ ,

$$R(z; w) = \log \left( c \left( \frac{\sin(\psi)}{\psi} \right)^2 \exp \left( - \frac{w^2 \psi^2}{2 \ln(2)} \right) \right) \quad (2.23)$$

where  $c$  is the scaling factor and  $\psi$  is the depth normalized to the maximum ranging depth. The fitted model to the measurements can be seen in Fig. 1.2 with the estimated parameter  $w = 1.5$ .

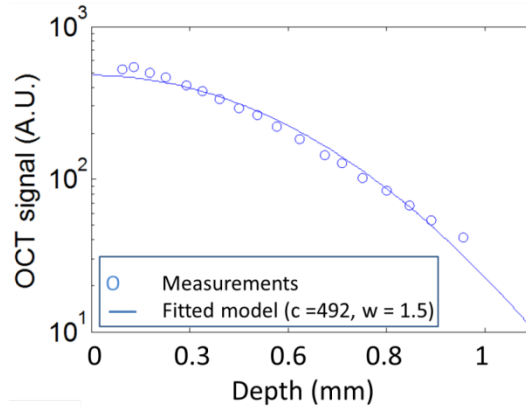


Figure 2.1 Measurements (circles) and the model fit to the measurements indicating the OCT system’s roll-off.

### *Rayleigh length estimation*

Figure 2.2(a) shows a B-scan of 0.05 wt. %  $\text{TiO}_2$  in silicone with adjusted focus location at 0.26 mm from the focus location on the surface, as estimated by optimizing the sharpness. Fig. 2.2(b) shows the concatenation of the averaged A-lines (from each B-scan) as a function of focus position. The location of the sample remained fixed in the B-scan for various focus positions by adjusting the optical path length of the system’s reference arm. As can be seen in Fig. 2.2(b), the highest intensity on the surface deviates from the centre of the image, which indicates a shift in the aforementioned adjustment of the focus position on the surface.

Several pre-processing steps have been performed on the measured spectra. First, the reference arm intensity, which was measured automatically by the system for every acquisition, was removed. Second, to compensate for the nonlinear spacing, the spectra were interpolated based on the reported wavelength distribution on the detector by the system manufacturer. Finally, the OCT signals were generated by squaring the Fourier transform of the interpolated signal. As mentioned in section 2.1, the averaged noise floor was obtained, by averaging over a large number of A-lines while having no sample in the

sample arm, and subtracted from the A-lines. Afterwards, the roll-off of the system was measured and the A-lines were corrected for it. To estimate the roll-off, scans of 0.25 wt. % TiO<sub>2</sub> for different locations of the surface within the OCT image depth range were obtained by changing the optical path length of the reference arm, and the sensitivity decay was obtained by smoothing and interpolating the average intensities of the corresponding region of interest in the scans. Finally, regions above and inside the sample that only contained noise were removed for each B-scan [7].

The system's Rayleigh length was estimated by the following procedure. For each B-scan obtained from the sample with 0.05 wt. % of TiO<sub>2</sub> in silicone, the averaged A-line was calculated and the arbitrary data-point at the physical depth of 63 μm from the sample's surface were recorded. This physical depth should be close enough to the surface to obtain a sufficiently high SNR and far enough from the surface to avoid the data-points being affected by reflection artefact. The initial values of  $z_0$  and  $z_R$  were obtained by fitting the following model to the recorded data-points (Fig.2. 2(c)),

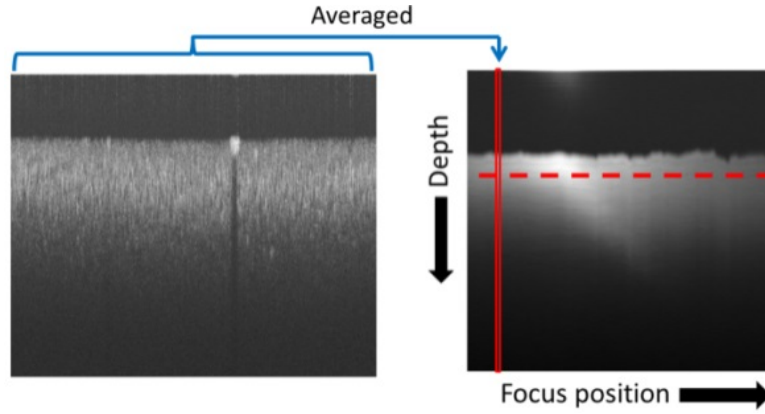
$$f(z; z_0, z_R) = \frac{C}{\left(\frac{z - z_0}{2z_R}\right)^2 + 1} \quad (2.24)$$

where  $z_R$  is the Rayleigh length which depends on the refractive index  $n$  of the medium [18]. In addition, the shifted focus positions were transformed from physical to optical distance. The optical Rayleigh lengths in air and silicone (with refractive index of  $n_{sample} = 1.44$ ) were estimated to be 29.3 μm and 60.8 μm ( $z_{RSi} = n_{Si}^2 \cdot z_{Rair}$ ), respectively, shown in Fig. 2.2(c). The physical Rayleigh length in silicone was calculated to be 42 μm.

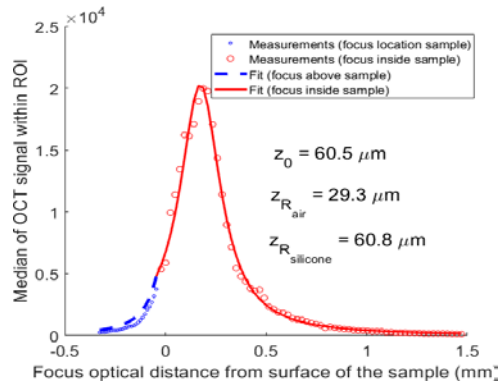
The system's Rayleigh length was estimated by the following procedure. For each B-scan obtained from the sample with 0.05 w.t.% of TiO<sub>2</sub> in silicone, the averaged A-line was calculated and the data-points at the physical depth of 63 μm from the sample's surface were recorded. The initial values of  $z_0$  and  $z_R$  were obtained by fitting the following model to the recorded data-points (Fig. 2.2(c)),

$$f(z; z_0, z_R) = \frac{c}{\left(\frac{z-z_0}{2z_R}\right)^2 + 1}, \quad (2.25)$$

where  $z_R$  is the Rayleigh length which depends on the refractive index  $n$  of the medium [18]. In addition, the shifted focus positions were transformed from physical to optical distance. The optical Rayleigh lengths in air and silicone (with refractive index of  $n_{sample} = 1.44$ ) were estimated to be  $29.3 \mu\text{m}$  and  $60.8 \mu\text{m}$  ( $z_{R_{Si}} = n_{Si}^2 \cdot z_{R_{air}}$ ), respectively, shown in Fig. 2.2(c). The physical Rayleigh length in silicone was calculated to be  $z_{R_{Si}}/n_{Si} = 42 \mu\text{m}$ .



(a) (b)



(c)

Figure 2.2 a) A B-scan of 0.05 w.t.% TiO<sub>2</sub> dispersed in silicone with the focus location at 0.26 mm inside the sample; b) The averaged A-lines from the acquired B-scans per focus position as a function of focus position; c) The averaged OCT signals (circles) along data-points located at  $63 \mu\text{m}$  inside the sample (dashed lines in (a)) with the best fitted focus model in Eq. 2.23.

## 2.3.2 Simulation

### *Method A*

We will use the known specifications and estimated model parameters of the Thorlabs experimental OCT-system (Table 2.1) to simulate the OCT signal described in section 2.2. Fig. 2.3 shows a Gaussian source spectrum with a central wavelength of 825 nm, the wavelength bandwidth (FWHM) of 150 nm and  $P_{ref}$  of 4.6 nWatt for the central pixel. The beamsplitter directs 0.001% of the beam into the sample arm and 0.999% of the beam into the reference arm. The beam in the reference arm is directed towards a mirror, with reflectivity  $\alpha_R = 1$ , located at the distance of 0.1 mm from the beamsplitter. The incident light in the sample arm propagates into a homogeneous sample with a refractive index of 1.44 located at a distance of 0.25 mm from the optical path length of the reference arm. The attenuation coefficient of the sample is set to  $2 \text{ mm}^{-1}$ . To consider the shape of the OCT beam in the sample, the Rayleigh length inside the sample was assumed to be 200  $\mu\text{m}$ . At this stage, the beam is focused in the sample arm with an objective lens. The Rayleigh length and the locations of the focus are set to the values explained in Section 2.3.1. The attenuation coefficient of the semi-infinite samples with 0.05 w.t.%, 0.1 w.t.% and 0.25 w.t.% of  $\text{TiO}_2$  in silicone were estimated previously to be 1.1, 1.8 and  $3.1 \text{ mm}^{-1}$  respectively [6]. However, these estimated attention coefficients

Table 2.1 The simulation parameters.

$P_{ref}$	4.6 nWatt	Peak power for the central wavenumber
$\alpha_R$	1	Reflectivity of the reference mirror
$\Delta\lambda$	150 nm	Wavelength bandwidth (FWHM)
$\lambda_c$	825 nm	Central wavelength of the source
$\tau$	34 $\mu\text{s}$	Integration time
$\Delta e$	173	A/D conversion resolution
$\rho$	0.8	Detector quantum efficiency
$w$	1.57	Spectrometer spectral resolution
$N_p$	1024	Number of pixels in the detector
$\delta_s z$	1.27 $\mu\text{m}$	Axial physical pixel size
$Z_{max}$	1.9 $\mu\text{m}$	Maximum depth
$\varphi_0$	54 $\mu\text{m}$	Physical Rayleigh length in air

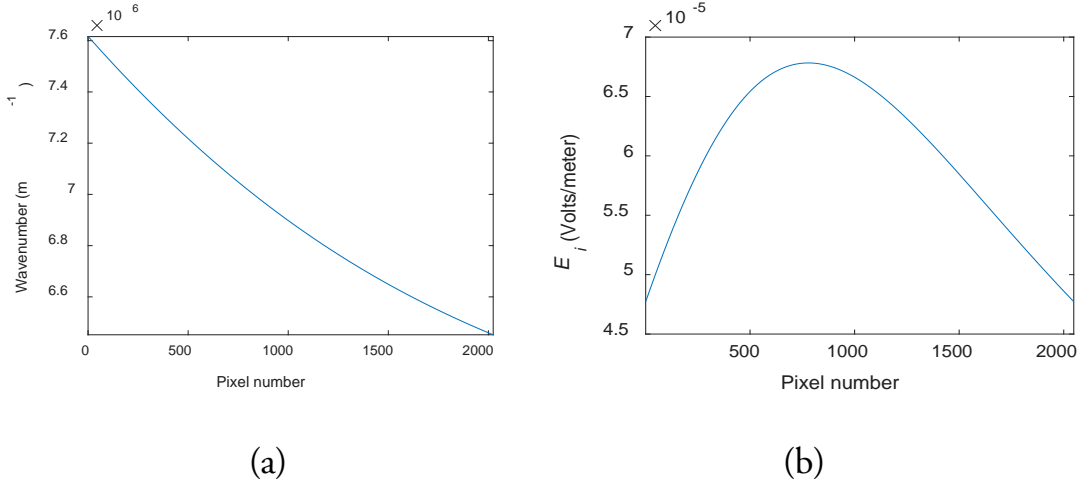


Figure 2.3 a) Non-linear distribution of the wavenumber on the detector with function  $(.)^{0.8}$ ; b) the electric field illuminating the interferometer ( $E_i$  in Eq. 2.4).

values are not accurate since the effect of the shape of the OCT beam was not taken into account in the estimation method presented.

The backscattered light from the sample interferes with the reflected light from the reference arm and is detected by a linear detector array with 1024 pixels. The distribution of the wavenumbers in the pixels is modelled by  $(.)^{0.8}$  as is shown in Fig. 2.3(a). The detected source spectrum is shown in Fig. 2.3(b). The sampling interval of the spectrometer in the  $z$ -domain can be calculated as  $1.27 \mu\text{m}$  by Eq. 2.16. The spectrometer's resolution  $w$  is set to 1.5. The noise on the detector is modelled as was described in Section 2.2.1.7. In Eq. 2.18 and 2.19, the parameters  $\rho$ ,  $\tau$  and  $\Delta e$  are set to 0.8 and  $34 \mu\text{s}$  and 173 electrons, respectively. The detected depth profile is obtained by the squared magnitude of the inverse Fourier of the interpolated measured signal. Fig. 2.4(a) shows the averaged depth-profile over 100 A-lines. As mentioned, as a post-processing step, the fixed pattern noise (DC term) is obtained by averaging over a large number of measured spectra (1000) while having no sample in the sample arm (Fig. 2.4(b)). Finally, Fig. 2.4(c) shows the subtracted DC term from the squared measured OCT signal for the location of focus at 0.36 mm inside the sample.

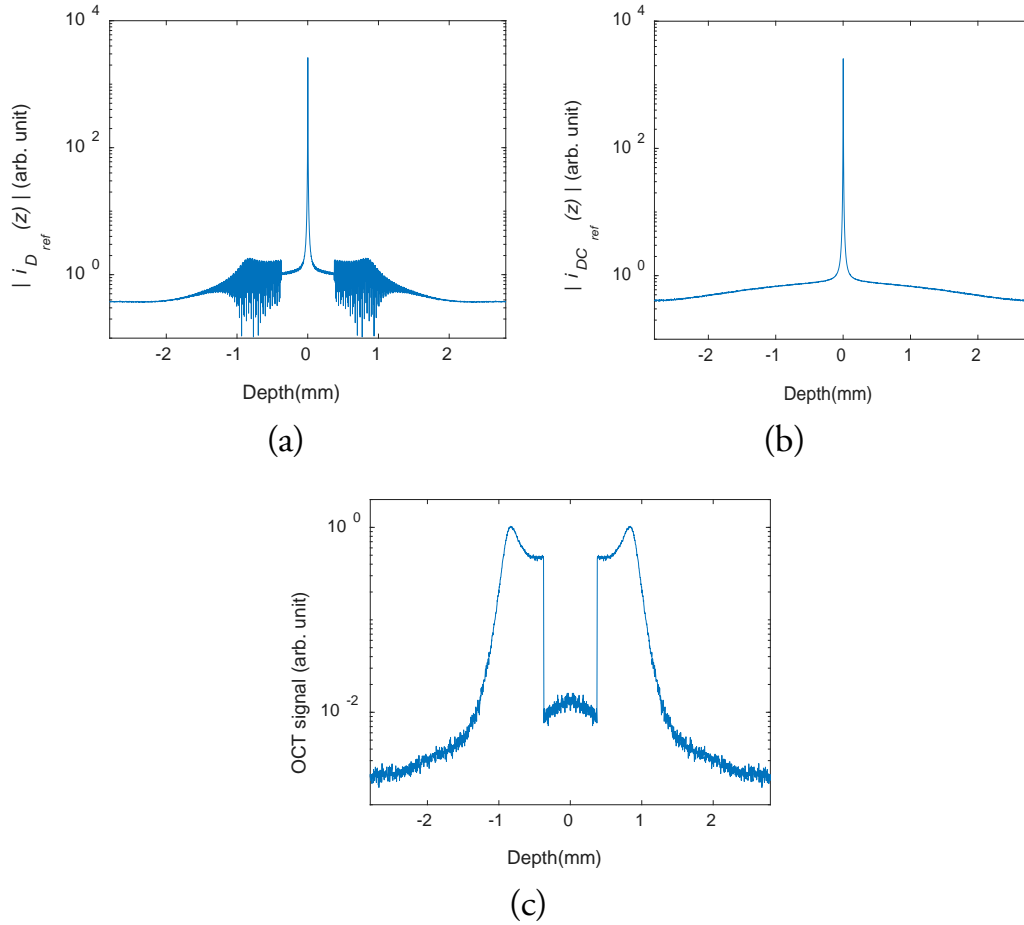


Figure 2.4 The magnitude of the Fourier transform of a) the measured intensity on the detector; b) the measured DC term of the reference arm; c) the squared measured intensity after removing the DC term of the reference arm. The physical location of focus is at 0.36 mm inside the sample.

### Method B

A simple model of the OCT signal explained in Section 2.3 was used to simulate the OCT signal with the aforementioned estimated Rayleigh length, attenuation coefficients and for various locations of the focal plane from the samples' surfaces. The values of the parameter  $C$  were visually adjusted to be 11000, 12000 and 20000 (A.U.) for the semi-infinite samples with 0.05 w.t.%, 0.1 w.t.% and 0.25 w.t.% of  $\text{TiO}_2$  in silicone, respectively.

In Figures 2.5 and 2.6, the simulated OCT signals, method A (dashed line) and method B (circles), and the measured OCT signals (solid lines) are shown for various locations of the focus above and inside the sample. As can be observed there is a small difference between the two simulated OCT signals obtained by methods A and B for signal to noise ratios (SNR) larger than 10%. For the region with a smaller SNR, method

A better represents the signal decay observed in the measured OCT signal. This is because method A implements several steps before obtaining the intensity of the OCT signal such as zero-padding and interpolation.

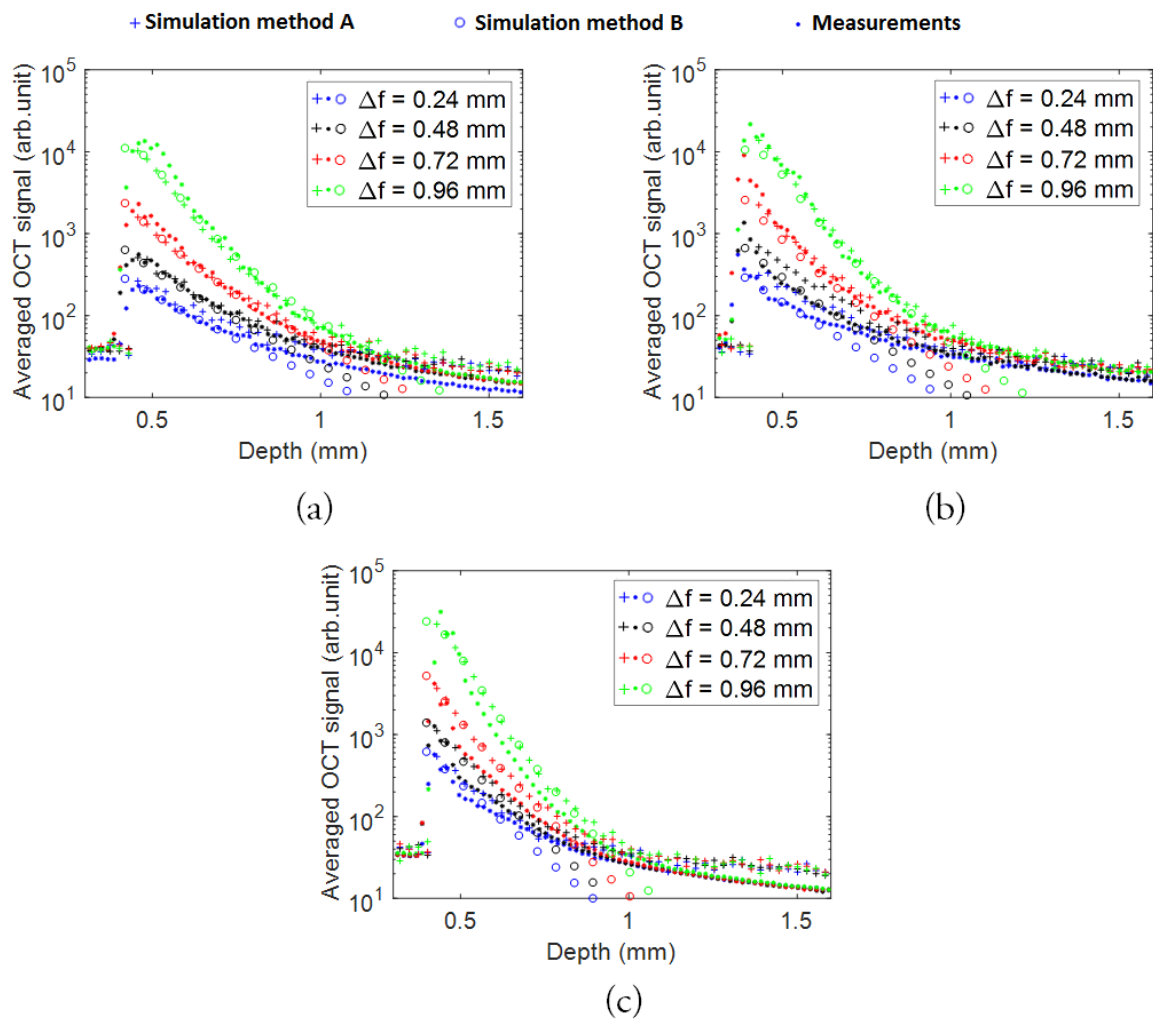


Figure 2.5 The simulated (Method A: dots, Method B: circles) and the measured (plus signs) OCT signals for different locations  $\Delta f$  of the focal plane above the surfaces of different samples with: a) 0.05 w.t.%; b) 0.1 w.t.%; c) 0.25 w.t.% of  $\text{TiO}_2$  in silicone.  $\Delta f$  is the distance of the focus location from the sample's surface.

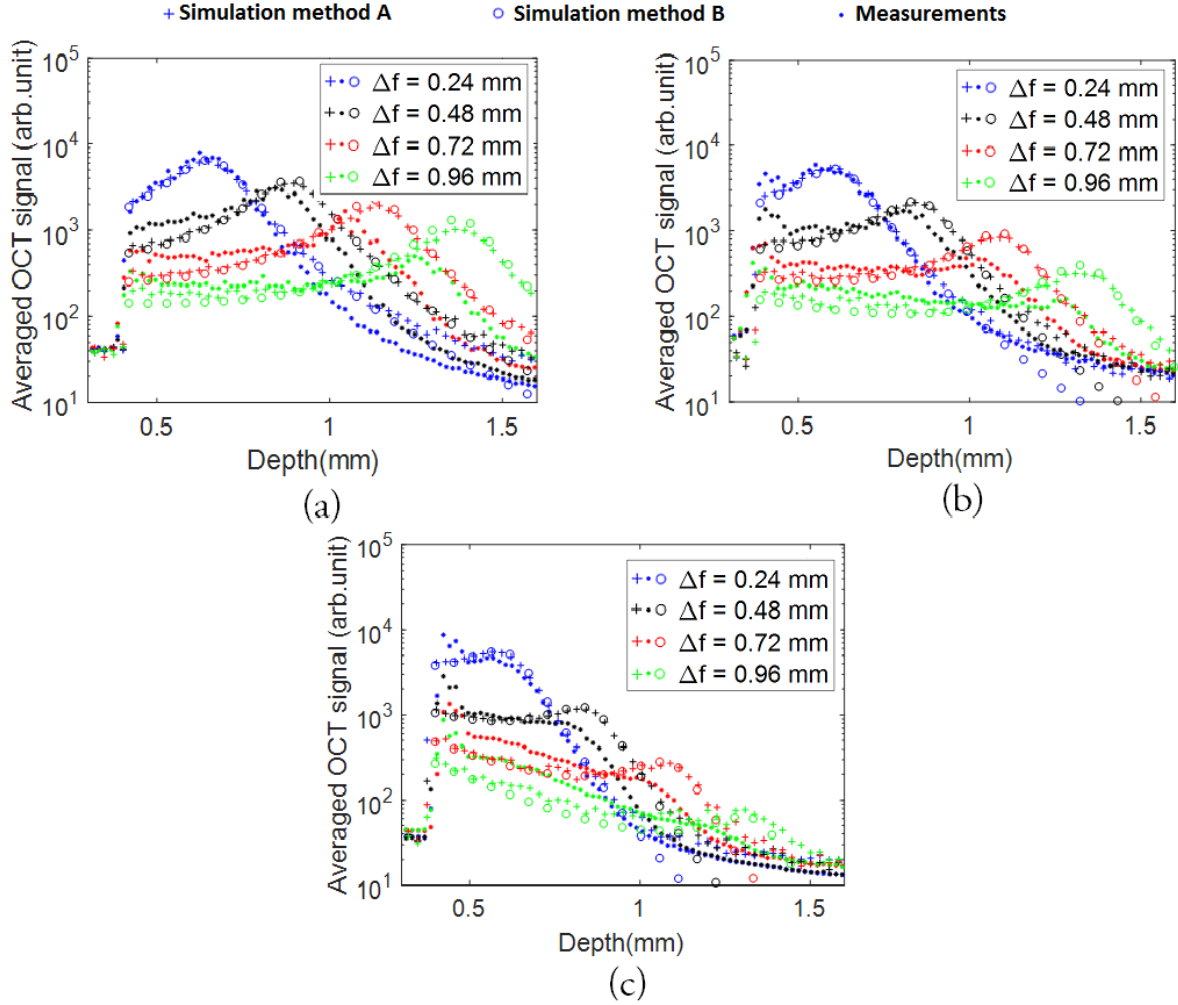


Figure 2.6 The simulated (Method A: dots, Method B: circles) and measured (plus sign) OCT signals obtained for different locations of the focal plane inside the sample with: a) 0.05 w.t.%; b) 0.1 w.t.%; c) 0.25 w.t.% of  $\text{TiO}_2$  in silicone.  $\Delta f$  is the distance of the focus location from the sample's surface.

## 2.4 Conclusion

In this chapter, we presented two methods to simulate the OCT signal for various focus locations above and inside semi-infinite samples with different attenuation coefficients. The more complex simulation, method A, takes into account the interference of the electrical fields in the sample and reference arms, the attenuation coefficient of the sample and the shape of the OCT beam, noise and several post processing steps such as zero-padding and interpolation to correct for the effect of non-linear spacing of the wavelength on the detector. The simpler model, method B, only uses the attenuation coefficient, the shape of the OCT beam and a scaling factor to model the OCT signal. We can visually

observe that in the area with larger SNRs, the simulation results using Method A and Method B are similar to each other. In chapter 4 of this thesis, we will present a method to estimate the sample attenuation coefficients from OCT measurements compensated for the effects of the axial PSF. The recorded signals were modeled by assuming single-scattering in a homogeneous sample accounting for the system's roll-off, noise floor and focused beam shape (axial PSF). In the presented method, the parts of the OCT signal with the larger SNRs have more impact on fitting the model to the signal. Therefore, we can disregard the differences between the OCT signal in Model A and B for small SNRs and use the simpler method, i.e. Method B, as a model of the OCT signal. We also observed that there are differences between the simulation results and the measurements which are mainly caused by a mismatch between the parameter values of the simulation and the experimental set-up. In Chapter 4, we will observe that an accurate estimation of the model parameters will result in obtaining a better fit to the measurements.

## Acknowledgment

I would like to acknowledge Dr. Jeroen Kalkman<sup>1</sup> for his technical support in this work.

## References

- [1] W. Drexler, J. G. Fujimoto, "Optical coherence tomography: technology and applications," Springer Science & Business Media, 2008.
- [2] T. G. van Leeuwen, D. J. Faber, and M. C. Aalders, "Measurement of the axial point spread function in scattering media using single-mode fibre-based optical coherence tomography," *IEEE J. Sel. Top. Quant. Electr.* **9**, 227–233 (2003).
- [3] B. Cense, "Optical coherence tomography of retinal imaging," PhD Dissertation, Twente University, BH Park, MC Pierce (2005).
- [4] S. Moon, S. W. Lee, and Z. Chen, "Reference spectrum extraction and fixed-pattern noise removal in optical coherence tomography," *Optics express*, **18**, 24395-24404 (2010).

---

<sup>1</sup>Department of Imaging Physics, Delft University of Technology, Delft, 2628 BL, The Netherlands.

- [5] S. H. Yun, G. J. Tearney, B. E. Bouma, B. H. Park, and J. F. de Boer, “High-speed spectral-domain optical coherence tomography at 1.3  $\mu$ m wavelength,” *Opt. Exp.* **11**, 3598-3604 (2003).
- [6] K. A. Vermeer, J. Mo, J. J. Weda, H. G. Lemij, and J. F. de Boer, “Depth-resolved model-based reconstruction of attenuation coefficients in optical coherence tomography,” *Biomed. Opt. Exp.* **5**, 322-337 (2013).



### 3 Noise-Adaptive attenuation coefficient in spectral domain optical coherence tomography data

---

The attenuation coefficient is a tissue property that can be estimated from optical coherence tomography (OCT) data. We observed that excessive noise below the retina might cause both an underestimation and a significant variation of the estimated attenuation coefficient values by a state-of-the-art algorithm. Two methods were proposed to reduce these effects: I) by removing the average noise signal from the OCT data; II) by excluding the detected noise region below the retina. The methods were applied to four circular peripapillary retinal scans of a healthy subject. We evaluated all methods quantitatively using metrics for the inter- and intra-A-lines variation of the estimated attenuation coefficients. Both methods resulted in higher attenuation coefficients thereby reducing the bias. However, only method II succeeded in reducing the amount of variation by both metrics; method I made things worse. In conclusion, method II yields a more robust and more precise estimate of the attenuation coefficient, in particular for the choroid and sclera, compared to the baseline method.

B. Ghafaryasl, K. A. Vermeer, Johannes F. de Boer, M. E. J. van Velthoven, L. J. van Vliet, Noise-Adaptive attenuation coefficient in spectral domain optical coherence tomography data, *IEEE 13th International Symposium of Biomedical Imaging (ISBI)*, 706–709 (2016).

### 3.1 Introduction

Optical coherence tomography (OCT) is used for retinal imaging to obtain information about the health status of the retina. The attenuation coefficient is an optical tissue property that can be estimated from OCT data. It has potential as a biomarker for the diagnosis and monitoring of chorioretinal diseases [1]. An accurate estimation of the attenuation coefficients will result in a better understanding of tissue characteristics. Different models have been proposed for estimating the attenuation coefficients from OCT signals [2,3]. Recently, a single scattering model was introduced for estimating attenuation coefficient,  $\mu$ , from an OCT signal  $I$  [2]:

$$\mu[i] \approx \frac{I[i]}{2 \Delta \sum_{i+1}^N I[i]}, \quad (3.1)$$

where  $i$  is the pixel index at different depths of the B-scan,  $N$  the number of pixels per A-line, and  $\Delta$  the axial pixel size. Noise in OCT systems is generally handled by subtracting the depth dependent noise floor  $N(z)$  [2]. Eq. 3.1 is only valid if the sensitivity of the OCT system does not decrease with depth. If such depth-dependent sensitivity decay exists (e.g., due to the spectrometer resolution limitation), the raw OCT data should be adjusted before estimating the attenuation coefficient. This decay, known as roll-off  $R(z)$ , has been modeled by [4]. Accordingly, the corrected OCT signal  $I(z)$  can be obtained from the raw OCT signal  $\Gamma(z)$  by  $I(z) = \Gamma(z)/R(z)$ . Fig. 3.1(a-b) show the SLO scan of the right eye of a healthy subject and the peripapillary SD-OCT circular scan, acquired by a Spectralis SD-OCT system (Heidelberg Engineering, Germany). This data was corrected for roll-off and the attenuation coefficients, shown in Fig. 3.1(c), were directly estimated using Eq. 3.1 (*Method A*).

In Eq. 3.1, the denominator depends on the depth information of the image. Fig. 3.2(a) shows a single A-line profile of the OCT data before and after compensating for roll-off. In this figure, we can observe the noise amplification at larger depth due to compensating for roll-off, which increases the effect of the noise on attenuation coefficient estimation.

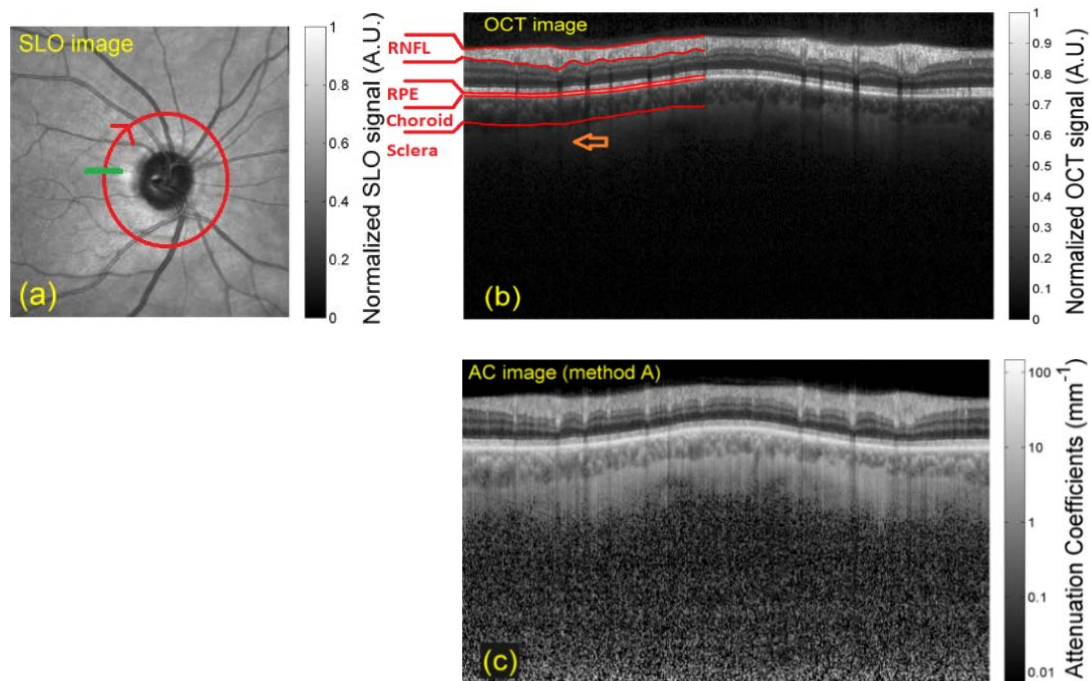


Figure 3.1 a) An en face image of the right eye's retina of a healthy subject obtained by Scanning Laser Ophthalmoscopy (SLO). The red circle indicates the location of the peripapillary OCT circular scan. The green bar indicates the starting point of the scan; b) peripapillary OCT circular scan after rescaling the intensities by  $\sqrt[4]{\cdot}$  for display purposes based on the manufacturer's recommendation; c) the attenuation coefficient (AC) image after  $\log(\cdot)$  scaling.

Fig. 3.2(b) shows the cumulative sum of the OCT signal as a function of the distance to the bottom of the image for four neighboring A-lines. Below the retinal pigment epithelium (RPE), we can see that the cumulative sum of the noise, which is part of the denominator of Eq. 3.1, is non-zero and varies strongly between neighboring A-lines. A positive non-zero noise average below the choroidal region results in an erroneous increase of the denominator of Eq. 3.1 and consequently in underestimation of the attenuation coefficients. The noise subtraction step should ideally sets the average of the noise part of each A-line to zero and thereby avoid noise propagation into the estimated attenuation coefficient. However, due to changes of the system components over time, the depth-dependent noise floor varies, which results in a non-zero mean and an inaccurate estimation of the attenuation coefficients.

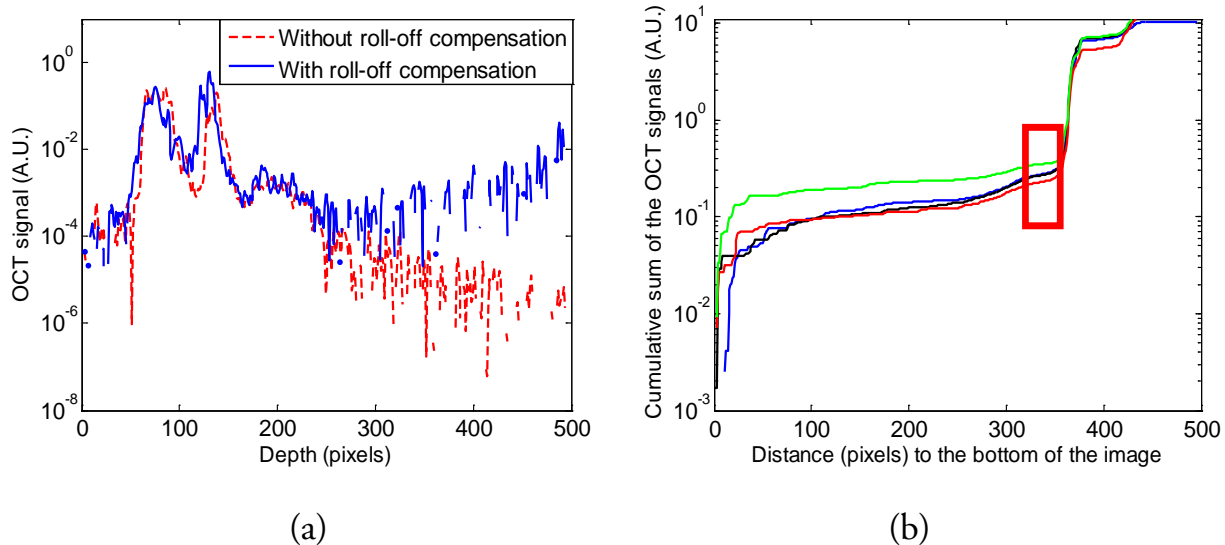


Figure 3.2 a) Depth profile of a single A-line before and after compensating for roll-off; b) cumulative sum of OCT pixel values of four neighboring A-lines in different colors (shown by an arrow in Fig.3.1(b)) as a function of the distance to the bottom of the image. The red rectangle shows the choroidal region of the A-lines.

Additionally, in SD-OCT scanners such as Spectralis and RT-100 (OptoVue, USA), negative pixel values are clipped and set to zero, thereby creating a bias with a considerable positive mean. This in turn causes a positive bias in the denominator of Eq. 3.1, which results in the underestimation of the attenuation coefficients of the chorioretinal structures.

In this chapter, we will present and evaluate two different approaches to remove the bias and reduce the intra-scan variations of the estimated attenuation coefficients, with particular interest for the sub-RPE region, namely the choroid and sclera. In the first approach, an averaged noise signal will be subtracted from the corrected OCT signal for roll-off. In the second approach, we exclude the signal from the region below the retina where the OCT signal drops below the noise floor. We will evaluate and compare these methods quantitatively by computing the intra- and inter-A-line variability of the estimated attenuation coefficients in the retinal nerve fibre layer (RNFL), the RPE, choroid and sclera, as well as by evaluating the estimated attenuation coefficient values in the RNFL and the RPE.

## 3.2 Methods

In this section, two possible solutions are presented to remove the bias and reduce the variation of the estimated attenuation coefficients.

### 3.2.1 Subtracting the average noise signal (Method B)

As mentioned in Section 1, the truncation of the negative values causes a non-zero mean or bias for the noise part of each A-line. Therefore, one may suggest to remove this bias by setting the mean of the noise to zero. The bias was estimated by averaging over a large number of A-lines while having no sample in the sample arm. In the next step, the estimated bias was subtracted from the corrected OCT data and the attenuation coefficients were estimated using Eq. 3.1.

### 3.2.2 Excluding the noise region (Method C)

We propose a method to detect the region where the noise dominates over the signal and exclude this from the attenuation coefficient estimation. In practice, we collect a negligible amount of scattered light from this region; hence the statistics are heavily influenced by the processed noise. In the first step, a region of interest (ROI) below the retina was indicated by segmenting the RPE using the Spectralis segmentation software. As mentioned before, the manufacturer already subtracted the noise level from the raw OCT signal after which all negative values were clipped to zero.

Therefore, the location of the first zero per A-line in the ROI marks the start of the noise region below the retina. To avoid outliers, the location of the first zero-valued pixels in neighboring A-lines was taken into account. For this, a local regression using weighted linear least-squares and a second-order polynomial model was used to smooth the detected data points (Curve Fitting Toolbox, MATLAB 2013; The MathWorks, Natick, MA). Afterwards, the region below the assigned smoothed curve was excluded and the attenuation coefficients were estimated using Eq. 3.1, after compensating for roll-off.

### 3.2.3 Evaluation of different methods

To investigate which method results in a better estimation of the attenuation coefficients, the median — which is less sensitive to outliers than the mean — of the attenuation

coefficients within the RNFL and the RPE was computed for all methods. In this procedure, the A-lines crossing blood vessels were detected by thresholding the intensity values of the RPE and a few pixels above it. These A-lines have a lower intensity pixel value in the regions below blood vessels and were therefore excluded from the RNFL. Additionally, the intra-B-scan variations of the estimated attenuation coefficients are assessed quantitatively. For this, the average relative inter-A-line variations  $S$  between adjacent A-lines inside a ROI were calculated per scan,

$$S \equiv \frac{1}{\Omega} \sum_{i=1}^N \sum_{j=1}^M \left| \frac{\mu_{i,j} - \mu_{i,j+1}}{\frac{1}{2}(\mu_{i,j} + \mu_{i,j+1})} \right|, \quad (3.2)$$

and the intra-A-line variations  $T$  inside a ROI were calculated by,

$$T \equiv \frac{1}{\Omega} \sum_{j=1}^M \sum_{i=1}^N \left| \frac{\mu_{i,j} - \mu_{i+1,j}}{\frac{1}{2}(\mu_{i,j} + \mu_{i+1,j})} \right|, \quad (3.3)$$

where  $\mu_{i,j}$  is the estimated attenuation coefficient of pixel number  $i$  for A-line  $j$ , and  $M$  and  $N$  are the number of A-lines and number of pixels per A-line in the ROI, respectively.  $\Omega$  indicates the number of pixels in the region of interest. The  $S$  and  $T$  metrics of the attenuation coefficients within the RNFL, RPE, choroid and sclera were calculated separately for each scan and method.

### 3.3 Experiments and results

Four peripapillary circular scans of a healthy subject were acquired consecutively with a Spectralis SD-OCT system at the Rotterdam Eye Hospital, The Netherlands. The Spectralis has a light source with a central wavelength of 870 nm. The scan protocol combined 768 A-lines of 496 pixels into a single B-scan. The system uses an eye tracker to average 16 B-scans. The pixel size is 3.9x11.3  $\mu\text{m}^2$  in  $z$  and  $x$  directions, which are the axial and the lateral axes, respectively.

The roll-off parameter  $w$  of our system was determined by fitting the roll-off model [4] to OCT signals generated by putting a uniform scattering sample at different depths in

the sample arm and by changing the optical path length of the reference arm accordingly. This value was estimated to be 1.9 for our system.

### 3.3.1 Removing the average noise signal (method B)

The bias of the system was acquired by having no sample in the sample arm and averaging the A-lines of 5 B-scans. The bias was subtracted from the OCT data. Fig. 3.3(a) shows a larger variation between the cumulative sum of the OCT signals of neighboring A-lines compared to Fig. 3.2(b), after removing the bias and compensating for roll-off. Fig. 3.4(a) shows the estimated attenuation coefficient map using Eq. 3.1.

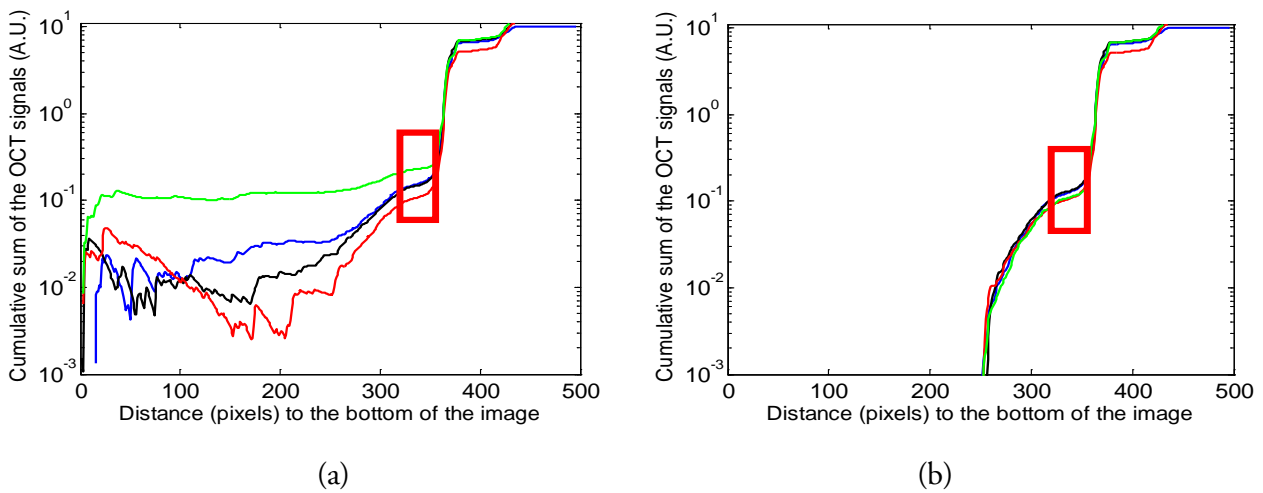


Figure 3.3 Cumulative sum of OCT pixel values corresponding to A-lines in Fig. 3.2; (a) after subtracting the bias from the corrected OCT data for roll-off (*method B*); (b) after removing the noise part at larger depths with our proposed method (*method C*). The red rectangle shows the choroidal region.

### 3.3.2 Excluding the noise region (method C)

Fig. 3.4(b) shows the location of the first zero-valued pixel below the RPE per A-line. In this figure, the green curve is the response of the weighted linear least-squares using a size of 5% of the number of A-lines (38 data points), which provides a regularized segmentation of the noise region. Fig. 3.3(b) shows a smaller variation between the cumulative sum of the OCT signals of the neighboring A-lines compared to Fig. 3.2(b). The segmented noise region was excluded and the attenuation coefficient was estimated by Eq. 3.1 (Fig. 3.4(c)).

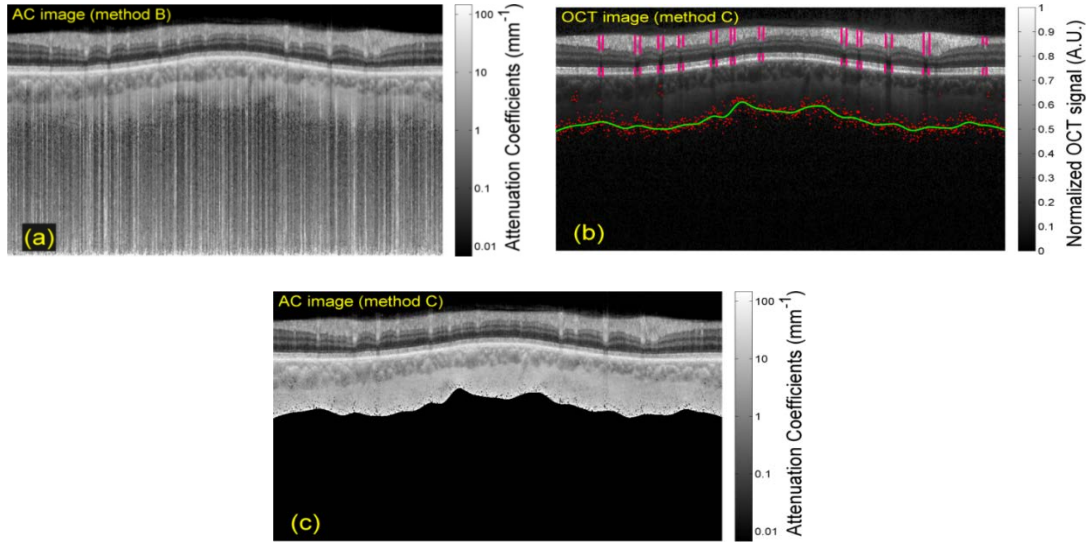


Figure 3.4 (a) The attenuation coefficient image after the bias was subtracted from Raw OCT scan and compensating for roll-off. (b) The location of the first zero-valued pixel, detected after the RPE, per A-line are shown as red points. In this figure the smoothed curve in green is the response of the weighted linear least-squares fit. The detected blood vessels are shown in between the vertical pink lines in the RPE and RNFL. (c) Attenuation image estimated by Eq. 3.1 after removing the noise part of the image.

### 3.3.3 Evaluation of the methods

To investigate which method results in a better estimation of the attenuation coefficients, the blood vessels were detected and excluded in computing the performance metrics in the RNFL. Then, the median values of the estimated attenuation coefficients for the RNFL and the RPE were computed (Table 3.1). This table shows that removing the noise region increases the estimated attenuation coefficients as expected. We therefore consider the larger attenuation coefficients of methods B and C to be more accurate. The  $S$  and  $T$  metrics of Eq. 3.2 and Eq. 3.3 were computed for the RNFL, RPE, choroid and sclera, for each scan and all methods. The RPE and RNFL were segmented using the Spectralis segmentation software. The interface between choroid and sclera was delineated manually and the choroid and a part of the sclera (between this interface and the curve obtained in section 3.2) were segmented. Table 3.2 shows the inter-A-line variation  $S$  for all scans

Table 3.1 The median of the estimated attenuation coefficients within the RNFL and the RPE for different scans and different methods.

Layer	Method	Scan1	Scan2	Scan3	Scan4
RNFL	A	2.09	2.08	2.26	2.37
	B	2.11	2.08	2.30	2.41
	C	2.13	2.13	2.31	2.42
RPE	A	29.89	27.81	31.08	27.83
	B	33.09	30.96	34.04	30.81
	C	33.75	32.23	34.86	31.77

and methods. The results show that the inter-A-line variation is lower for method C compared to the other methods in the RPE, choroid and sclera. In the RNFL no difference can be observed. This improvement is most significant in the sub-RPE region: choroid and sclera. This may contribute to better visualization and segmentation of choroidal and scleral pathology. The attenuation coefficients are more accurately estimated by excluding the noise region or removing the average noise signal from the A-lines compared to the baseline method. Other causes of variation in the computed attenuation coefficient values are under investigation and will be presented in our future work. Table 3.3 shows the intra-A-line variation  $T$  for all scans and methods. The results show that the intra-A-line variation is lower for method C compared to the other methods in the sclera. In the RNFL, RPE and choroid all methods yield the same inter-A-line variation.

### 3.4 Conclusion

In this chapter, we presented and evaluated two different approaches to handle the variation of the attenuation coefficients. Our results show that subtracting the bias from the OCT data increases the inter- and intra-A-line variation of the estimated attenuation coefficients. On the other hand, excluding the noise region improves the quality of the attenuation coefficient images significantly and reduces the inter- and intra-A-line variation of the estimated ACs. This improvement is most significant in the sub-RPE

region: choroid and sclera. This may contribute to better visualization and segmentation of choroidal and scleral pathology. The ACs are more accurately estimated by excluding the noise region or removing the average noise signal from the A- lines compared to the baseline method. Other causes of variation in the computed AC values are under investigation and will be presented in our future work.

Table 3.2 The  $S$  values (Eq. 3.2) for different layers, scans and methods. The winner method is printed in bold face (M\*: Method)

Layer	M*	Scan1	Scan2	Scan3	Scan4	Mean±SD
	A	0.27	0.42	0.34	0.23	0.31±0.01
RNFL	B	0.27	0.42	0.34	0.23	0.31±0.01
	C	0.27	0.42	0.34	0.23	0.31±0.01
	A	0.35	0.47	0.35	0.40	0.39±0.01
RPE	B	0.35	0.48	0.35	0.40	0.39±0.02
	<b>C</b>	<b>0.34</b>	<b>0.46</b>	<b>0.34</b>	<b>0.39</b>	<b>0.38±0.01</b>
	A	0.44	0.44	0.42	0.46	0.44±0.02
Choroid	B	0.91	0.66	0.64	0.81	0.75±0.04
	<b>C</b>	<b>0.41</b>	<b>0.42</b>	<b>0.39</b>	<b>0.43</b>	<b>0.41±0.01</b>
	A	0.71	0.65	0.69	0.71	0.69±0.01
Sclera	B	4.17	3.79	3.40	4.05	3.88±2.67
	<b>C</b>	<b>0.64</b>	<b>0.58</b>	<b>0.62</b>	<b>0.65</b>	<b>0.62±0.01</b>

Table 3.3 The  $T$  values (Eq. 3.3) for different layers, scans and methods. The winner method is printed in bold face.

Layer	M*	Scan1	Scan2	Scan3	Scan4	Mean $\pm$ SD
RNFL	A	0.21	0.30	0.24	0.18	0.23 $\pm$ 0.01
	B	0.21	0.30	0.24	0.18	0.23 $\pm$ 0.01
	C	0.21	0.30	0.24	0.18	0.23 $\pm$ 0.01
RPE	A	0.31	0.37	0.30	0.33	0.32 $\pm$ 0.01
	B	0.31	0.37	0.30	0.33	0.32 $\pm$ 0.02
	C	0.31	0.37	0.30	0.33	0.32 $\pm$ 0.01
Choro id	A	0.25	0.28	0.24	0.27	0.26 $\pm$ 0.02
	B	0.36	0.39	0.43	0.84	0.50 $\pm$ 0.24
	C	0.25	0.28	0.24	0.27	0.26 $\pm$ 0.01
Sclera	A	0.43	0.42	0.43	0.44	0.43 $\pm$ 0.01
	B	1.54	1.13	1.86	1.88	1.60 $\pm$ 0.67
	C	<b>0.41</b>	<b>0.39</b>	<b>0.40</b>	<b>0.41</b>	<b>0.40<math>\pm</math>0.01</b>

## References

- [1] K. A. Vermeer, J. van der Schoot, H. G. Lemij, and J. F. de Boer, "RPE-normalized RNFL attenuation coefficient maps derived from volumetric OCT imaging for glaucoma assessment, " *Investigative Ophthalmology & Visual Science*, Cadmus USA, **53**, pp. 6102-6108 (2012).
- [2] K. A. Vermeer, J. Mo, J. J. Weda, H. G. Lemij, and J. F. de Boer, "Depth-resolved model-based reconstruction of attenuation coefficients in optical coherence tomography," *Biomedical Optics Express*, Optical Society of America, USA, **5**, 322-337 (2013).
- [3] D. J. Faber, F. J. van der Meer, M. C. G. Aalders, and T. G. van Leeuwen, "Quantitative measurement of attenuation tomography," *Optics Express*, Optical Society of America, USA, **12**, 4353-4365 (2004).

[4] S. H. Yun, G. J. Tearney, B. E. Bouma, B. H. Park, and J. F. de Boer, "High-speed spectral-domain optical coherence tomography at 1.3  $\mu$ m wavelength," *Optics Express*, Optical Society of America, USA, **11**, pp. 3598-3604 (2003).

# 4 Analysis of attenuation coefficient estimation in Fourier-domain OCT of semi-infinite media

---

The attenuation coefficient is an optical property of tissue that can be estimated from optical coherence tomography (OCT) data. In this chapter, we aim to estimate the attenuation coefficient accurately by compensating for the shape of the focused beam. For this, we propose a method to estimate the axial PSF model parameters and attenuation coefficient by fitting a model for an OCT signal in a homogenous sample to the recorded OCT signal. In addition, we employ numerical analysis to obtain the theoretical optimal precision of the estimated parameters for different experimental setups. Finally, the method is applied to OCT B-scans obtained from homogeneous samples. The numerical and experimental results show accurate estimations of the attenuation coefficient and the focus location when the focus is located inside the sample.

B. Ghafaryasl, k. A. Vermeer, J. Kalkman, T. Callewaert, J. F. de Boer, L. J. van Vliet, Analysis of attenuation coefficient estimation in Fourier-domain OCT of semi-infinite media, *Biomed. Opt. Express*, **11**, 6093-6107 (2020).

## 4.1 Introduction

Optical coherence tomography (OCT) has been widely used to capture structural information of tissues in clinical tasks such as the diagnosis of retinal and vascular diseases. Previously, extracting valuable information embedded in the signal intensity of constituting tissues has been investigated. An optical property such as the attenuation coefficient (AC) offers valuable information that can be estimated from the intensity of the OCT signal. It has the potential to act as a biomarker for the diagnosis and monitoring of chorioretinal diseases [1], breast tumor lesions [2], renal tumors [3,4], oral cancer [5], rectal cancer [6] and several other applications such as atherosclerotic plaque characterization [7-9]. Several methods based on single [10,11,12] and multiple [13,14] scattering of light have been presented for estimating the attenuation coefficient in a homogeneous medium using OCT. Recently, a depth-resolved single-scattering based method has been developed by Vermeer *et al.* [15] for estimating attenuation coefficients in inhomogeneous mediums, e.g. in tissues. For all methods that estimate the attenuation coefficient, the OCT signal must be corrected for: 1) the depth-dependent noise floor [16]; 2) the so-called roll-off, i.e. the depth-dependent signal decay caused by discrete signal detection and resolution limitations of the detection process [15,17]; and 3) the axial point spread function (PSF), which, for a Gaussian-shaped beam, is governed by the effective Rayleigh length around the focus position of the beam [15,18]. Compensation for noise and roll-off is nowadays a standard procedure, which can be done with a function obtained from a fit to reference data [17]. However, in order to correct for the axial PSF, in many cases its model parameters need to be estimated from the acquired data since the effective Rayleigh length and focus depend on the optical system, e.g. in case the cornea and lens. We showed in previous work how the attenuation coefficient is sensitive to an error in the estimated parameters of the axial PSF model [19]. Therefore, accurate and precise estimation of these parameters is required to achieve an unbiased and precise estimation of attenuation coefficient. Various methods have been developed to estimate the attenuation coefficient of the tissue while taking into account the effect of the beam shape that influence the acquired OCT signal. Smith *et al.* [20] compensate for the effect of focus using an existing model of the shape of the beam.

However, in their work the parameters of the shape of the beam need to be known in advance. In many medical applications, such as ophthalmology, the location of the focal point varies and there is a need for a method to automatically estimate the focus location to compensate for the effect of the beam shape in the estimation of the attenuation coefficient. Stefan et al. [21] introduced a method to estimate the attenuation coefficient using two B-scans to first estimate the location of focus and afterwards estimating the attenuation coefficient from a single scattering model of the OCT light after compensating for the effect of beam shape. This method is dependent on having identical A-lines to be able to eliminate the effect of attenuation coefficients. However, this proposed method was only tested with static samples where the identical physical location in both B-scans is feasible and the factors such as beam's angle of incidence can be controlled to ensure a similar tissue attenuation coefficient. Another limitation of this method is the necessity to have access to two scans from the same position in the tissue. However, in many clinical data, such as retinal scans, only one averaged measurement of the same tissue's location is available.

In this chapter, we aim to achieve an accurate estimate of attenuation coefficient by compensating for all of the aforementioned effects on the recorded OCT signal. To do so, we propose a method to estimate the axial PSF model parameters (focus depth and Rayleigh length in the medium) and attenuation coefficient by fitting a single scattering based model for a homogenous sample OCT signal to the recorded OCT signal after subtraction of the depth-dependent noise floor and compensating for roll-off. In addition, a Cramér-Rao analysis is performed to theoretically determine the attainable precision of the estimated parameters and to investigate the limitations of the proposed procedure for various experimental configurations. Monte Carlo simulations of the estimation method are performed to evaluate the robustness of the method and compare the precision of the theoretical lower bound produced by the Cramér-Rao analysis and to show a possible bias in the estimated parameters. Finally, the method is applied to B-scans obtained with an experimental OCT system from homogeneous samples with various concentrations of  $\text{TiO}_2$  particles dispersed in silicone to assess the precision and accuracy of the method.

## 4.2 Method

In this section, we introduce a method for accurate estimation of the attenuation coefficient in a homogenous (or single layer) sample by compensating the recorded OCT signal for the noise floor, roll-off, and axial PSF.

### 4.2.1 Estimating the model parameters

In a single scattering model of light presented by Faber et al. [22], the Fourier-domain OCT signal at physical depth  $z$  in a homogeneous sample may be expressed by,

$$S(z) = R(z) \frac{1}{\left(\frac{z - z_0}{2z_R}\right)^2 + 1} C e^{-2\mu z} + N(z) + \varepsilon(z), \quad (4.1)$$

where the first term models the signal decay caused by three factors (from left to right): the roll-off (expressed by  $R(z)$ ), the axial PSF modeled by a Cauchy function at focus position  $z_0$  and scaled by the Rayleigh length  $z_R$  [18], and the signal attenuation modeled by the attenuation coefficient  $\mu$  and scaling factor  $C$ . The second term,  $N(z)$  is the depth-dependent noise floor and can be obtained by averaging over a large number of A-lines without a sample in the sample arm of the OCT system. The intensity of the OCT signal has an exponential distribution caused by speckle noise. However, due the central limit theorem, by averaging over a sufficiently large number of neighboring A-lines (>30 based on rule of thumb) with exponential distributions, the averaged OCT signal at depth  $z$  tends toward a normal distribution  $\mathcal{N}[m(z), m(z)^2/N]$ , with  $m(z)$  being the expected value of the exponential distribution, and  $m(z)^2/N$  the variance of the resulting normal distribution. The third term  $\varepsilon(z)$  represents this speckle noise. In addition, the roll-off can be measured and the signal can be corrected for roll-off by performing the operation  $A(z) = (S(z) - N(z)) / R(z)$  [15].

We estimate the model parameters of the axial PSF and the attenuation coefficient using a maximum likelihood estimator. For this, Eq. 4.1 was fitted to the measurements. For an averaged A-line  $A(z)$  with  $N_D$  data-points as a function

of  $z$ , the independent parameters  $C$ ,  $\mu$ ,  $z_0$  and  $z_R$  can be estimated by minimizing the sum of squared residuals,  $\chi$ , given by,

$$\chi = \sum_{j=1}^{N_D} \left[ A(z_j) - C \frac{e^{-2\mu z_j}}{\left( \frac{z_j - z_0}{2z_R} \right)^2 + 1} \right]^2, \quad (4.2)$$

where subscript  $j$  is an index that denotes the data-point number on each averaged A-line.

#### 4.2.2 Model selection and evaluation

To design a reliable model-based method for estimating the axial PSF from recorded data, we studied the influence of integrating prior information into the model, such as a known or joint model parameter among multiple averaged A-lines, to reduce the degrees of freedom and aiming to thereby improve the estimation precision of the remaining parameters. Moreover, the attainable precision of the estimated parameters  $\{\theta_1, \dots, \theta_N\} = \{C, \mu, z_0, z_R\}$  needs to be calculated for various experimental setups. Exploring the precision of the estimated parameters such as the focus depth into the sample, the Rayleigh length, illumination intensity and the attenuation coefficient of the medium, enables us to optimize the experimental design and to know the limitations of the proposed method. For these purposes, a Cramér-Rao analysis was applied using a derivation of the Fisher information matrix for a Gaussian noise model (see equations 9-11 from Caan et al. [23]). Cramer-Rao analysis is limited to finding the minimal variance of the model parameters assuming an unbiased estimator. To evaluate the optimal precision of the estimated parameters and to compare different models and experimental setups, we use the relative errors, as provided by the diagonal elements of the relative Cramér-Rao lower bound (rCRLB) matrix [23]. The diagonal elements are the relative theoretical lower bounds on the variance of the unbiased estimators of each parameter. We intuitively considered an estimation error lower than 10% to be acceptable for the purpose of this chapter.

Multiple averaged A-lines can be used to estimate the model parameters. For this, let  $A(z) = \{A_1(z), A_2(z), \dots, A_{N_A}(z)\}$  be a set of  $N_A$  averaged A-lines with  $N_D$  data-points on each A-line. For a matrix of  $N_A \times N_D$  averaged A-lines, any unknown parameter among  $C, \mu, z_0, z_R$  can be estimated by minimizing the sum of squared residuals,  $\chi$ , given by,

$$\chi = \sum_{i=1}^{N_A} \sum_{j=1}^{N_D} \left[ A_i(z_j) - C \frac{e^{-2\mu z_j}}{\left( \frac{z_j - z_0}{2z_R} \right)^2 + 1} \right]^2, \quad (4.3)$$

where the parameters can be considered to be common (joint), fixed (known) or independent among the averaged A-lines. Table 1 lists seven models with different degrees of freedom by defining some of the parameters fixed (known), or by defining them as a common (joint) parameter to be estimated among different averaged A-lines. Such an evaluation assists us in choosing the model with the highest estimation precision while considering the feasibility of its implementation under experimental conditions. In Cramér-Rao analysis due to interdependency between the averaged A-lines, we assume that having a fixed or common parameter is equivalent since compared to the variance of the estimated parameters for every

Table 4.1 Overview of different OCT signal models with different degrees of freedom (DOF). The unknown independent parameters among the averaged A-lines which need to be estimated are indicated by “Indep.” and the fixed (known) or common (joint) parameters are shown by “Fix/Com.” in the table.

Parameter	Model 1	Model 2	Model 3	Model 4	Model 5	Model 6	Model 7
$C$ (arb. units)	Fix/Com.	Fix/Com.	Indep.	Fix/Com.	Indep.	Indep.	Indep.
$\mu$ ( $\text{mm}^{-1}$ )	Indep.	Indep.	Indep.	Indep.	Indep.	Indep.	Indep.
$z_0$ ( $\mu\text{m}$ )	Fix/Com.	Indep.	Fix/Com.	Indep.	Fix/Com.	Indep.	Indep.
$z_R$ ( $\mu\text{m}$ )	Indep.	Fix/Com.	Fix/Com.	Indep.	Indep.	Fix/Com.	Indep.
DOF	2	2	2	3	3	3	4

averaged A-line, the amount of joint information is large. Therefore, we expect the error we estimate for fixed parameters to be a good approximation of the error that we obtain in the estimation of common (joint) parameters.

In the next step, we used Monte Carlo simulations to show a possible bias and investigate if the simulations achieve the precisions given by the Cramér-Rao bound. This was performed by generating a large set of simulated OCT signals using Eq. 4.1 and estimating the model parameter with the proposed method for different parameter values.

### 4.3 Results

In this section, we first present the statistical analysis and numerical simulations to study the performance of the different models in Table 4.1 and estimation method using Cramér-Rao analysis and Monte Carlo simulation, respectively. This provides insight into the available information embedded in the data for different experimental setups and models with different degrees of freedom. Finally, we present the experimental results on a homogeneous phantom to assess the real-life performance of the proposed method.

#### 4.3.1 Model selection by Cramér-Rao analysis

A Cramér-Rao analysis was performed to assess the amount of information present in the data and the impact thereof on the attainable precision for all model parameters. Eq. 4.1 was used to simulate OCT depth profiles. A simulated (thick) homogeneous sample with a refractive index of 1.44, a physical thickness of 1 mm and an attenuation coefficient of  $0.72 \text{ mm}^{-1}$  was located at the zero-delay line. The model parameters in Eq. 4.1 were set to  $z_R = 42 \text{ }\mu\text{m}$ ,  $C = 2.5 \times 10^4$  and  $z_0 = 160 \text{ }\mu\text{m}$  inside the sample. Each A-line consisted of 788 pixels and the physical axial pixel size  $\Delta z$  of the system in air was set to  $1.27 \text{ }\mu\text{m}$ . For a realistic simulation, the OCT signal was distorted by exponential noise with the intensity-dependent mean at each depth, equal to the expected values of  $S(z)$  in Eq. 4.1. To reduce the noise, we averaged over single A-lines as explained in section 2.1. An example of a simulated single A-line is presented in Fig. 4.1(a), together with an averaged (over 500 simulated A-lines) OCT signal. The noise of the averaged A-line resembles an intensity-dependent Gaussian distribution due to the central limit theorem. We

obtained the intensity-dependent standard deviations for all averaged A-lines using 1000 observations of the simulated averaged-A-lines. In Fig. 4.1(b), we show the rCRLB values after averaging  $N$  single A-lines. The diagonal elements of the rCRLB matrix represent the optimal precision of the estimated model parameters for the aforementioned intensity-dependent standard deviations. As is shown, by averaging over 10 A-lines, the estimation error of  $\mu$  remains below 10%. However, in real measurements, due to the presence of the background noise which varies for different OCT systems, a larger number of averaging is required. In addition, rCRLB is the lower bound of the estimation error and in practice, as will be shown in the Monte Carlo simulation, the estimation error is larger. Averaging of 500 A-lines is therefore used for the simulated and measured OCT signals in the following sections. The calculated rCRLB matrix for the simulated signals shown in Fig. 4.2. As seen in this figure, the model parameter estimation errors remain below 5%.

In addition, we investigate the precision of the estimated parameters for different degrees of freedom imposed on the model. The diagonal elements of the

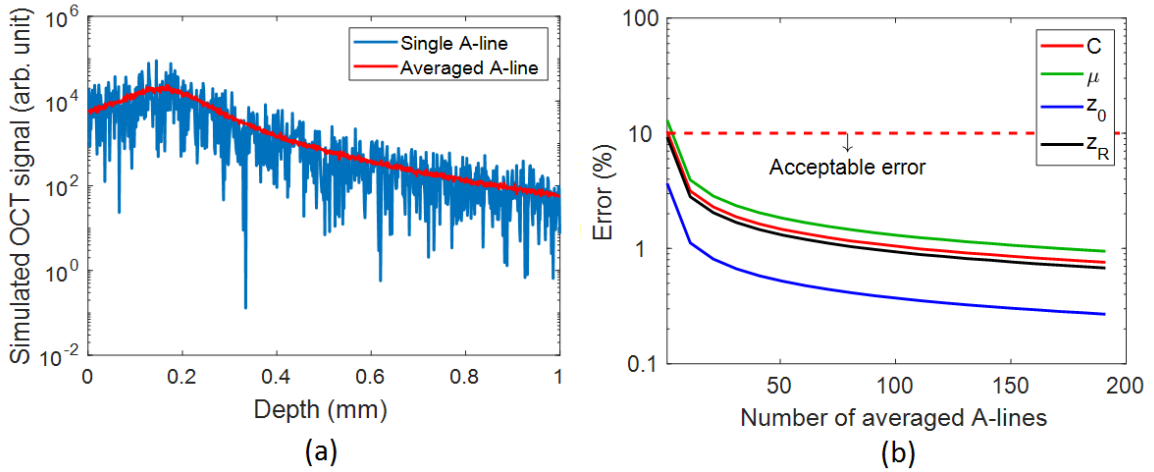


Figure 4.1 (a) The simulated single (blue) and averaged (red) OCT signals distorted by intensity-dependent Gaussian noise. The averaged OCT signal was obtained by averaging over 500 single A-lines. (b) rCRLB values after averaging 1 to 1000 A-lines. The model parameter were set to  $z_0 = 160 \mu\text{m}$ ,  $\mu = 0.72 \text{ mm}^{-1}$ ,  $C = 2.5 \times 10^4$ , and  $z_R = 42 \mu\text{m}$ .

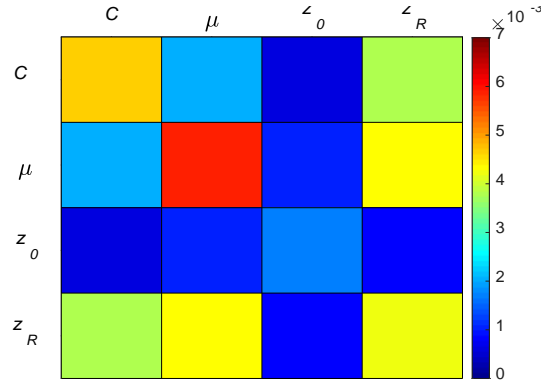


Figure 4.2 rCRLB matrices for models with intensity-dependent Gaussian noise. The model parameters were set to  $z_0 = 160 \mu\text{m}$ ,  $\mu = 0.72 \text{ mm}^{-1}$ ,  $C = 2.5 \times 10^4$ , and  $z_R = 42 \mu\text{m}$ .

rCRLB matrix for the seven models shown in Table 4.1 are depicted in Fig. 4.3. As it can be observed, incorporating prior knowledge by fixing  $z_R$  results in a better precision of parameter  $\mu$  for depth-variant noise as indicated by the smaller values for Model 1...Model 6 compared to Model 7 as defined in Table 4.1.

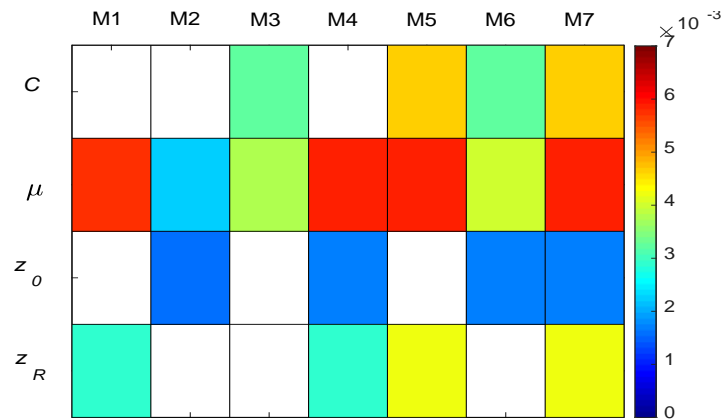


Figure 4.3 The diagonal elements of the rCRLB matrices for the seven models (M1...M7) as shown in Table 4.1.

### 4.3.2 Experiment design by Cramér-Rao analysis

To assess the attainable precision under different experimental conditions, we calculated the rCRLB matrices as a function of one of the model parameters while keeping the other ones fixed. The rCRLB values are shown in Fig. 4.4 for a range of parameter values. In this figure, the horizontal dashed lines indicate the acceptable error (below 10%) and the vertical dashed lines indicate the set parameter values in the simulation and also were considered to be fixed for the other plots in this figure.

In Fig. 4.4(a), it can be observed that the estimation error for  $\mu$  remains below 10%. The estimation errors for  $C$ ,  $z_0$  and  $z_R$  remain below 10% when the focus is located inside the sample. Fig. 4.4(b) shows that for a Rayleigh length below 500  $\mu\text{m}$  the estimation errors of  $\mu$  remains below 10%. The estimation error of  $z_0$  increases to above 10% for Rayleigh lengths larger than 400  $\mu\text{m}$ . The estimation errors for  $C$  and  $z_R$  remain below 10% for Rayleigh lengths below 500  $\mu\text{m}$ . By varying the attenuation of the sample, Fig. 4.4(c) shows that the estimation errors of the parameters remain below 10% for all the attenuation coefficient values. Fig 4.4(d) shows that by increasing the light intensity the precision of all estimated parameters remains the same due to the intensity-dependent noise.

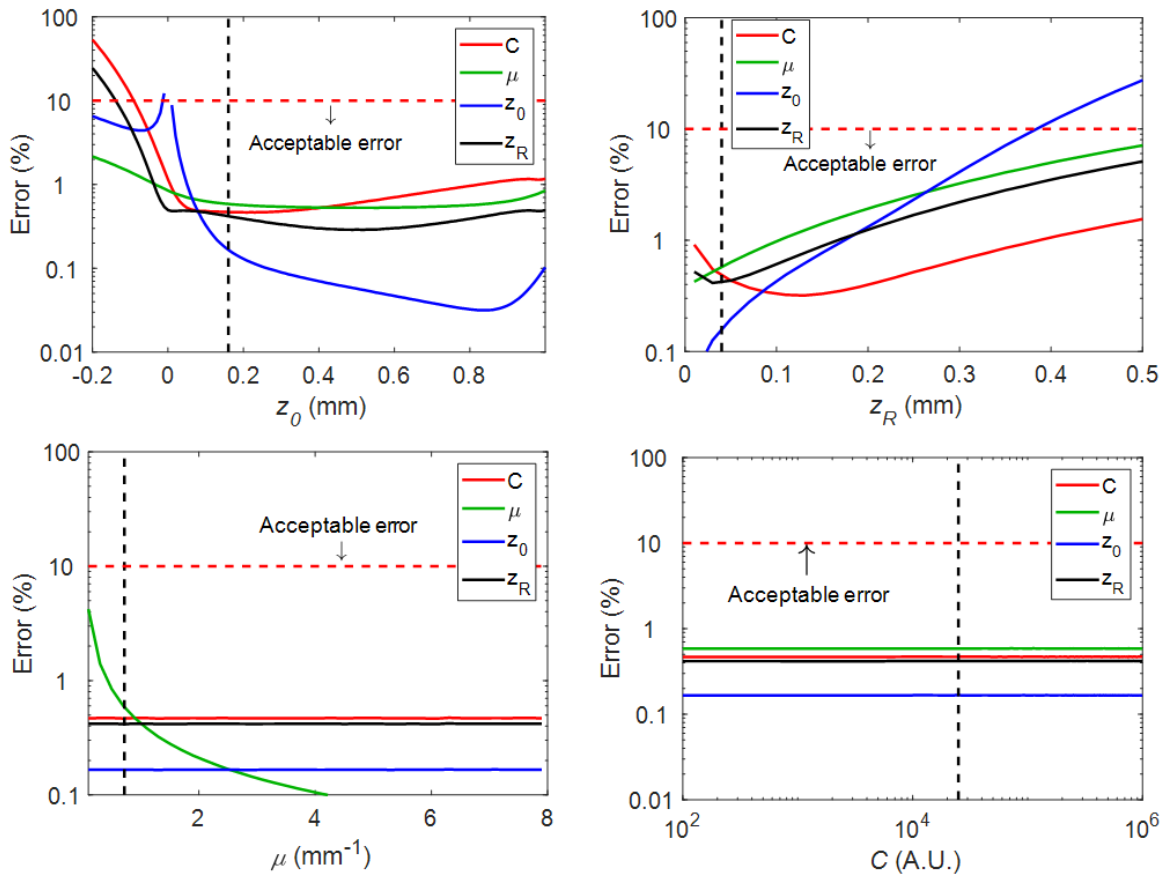


Figure 4.4 The error (%) of the estimated model parameters obtained from the diagonal elements of the rCRLB matrix for: a)  $z_R = 42 \mu\text{m}$ ,  $\mu = 0.72 \text{ mm}^{-1}$ ,  $C = 2.5 \times 10^4$  and  $z_0 = [-0.2, 0.9] \text{ mm}$ ; b)  $z_0 = 160 \mu\text{m}$  inside the sample,  $\mu = 0.72 \text{ mm}^{-1}$ ,  $C = 2.5 \times 10^4$  and  $z_R = [0.01, 0.5] \text{ mm}$ ; c)  $z_R = 42 \mu\text{m}$ ,  $z_0 = 160 \mu\text{m}$  inside the sample,  $C = 2.5 \times 10^4$  and  $\mu = [0.01, 8] \text{ mm}^{-1}$ ; d)  $z_R = 42 \mu\text{m}$ ,  $z_0 = 160 \mu\text{m}$ ,  $\mu = 0.72 \text{ mm}^{-1}$  inside the sample and  $C = [10^2, 10^6]$  (arb. units). The vertical dashed lines indicate the parameter values, which were set in the simulations and also were considered to be fixed for the other plots in this figure.

### 4.3.3 Estimation accuracy and precision: Monte Carlo simulation

To investigate if the theoretical lower bounds on the precision estimated by CRLB can be attained by our estimation method, Monte Carlo simulations were performed. In the simulated data, the location of the focus was varied between the surface and 0.6 mm inside the sample; the other model parameters were set to  $z_R = 42 \mu\text{m}$ ,  $C = 2.5 \times 10^4$  and  $\mu = 0.72 \text{ mm}^{-1}$ . Next, we simulated 500 averaged A-lines distorted by Gaussian noise with an intensity-dependent standard deviation, as explained in section 3.1, for different focus locations. The method in section 2.1 was applied to estimate the model parameters using the *fmincon* function of MATLAB [Curve Fitting Toolbox, MATLAB 2013; The MathWorks, Natick, MA] using interior-point optimization with a termination tolerance set to  $10^{-15}$ , and the maximum number of iteration and function evaluations set to  $10^5$ .

Prior knowledge of the sample under investigation in combination with known properties of the optical system are useful to set suitable initial parameter values. The initial value of  $C$  ( $2.5 \times 10^4$  (arb. unit)) was set by choosing an arbitrary A-line and taking the average of the intensity values at all depths within the sample. To investigate the effect of the initial parameter values on the estimation results, the initial parameter values were varied individually, over the following ranges:  $0.01 \text{ mm} \leq z_R \leq 0.2 \text{ mm}$ ,  $0 \text{ mm} \leq z_0 \leq 2 \text{ mm}$ ,  $10^3 \leq C \leq 7 \times 10^4$  and  $0 \text{ mm}^{-1} \leq \mu \leq 6 \text{ mm}^{-1}$ , while the other parameters were set to the aforementioned initial parameter values. Fig. 4.5 shows the CoV and bias of the estimated parameters for different settings of the initial values. As can be seen, the CoVs remain below 10% and bias error below 1%.

The coefficient of variation (CoV) of the estimated parameters in Monte Carlo simulation, the rCRLB values for different parameters and the estimation bias as a function of focus location, are shown in Fig. 4.6. For varying  $z_0$ , the initial values for the unknown parameters were set to  $z_R = 50 \mu\text{m}$ ,  $C = 2 \times 10^4$  (arb. unit),  $\mu = 1 \text{ mm}^{-1}$  and the values of  $z_0$  were set to 0.2 mm above the expected focus locations for each averaged A-line. We can observe in Fig. 4.6(a) that the estimation error of the parameters by Monte Carlo simulation is below 12% when the focus location is

inside the sample. Fig. 6(b) shows an acceptable bias error of the attenuation coefficient in the Monte Carlo simulation for all focus locations.

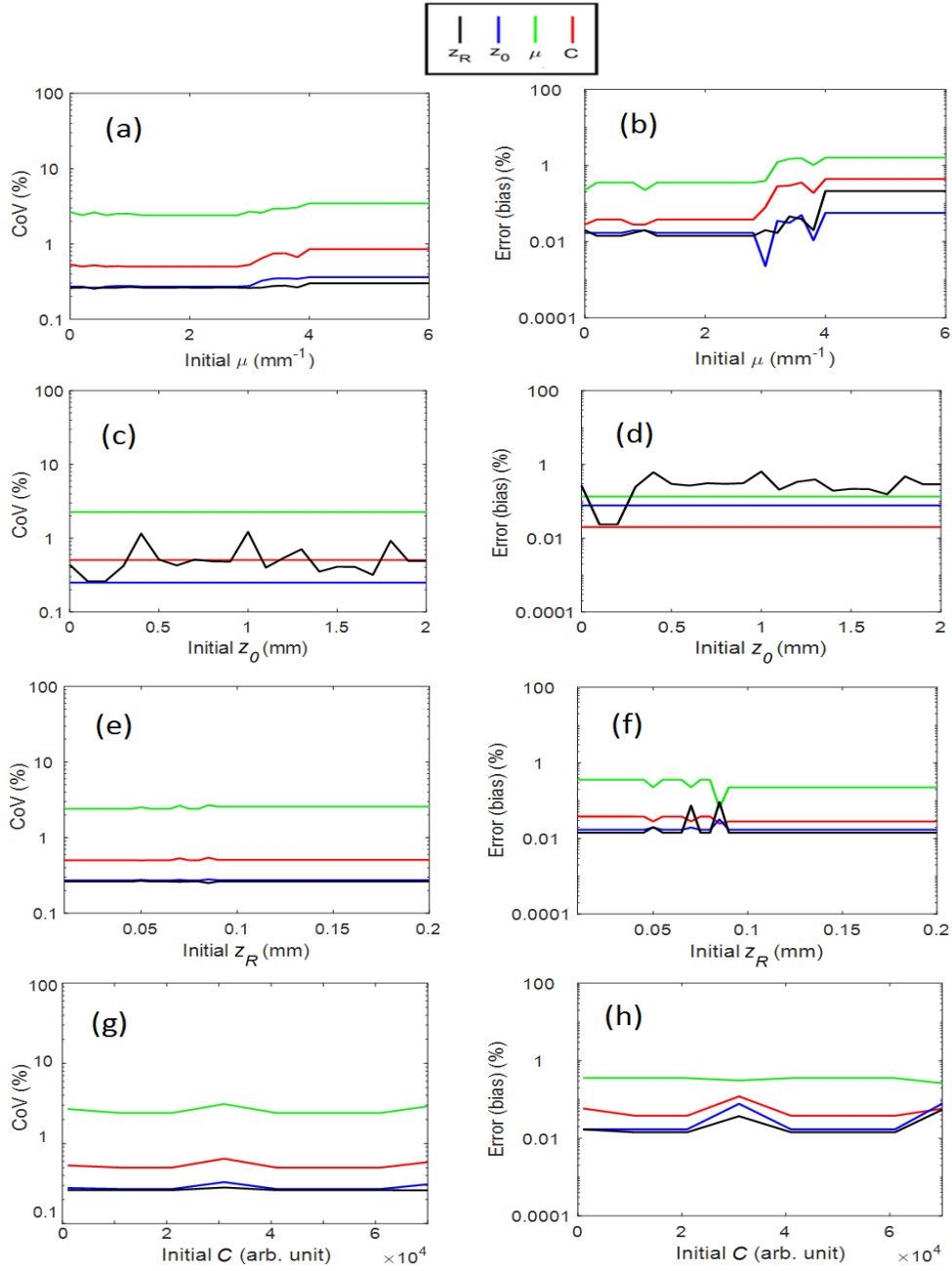


Figure 4.5 The coefficient of variation (CoV) (left column) and bias of the estimated parameters (right column) using the proposed method obtained from 100 simulated OCT signals, when initial parameter values are set to: a-b)  $0 \text{ mm}^{-1} \leq \mu \leq 6 \text{ mm}^{-1}$ ,  $z_R = 50 \text{ }\mu\text{m}$ ,  $C = 2 \times 10^4$  (arb. unit), and  $z_0 = 1 \text{ mm}$ ; c-d)  $0 \text{ mm} \leq z_0 \leq 2 \text{ mm}$ ,  $\mu = 1 \text{ mm}^{-1}$ ,  $z_R = 50 \text{ }\mu\text{m}$ , and  $C = 2 \times 10^4$  (arb. unit); e-f)  $0.01 \text{ mm} \leq z_R \leq 0.2 \text{ mm}$ ,  $\mu = 1 \text{ mm}^{-1}$ ,  $C = 2 \times 10^4$  (arb. unit), and  $z_0 = 1 \text{ mm}$ , and g-h)  $10^3 \leq C \leq 7 \times 10^4$  (arb. unit),  $\mu = 1 \text{ mm}^{-1}$ ,  $z_R = 50 \text{ }\mu\text{m}$ , and  $z_0 = 1 \text{ mm}$ . The simulated model parameters were set to  $z_R = 42 \text{ }\mu\text{m}$ ,  $C = 2.5 \times 10^4$  (arb. unit),  $\mu = 0.72 \text{ mm}^{-1}$  and  $z_0 = 0.16 \text{ mm}$ .

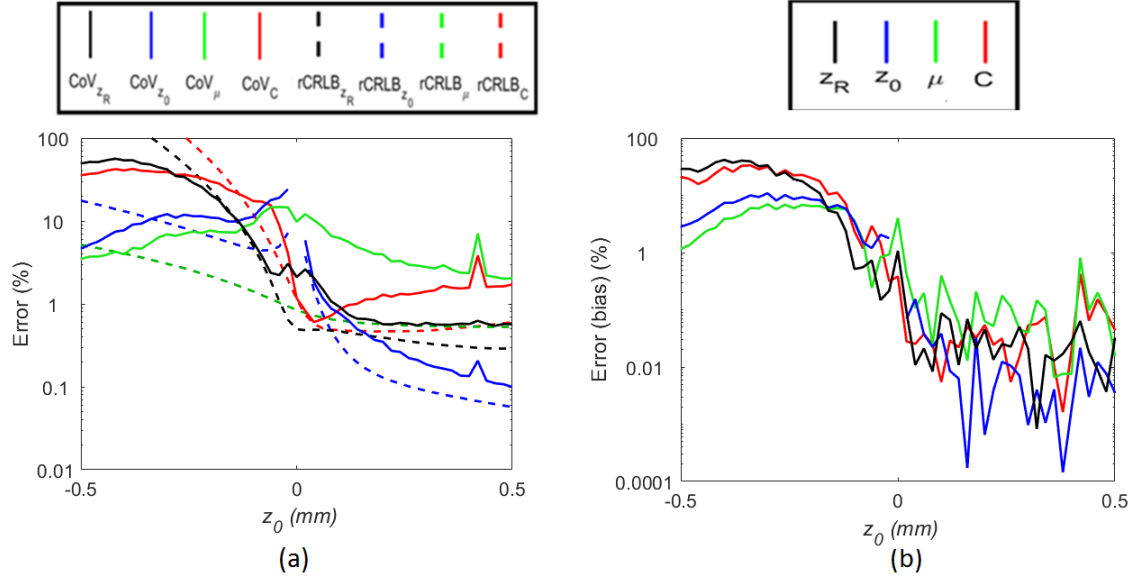


Figure 4.6 Monte Carlo simulation results: a) the coefficient of variation (CoV) of the estimated parameters (solid lines) for 500 measurements and Cramer-Rao lower bounds (dashed lines); and (b) bias of the estimated parameters as a function of focus location inside the medium.

To summarize the results, it has been shown that knowing more model parameters results in a better estimation precision of  $\mu$  (Fig. 4.3). Additionally, the proposed approach ideally can estimate the model parameters with an acceptable precision (below 10%) when the number of averaged A-lines is larger than 500, the location of the focus is inside the sample, the Rayleigh length is below 0.4 mm and the attenuation coefficient of the sample is more than  $0.2 \text{ mm}^{-1}$  and less than  $6 \text{ mm}^{-1}$  (Fig. 4.4). Therefore, these limitations for Rayleigh length and the attenuation coefficient were considered in designing our experimental setup. In addition, we obtained acceptable results using aforementioned interior-point solver. This routine was used for estimating the model parameters in the real measurements explained in the next section.

#### 4.3.4 Experimental setup

In this section, we apply our method to the measurements obtained from different samples with an experimental OCT system. We apply them to estimate the model parameters based on either single or multiple B-scans. The B-scans of three thick or semi-infinite samples with 0.05 wt. %, 0.1 wt. % and 0.25 wt. % of  $\text{TiO}_2$  in silicone, with the zero delay location positioned 0.4 mm above the sample surface,

are recorded with various locations of the focal plane from the samples' surfaces using a Ganymede-II-HR Thorlabs spectral domain OCT system (GAN905HV2-BU) [24]. The system has a centre wavelength of 900 nm and a bandwidth of 195 nm and a Thorlabs scan lens (LSM02-BB) with 18 mm focal length. The system's axial and lateral resolutions were 3  $\mu\text{m}$  (in air) and 4  $\mu\text{m}$ , respectively, and the axial and lateral physical pixel size in air was  $1.27 \times 2.9 \mu\text{m}$  with 1024 pixels on each A-line.

First, the focus position was manually set to the sample's surface by optimizing the surface structure's sharpness in the centre of enface image created by the OCT camera. Next, 90 B-scans were obtained at various locations of the focal plane by changing the axial location of the lens in the sample arm with a physical step size of 11.25  $\mu\text{m}$  within a range of  $\pm 0.5$  mm around the initial focus location as was explained in Chapter 2. Several pre-processing has been performed as explained in chapter 2 and the physical Rayleigh length in silicone was calculated to be 42  $\mu\text{m}$ .

#### Estimating the model parameters in a single B-Scan

The unconstrained model of Eq. 4.1 was fit to the averaged A-lines obtained from 500 single A-lines of each B-scan. The initial values were set to  $\mu = 3 \text{ mm}^{-1}$ ,  $C = 5 \times 10^3$ ,  $z_R = 56 \mu\text{m}$ , and the values of  $z_0$  were set to 0.2 mm above the expected focus locations for each Averaged A-line.  $z_0 = (\text{the expected focus location} - 0.2 \text{ mm})$ . The results of the fit to the measurements of 8 B-scans acquired with focus positions of  $\{-0.5, -0.3, -0.1, 0.15, 0.3, 0.45, 0.6, 0.75\}$  mm are shown in Fig. 4.7. The estimated parameter values for all recorded B-scans are shown in Fig. 4.8. Since parameters  $z_R$  and  $\mu$  are constant among the B-scans, we expect them to have similar estimated values. However, as can be seen, when the focus is above the sample, the estimated parameters are far from the expected values. Additionally, when the focus location is within the depth of 0.1 mm inside the sample, the estimated attenuation coefficients seems to be significantly different compare to their estimated values at larger depths. This also confirms the simulation results in section 3.1. For a location of focus inside the sample, the estimated focus locations closer to the surface are in better agreement with the expected focus locations than for focus positions very deep into the sample.

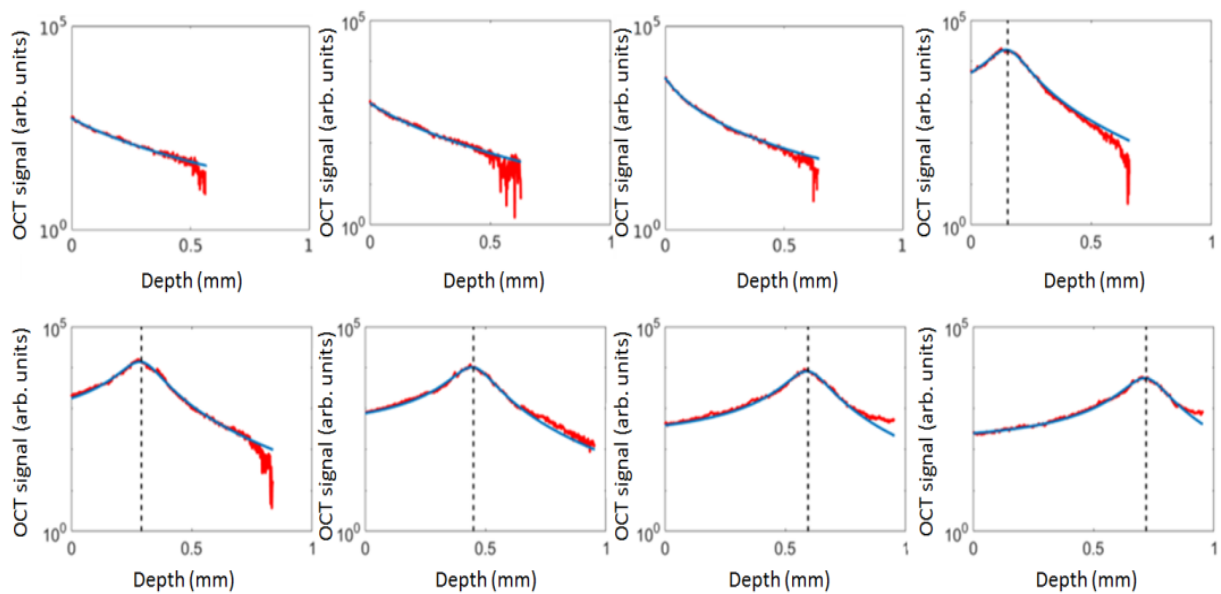


Figure 4.7 The result of fitting the constrained model (blue) to the averaged A-lines per B-scan (red) obtained from the sample with 0.05 wt. %  $\text{TiO}_2$  in silicone for eight different focus positions  $\{-0.5, -0.3, -0.1, 0.15, 0.3, 0.45, 0.6, 0.75\}$  mm from left to right. The location of the estimated focus (within the shown depth range) is indicated by the vertical dashed line.

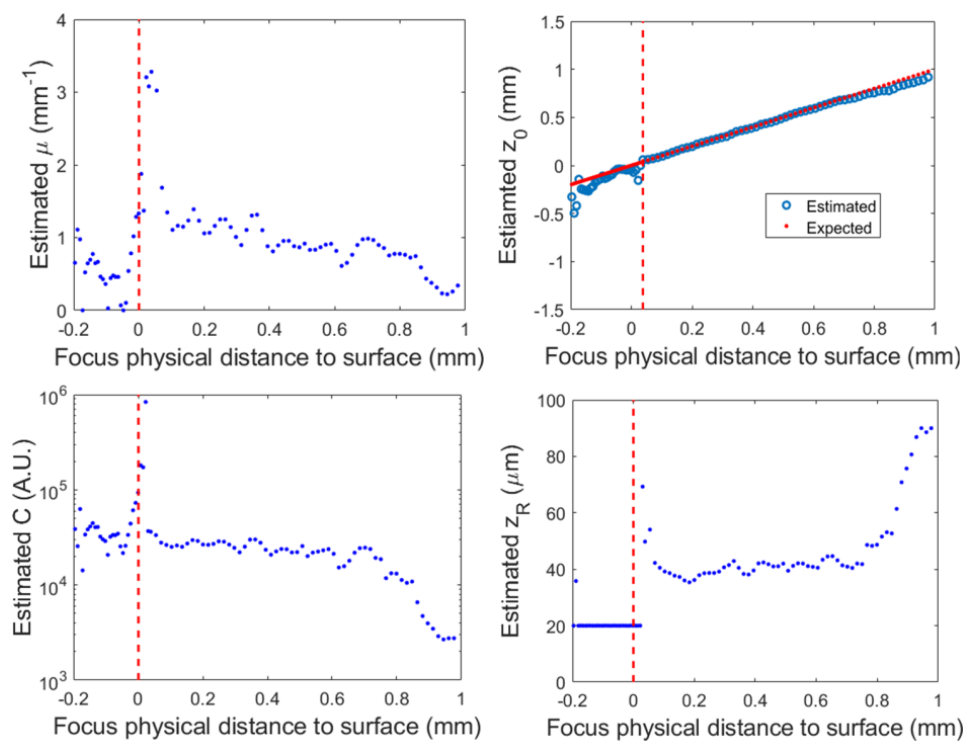


Figure 4.8 The estimated model parameters as a function of focus position obtained averaged A-lines per B-scan acquired from the sample with 0.05 wt. % TiO<sub>2</sub> in silicone. The vertical red dashed lines indicate the B-scan in which the focus was on the sample's surface.

### 4.3.5 Estimating the model parameters using multiple B-Scans

Multiple B-scans of the same sample acquired with different focus positions can also be combined to estimate the model parameters as was explained in section 2.2. In this case, the model parameters  $\mu$  and  $z_R$  were considered common while the focus position  $z_0$  and  $C$  were left free to vary among the B-scans. Only the B-scans in which the focus was inside the sample were considered in this experiment. The initial parameter values of the fitting process were the same as the values mentioned in section 3.3. To investigate if the estimation result depends on the number of the B-scans used, different numbers of the B-scans (2, 4, 8, 16 and 32) acquired from the sample with 0.05 wt. % TiO<sub>2</sub> in silicone were used. The estimated parameters  $\mu$ ,  $z_R$  and  $z_0$  are shown in Fig. 4.9 for different numbers of combined B-Scans. As can be seen, the estimated attenuation coefficient and Rayleigh length do not change significantly when more than 8 B-scans were used.

We combined 8 B-scans in estimating the attenuation coefficient  $\mu$  for samples with different concentrations of TiO<sub>2</sub> in silicone (0.05 wt. %, 0.1 wt. % and 0.25 wt. %). The results are shown in Table 4.2. The standard errors for the estimated attenuation coefficients, Rayleigh lengths and the focus locations were 0.01 mm<sup>-1</sup>, 0.0001 mm, and less than 0.01 mm, respectively. In theory, the relationship between the particle concentration and the attenuation coefficient should be linear. The estimation result shows a reasonable correlation between the TiO<sub>2</sub> weight concentration and the estimated attenuation coefficient [with  $R^2 = 0.99$  calculated over all B-scans].

Table 4.2. Estimated attenuation coefficients obtained using 8 B-scans acquired with different focus positions inside the sample for three phantoms with different TiO<sub>2</sub> weight concentrations in Silicone.

TiO <sub>2</sub> conc. (wt. %)	0.05	0.1	0.25
Estimated $\mu$ (mm <sup>-1</sup> )	1.0	2.1	4.4

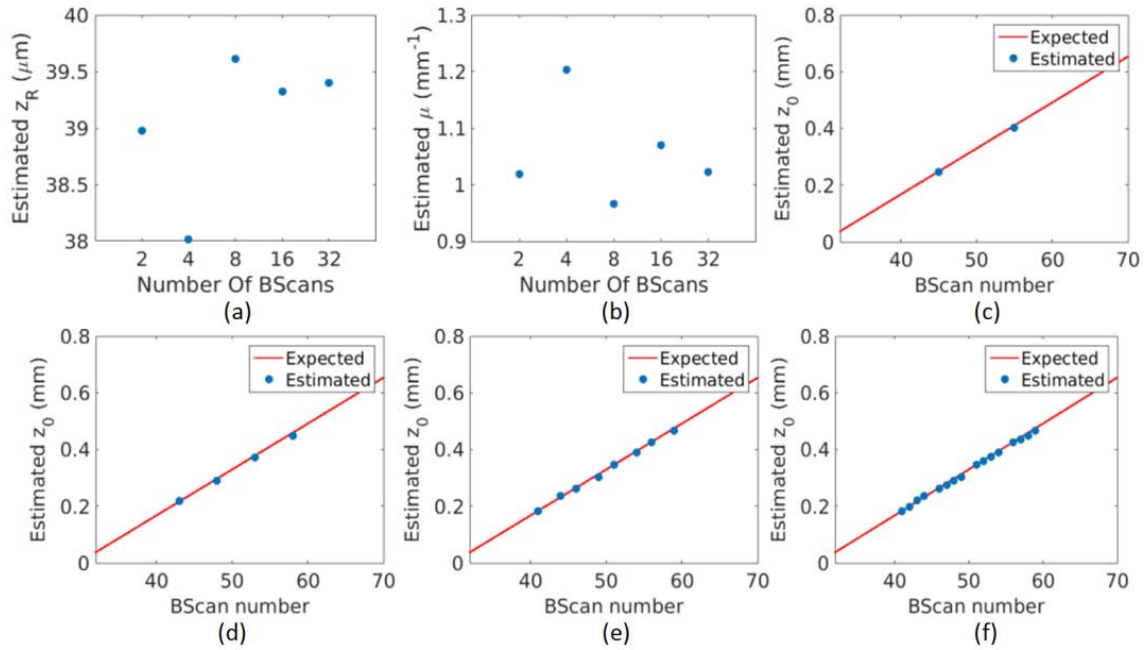


Figure 4.9 Estimated model parameters: (a)  $z_R$  and (b)  $\mu$ , obtained from the averaged A-lines of 2, 4, 8 and 16 B-Scans acquired at different focus positions inside the sample with 0.05 wt. %  $\text{TiO}_2$  in silicone. The estimated and expected  $z_0$  are shown for the combinations of (c) 2, (d) 4, (e) 8, and (f) 16 B-Scans, i.e. focus locations.

## 4.4 Discussion

We presented a method to estimate the sample attenuation coefficients from OCT measurements compensated for the effects of the axial PSF. The recorded signals were modeled by assuming single-scattering in a homogeneous sample accounting for the system's roll-off, noise and focused beam shape (axial PSF). The model parameters of the focused axial PSF were estimated from experimental OCT data. Our goal was to achieve accurate estimation of the attenuation coefficient to enable reliable quantitative analysis of a sample under investigation. The numerical study predicted the performance, and hence the limitations, of our model for different experimental conditions. We observed that for a Rayleigh length smaller than 0.5 mm the estimation error of attenuation coefficient is smaller than 10% for a sample with attenuation coefficient of  $0.73 \text{ mm}^{-1}$  and with the location of the focused beam inside the sample. The signal decay caused by the effect of axial PSF for the location of the focus inside and close to the sample's surface for larger Rayleigh lengths is not as significant as for smaller Rayleigh lengths. Monte Carlo simulation shows that accurate estimation of the Rayleigh length for the location of focus

above the sample is not feasible. However, the estimation errors of attenuation coefficient and the location of focus are smaller than 12% both above and inside the sample.

In experiments with phantoms of different weight concentrations  $\text{TiO}_2$  in silicone, good fits of the model to the measurements using a single B-scan as well as multiple B-scans acquired for different focus positions were obtained. In the latter case the parameters related to sample and optics were shared, whereas the focus position and signal strength were allowed to vary among the different B-scans. Only for focus positions very deep into the sample, the fitted model parameters started to deviate from the measurements closer to the sample's surface. This might be due to the background noise subtraction or an incorrect estimation of roll-off.

The estimated attenuation coefficients using single B-scans are varying among the B-scans and tend to decrease when the focus is shifting to larger depths. We observed that the incorrect estimation of model parameter  $C$  can significantly influence the estimation of the attenuation coefficients. Therefore, finding a method to fix this parameter would significantly improve the results of estimating the attenuation coefficient from a single B-scan.

We also combined multiple B-scans acquired at different focus positions to estimate the model parameters. The estimated Rayleigh length and locations of focus in different B-scans could be estimated with less than 3% error while using 8 B-scans. Using more B-scans does not show a significant improvement in estimating the model parameters. To be able to compare the numerical and experimental results properly, the true attenuation coefficient values of the samples should be known. While these attenuation coefficients are unknown, we do know the concentration of  $\text{TiO}_2$ . We showed that in samples with different concentrations of  $\text{TiO}_2$  dispersed in silicone there is a linear relation between the 0.05 wt. % and 0.1 wt. %  $\text{TiO}_2$  weight concentration and the estimated attenuation coefficients. However, the estimated attenuation coefficient for 0.25 wt. %  $\text{TiO}_2$  is slightly lower than the expected value. It has been shown previously that the measured attenuation coefficient falls below the expected values for increasing particles concentration due to an increase of the amount of multiple

scattering [25]. Applying a multiple-scattering model can result in a better correlation between the measurements and the OCT light model.

A limitation of this work is the assumption of isotropic scattering and weak concentrations of scatterers such that a single-scattering model suffices.

In ophthalmology we encounter a shift of the focal plane due to accommodation of the human eye and movements of the eye and the head. The method can also be applied to data in which the focus position remains fixed for all B-scans. In addition, in ophthalmology, the recorded OCT scans obtained from a clinical OCT system are usually averaged over 10-100 B-scans during acquisition to improve the image quality of the scans. To obtain the precision explained in this research (by averaging over 500 A-lines), we only need to average over a small area in the image (5-50 neighboring A-lines). To obtain a higher spatial resolution, it is advised to reduce the number of averaging among neighboring A-lines while increasing the averaging rate during acquisition. In future work, we will extend the proposed method to estimate the attenuation coefficient values of a multi-layer sample from the OCT images. This is especially relevant in applications such as ophthalmology where each retina layer has different optical properties.

## Acknowledgment

This research was funded by the Netherlands Organization for Health Research and Development (ZonMw) TOP grant (91212061). We would like to acknowledge Dr. Dirk H. J. Poot (Biomedical Imaging Group Rotterdam, departments of Medical Informatics and Radiology, Erasmus Medical Center Rotterdam, Rotterdam, The Netherlands) and Prof. Ton van Leeuwen (Biomedical Engineering and Physics, Amsterdam Medische Centra, Amsterdam, the Netherlands) for their technical support in this work.

## References

- [1] K. A. Vermeer, J. van der Schoot, H. G. Lemij, and J. F. de Boer, "RPE-normalized RNFL attenuation coefficient maps derived from volumetric OCT imaging for glaucoma assessment," *Invest. Ophthalmol. & Vis. Sci.* **53**, 6102-6108 (2012).

- [2] R. A. McLaughlin, L. Scolaro, P. Robbins, C. Saunders, S. L. Jacques, and D. D. Sampson, "Parametric imaging of cancer with optical coherence tomography," *J. Biomed. Opt.* **15**, 046029 (2010).
- [3] K. Barwari, D. M. de Bruin, E. C. Cauberg, D. J. Faber, T. G. van Leeuwen, H. Wijkstra, J. de la Rosette, and M. P. Laguna, "Advanced diagnostics in renal mass using optical coherence tomography: a preliminary report," *J. Endourol.* **25**, 311–3115 (2011).
- [4] K. Barwari, D. M. de Bruin, D. J. Faber, T. G. van Leeuwen, J. J. de la Rosette, and M. P. Laguna, "Differentiation between normal renal tissue and renal tumors using functional optical coherence tomography: a phase I in vivo human study," *BJU International* **110**, E415–E420 (2012).
- [5] P. H. Tomlins, O. Adegun, E. Hagi-Pavli, K. Piper, D. Bader, and F. Fortune, "Scattering attenuation microscopy of oral epithelial dysplasia," *J. Biomed. Opt.* **15**, 066003 (2010).
- [6] Q. Q. Zhang, X. J. Wu, T. Tang, S. W. Zhu, Q. Yao, B. Z. Gao, and X. C. Yuan, "Quantitative analysis of rectal cancer by spectral domain optical coherence tomography," *Phys. Med. Biol.* **57**, 10 (2012).
- [7] F. J. van der Meer, D. J. Faber, D. M. B. Sassoon, M. C. Aalders, G. Pasterkamp, and T. G. van Leeuwen, "Localized measurement of optical attenuation coefficients of atherosclerotic plaque constituents by quantitative optical coherence tomography," *IEEE Trans. Med. Imag.* **24**, 1369–1376 (2005).
- [8] C. Xu, J. M. Schmitt, S. G. Carlier, and R. Virmani, "Characterization of atherosclerosis plaques by measuring both backscattering and attenuation coefficients in optical coherence tomography," *J. Biomed. Opt.* **13**, 034003 (2008).
- [9] G. van Soest, T. Goderie, E. Regar, S. Koljenovic, G. L. J. H. van Leenders, N. Gonzalo, S. van Noorden, T. Oka-mura, B. E. Bouma, G. J. Tearney, J. W. Oosterhuis, P. W. Serruys, and A. F. W. van der Steen, "Atherosclerotic tissue characterization in vivo by optical coherence tomography attenuation imaging," *J. Biomed. Opt.* **15**, 011105 (2010).
- [10] J. M. Schmitt, A. Knüttel, M. Yadlowsky, and M. A. Eckhaus, "Optical-coherence tomography of a dense tissue: statistics of attenuation and backscattering," *Phys. Med. Biol.* **39**, 1705-1720 (1994).
- [11] R. O. Esenaliev, K. V. Larin, I. V. Larina, and M. Motamedi, "Non-invasive monitoring of glucose concentration with optical coherence tomography," *Opt. Lett.* **26**, 992-994 (2001).
- [12] A. I. Kholodnykh, I. Y. Petrova, K. V. Larin, M. Motamedi, R. O. Esenaliev, "Precision of Measurement of Tissue Optical Properties with Optical Coherence Tomography", *Appl. Opt.* **42**, 3027-3037 (2003).
- [13] L. Thrane, H. T. Yura, and P. E. Andersen, "Analysis of optical coherence tomography systems based on the extended Huygens Fresnel principle," *J. Opt. Soc. Am. A* **17**, 484-490 (2000).

- [14] V. D. Nguyen, D. J. Faber, E. van der Pol, T. G. van Leeuwen, and J. Kalkman, "Dependent and multiple scattering in transmission and backscattering optical coherence tomography," *Opt. Exp.* **21**, 29145-29156 (2013).
- [15] K. A. Vermeer, J. Mo, J. J. Weda, H. G. Lemij, and J. F. de Boer, "Depth-resolved model-based reconstruction of attenuation coefficients in optical coherence tomography," *Biomed. Opt. Exp.* **5**, 322-337 (2013).
- [16] B. Ghafaryasl, K. A. Vermeer, J. F. de Boer, M. E. J. van Velthoven, L. J. van Vliet, "Noise-adaptive attenuation coefficient estimation in spectral domain optical coherence tomography data," in *Proceedings of IEEE 13<sup>th</sup> International Symposium on Biomedical Imaging (ISBI)*, 706-709 (2016).
- [17] S. H. Yun, G. J. Tearney, B. E. Bouma, B. H. Park, and J. F. de Boer, "High-speed spectral-domain optical coherence tomography at 1.3  $\mu$  m wavelength," *Opt. Exp.* **11**, 3598-3604 (2003).
- [18] T. G. van Leeuwen, D. J. Faber, and M. C. Aalders, "Measurement of the axial point spread function in scattering media using single-mode fibre-based optical coherence tomography," *IEEE J. Sel. Top. Quant. Electr.* **9**, 227-233 (2003).
- [19] B. Ghafaryasl, K. A. Vermeer, J. Kalkman, T. Callewaert, J. F. de Boer, and L. J. van Vliet, "Accurate estimation of the attenuation coefficient from axial point spread function corrected OCT scans of a single layer phantom," *Proc. SPIE 10483*, 104832B (2018).
- [20] G. T. Smith, N. Dwork, D. O'Connor, U. Sikora, K. L. Lurie, J. M. Pauly, and A. K. Ellerbee, "Automated, depth-resolved estimation of the attenuation coefficient from optical coherence tomography data," *IEEE Trans. Med. Imaging* **34**, 2592-2602 (2015).
- [21] S. Stefan, K. S. Jeong, C. Polucha, N. Tapinos, S. A. Toms, and J. Lee, "Determination of confocal profile and curved focal plane for OCT mapping of the attenuation coefficient," *Biomed. Opt. Express* **9**, 5084-5099 (2018).
- [22] D. J. Faber, F. J. van der Meer, M. C. G. Aalders, and T. G. van Leeuwen, "Quantitative measurement of attenuation coefficients of weakly scattering media using optical coherence tomography," *Opt. Express* **12**, 4353-4365 (2004).
- [23] M. W. A. Caan, H. G. Khedoe, D. H. J. Poot, A. J. den Dekker, S. D. Olabarriaga, K. A. Grimbergen, L. J. van Vliet, and F. M. Vos, "Estimation of diffusion properties in crossing fibre bundles," *IEEE Trans. Med. Imag.* **29**, 1504-1515 (2010).
- [24] T. Callewaert, J. Dik, and J. Kalkman, "Segmentation of thin corrugated layers in high-resolution OCT images," *Opt. Express* **25**, 32816-28 (2017).
- [25] J. Kalkman, A. V. Bykov, D. J. Faber, and T. G. van Leeuwen, "Multiple and dependent scattering effects in Doppler optical coherence tomography," *Opt. Express* **18**, 3883-3892 (2010).



# 5 Attenuation coefficient estimation in Fourier-domain OCT of multi-layered phantoms

---

In this chapter, we present an extension of the method presented in the previous section. This is done by fitting a single scattering model for the OCT signal in a multi-layer sample to the recorded OCT signal corrected for the noise floor and the effect of finite detector resolution called roll-off. In addition, we employ numerical simulations to obtain the theoretically achievable precision and accuracy of the estimated parameters under various experimental conditions. Finally, the method is applied to two sets of measurements obtained from a multi-layer phantom by two experimental OCT systems: one with a large (288  $\mu\text{m}$ ) and one with a small (36  $\mu\text{m}$ ) estimated Rayleigh length (in air). The multi-layer phantom is composed of layers with a distinctive concentration of  $\text{TiO}_2$  dispersed in silicone to assess the performance of the method. Numerical results show that the accuracy and precision of the estimated attenuation coefficients remain below 10%, specifically for focus positions within  $\pm 3$  mm of the sample's surface using the large Rayleigh length system and for focus positions inside the sample using the small Rayleigh length system. Experimental results show a linear relation of the estimated attenuation coefficients of each layer with the dissolved particle concentration ( $R^2 > 0.94$  and  $p < 0.02$ ) for a single-focus (averaged) scan obtained by both small and large Rayleigh lengths systems. In addition, using averaged scans acquired at multiple focus locations inside the sample, the linear correlation was improved to  $R^2 > 0.98$  ( $p < 0.008$ ) for both sets of measurements.

B. Ghafaryasl, k. A. Vermeer, J. Kalkman, T. Callewaert, J. F. de Boer, L. J. van Vliet, Attenuation coefficient estimation in Fourier-domain OCT of multi-layered phantoms, *Biomed. Opt. Express*, **12**, 2744-2758 (2021).

## 5.1 Introduction

Optical coherence tomography (OCT) is an interferometric imaging technique that can generate high-resolution three-dimensional images of biological tissues. Many tissues, such as the retina or the blood vessel wall are composed of a number of distinct tissues, each having its own optical tissue properties. OCT has been widely used to capture structural information of tissues for clinical tasks such as the diagnosis of retinal and vascular diseases. Recently, there has been a growing interest in the field of ophthalmology for utilizing optical tissue properties, such as the attenuation coefficient, for diagnosis and disease progression. The attenuation coefficient can be estimated from the intensity or amplitude of the OCT signal and can be used as a biomarker for the diagnosis and monitoring of diseases [1-6] as well as for tissue characterization [7-9]. Several methods based on single [10-12] and multiple [13,14] scattering of light have been presented for estimating the attenuation coefficient in a homogeneous medium using OCT. Only a few methods have been developed to estimate the attenuation coefficient of the tissue while taking into account the effect of the beam shape on the acquired OCT signal. Smith et al. [15] compensated for the effect of beam shape by correcting the OCT scan for the confocal detection efficiency using an existing model [8]. However, in their work the parameters of the shape of the beam need to be known before the estimation of the attenuation coefficient. In many medical applications, such as ophthalmology, the location of the focus varies between B-scans and there is a need for a method to automatically estimate the focus location to compensate for the effect of the beam shape in the estimation of the attenuation coefficient. Stefan et al. [16] introduced a method to estimate the attenuation coefficient using two B-scans with different focus locations to first estimate the location of focus and subsequently estimate the attenuation coefficient from a single scattering model of the OCT light after compensating for the effect of beam shape. However, this method is dependent on having identical lateral beam locations of the sample to unambiguously determine the effect of the beam. In addition, this method was only tested with static samples where an identical physical location in both B-scans is well feasible and factors such as the beam angle of incidence can be controlled to ensure a similar intensity of the measured OCT signal. The limitation of having access to two scans from exactly the same position in the tissue is a problem in

many clinical data, such as retinal scans, where only one averaged measurement of the same tissue's location is available. Recently, we presented a method to achieve an accurate estimate of attenuation coefficient for semi-infinite samples by compensating for the effects of the beam shape [17]. The proposed method estimates the axial point spread function (PSF) model parameters (Rayleigh length and focus depth) and attenuation coefficient by fitting a single-scattering model to the measured OCT signal of a homogenous sample. Monte Carlo simulations quantified the maximum expected accuracy and precision of our proposed method. However, while the method could estimate the attenuation coefficients of the materials from measurements of uniform samples, most biological tissues such as the retina are layered, and hence, the method cannot be applied straightforwardly. Therefore, there is a need, e.g. in ophthalmology, for a method to reliably estimate the attenuation coefficient properties in multi-layer samples.

In this chapter, we demonstrate simultaneous attenuation coefficient and beam focus position estimation in multi-layer samples. We investigate whether using multiple B-scans, acquired with different focus positions, improves the estimation of the attenuation coefficient. In addition, simulations of the OCT signal with speckles were used to numerically evaluate the accuracy and precision of the estimated parameters by the proposed method. The numerical analysis is needed for the evaluation of the proposed method since the true attenuation coefficient values of the materials are not known in real experiments. Finally, actual measurements of multi-layer phantoms composed of layers with different concentrations of  $\text{TiO}_2$  dispersed in silicone is used to investigate the accuracy of our method. For this, the method is applied to B-scans of this phantom obtained with two different experimental OCT systems: one with a small and one with a large Rayleigh length.

## 5.2 Method and experiments

In this section, the OCT signals for multi-layer samples including the effect of the axial point spread function is described. In addition, we introduce a method for accurate estimation of the attenuation coefficient and focus position in a multi-layer sample after compensating the recorded signal for the average noise level and roll-off. We simulate a realistic OCT signal including speckle formation and intensity noise. A Monte Carlo simulation is used to investigate the accuracy and

precision of the AC estimation method. Finally, we present the experimental results on a multi-layer phantom to assess the performance of the proposed methods in practice.

### 5.2.1 Estimating the model parameters

We simultaneously estimate the model parameters of the axial PSF and the attenuation coefficient per layer using a maximum likelihood estimator. For an inhomogeneous sample, a single-scattering physical model of averaged intensity of the OCT light at sampled physical depth  $z$  can be expressed as,

$$I(z) = R(z) \cdot \left( L \mu_{b,NA}(z) e^{-2 \int_0^z \mu_t(z') dz'} \cdot \frac{1}{\left( \frac{z - z_0}{2z_R(z)} \right)^2 + 1} + D(z) + \varepsilon(z) \right) \quad (5.1)$$

where  $R(z)$  is the signal intensity decay caused by roll-off as the ratio of spectral resolution over pixel resolution [18]. In the first term the signal variation is caused by three factors (from left to right): a scaling factor  $L$ , which comprises several factors such as input power, detector efficiency, coherence length and integrated phase function; the signal decay caused by a depth-resolved exponential signal attenuation modelled by  $\mu_t(z)$  (the total attenuation coefficient), which is the sum of  $\mu_a(z)$  (absorption coefficient) and  $\mu_s(z)$  (the scattering coefficient). The backscattering coefficient is  $\mu_{b,NA}(z) = \mu_s(z) \cdot p_{NA}(z)$ , with  $p_{NA}(z)$  being the fraction of scattered photons detected by OCT system [11, 19]. Finally, the axial PSF is modelled by a Lorentzian function at focus position  $z_0$  and scaled by the Rayleigh length in the medium,  $z_R(z)$  [20]. The second term  $D(z)$  is the noise level offset. The intensity of the OCT signal inside a (homogenous) layer is distorted by speckle noise and has an exponential distribution [18]. However, based on the central limit theorem, the uncorrelated intensity noise in the average of a large enough number ( $M$ ) of neighbouring A-lines ( $M > 30$  based on rule of thumb) converges to a normal distribution  $\mathcal{N}[m(z), M]$ , with  $m(z)$  being the expected value of the exponential distribution, and  $m(z)^2/M$  the variance of the resulting normal distribution. For an averaged A-line, the third term  $\varepsilon(z)$  is a Gaussian noise which represents the effect of additive background noise and

speckles with normal distributions. The acquired OCT signal can be corrected for the effect of noise floor [15] and roll-off [15,16].

To reduce the complexity of the fit model, we considered the parameters  $\mu_t = \mu_s$  and call it  $\mu$ , by assuming  $\mu_a \ll \mu_s$ , which is a good approximation for the wavelengths typically used for ophthalmic OCT. In addition, we assumed  $p_{NA}(z)$  and refractive indices to be constant for all depths. A constant refractive index results in a constant Rayleigh length for all depths. With the aforementioned assumptions, a model of OCT signal with  $N_D$  data-points  $z_j$  on each A-line can be expressed as,

$$I(z_j) = R(z_j) \cdot \left( C \mu(z_j) e^{-2\Delta \sum_{i=1}^j \mu(z_j)} \cdot \frac{1}{\left( \frac{z_j - z_0}{2z_R} \right)^2 + 1} + D(z_j) + \varepsilon(z_j) \right) \quad (5.2)$$

where the parameter  $\Delta$  indicates the depth per pixel corresponding to the sampling  $z_j$  and  $C=L \cdot p_{NA}$  is a scaling factor. To estimate the model parameters, we use multiple averaged A-lines with different locations of focus,  $z_{0_i}$ . Therefore, for a set of  $N_A$  averaged A-lines  $I_1(z_j), I_2(z_j), \dots, I_{N_A}(z_j)$ , the unknown parameters  $C_i$  and  $z_{0_i}$ , and the attenuation coefficient at each depth, can be estimated by minimizing the log-weighted sum of squared residuals,  $\chi$ , given by,

$$\chi = \sum_{i=1}^{N_A} \sum_{j=1}^{N_D} \left( \ln(I_i(z_j)) - \ln \left( \frac{C_i \mu(z_j) e^{-2\Delta \sum_{i=1}^j \mu(z_j)}}{\left( \frac{z_j - z_{0_i}}{2z_R} \right)^2 + 1} \right) \right)^2 \quad (5.3)$$

where the parameters can be considered to be common (joint), fixed (known) or independent among the averaged A-lines. The subscript  $j$  is an index that denotes the data-point number on each A-line. The proposed method requires knowledge

of the thickness of each layer per A-line and therefore segmentation of the multi-layer sample is a prerequisite.

### 5.2.2 Simulation of OCT signal and Monte Carlo simulation

To study the performance of the proposed method numerically, we applied it to simulated OCT signals. For this, we integrated the effect of axial PSF to an existing single-scattering based simulation of the OCT signals, which are distorted by speckle and signal intensity noise of a multi-layer sample [21].

OCT signals were simulated for a system with a Gaussian-shaped spectrum with a center wavelength of 1000 nm and a full width at half maximum of 73 nm. The front surface is located at 0.2 mm from the zero-delay. The simulated sample has four homogeneous layers each having thickness ( $d$ ) and attenuation coefficients ( $\mu$ ) of:  $d_1 = 170 \mu\text{m}$ ,  $d_2 = d_3 = d_4 = 100 \mu\text{m}$  and  $\mu_1 = 4.4 \text{ mm}^{-1}$ ,  $\mu_2 = \mu_1/2.5 = 1.76 \text{ mm}^{-1}$ ,  $\mu_3 = \mu_1/5 = 0.88 \text{ mm}^{-1}$  and  $\mu_4 = \mu_1/2.5 = 1.76 \text{ mm}^{-1}$ , respectively. To simulate these attenuation coefficient values, the fraction of the scattered intensity was assumed to be 0.5 and the averaged particle size was set to 700 nm. The concentration of particles in each layer was  $P_1 = 7\%$ ,  $P_2 = 2.8\%$ ,  $P_3 = 1.4\%$ ,  $P_4 = 2.8\%$ . The model is based on the single scattering approximation. In addition, to calculate the scattering properties of the particles using Mie-scattering, the refractive indices of the sample and particles were set to  $n_{med} = 1.44$  and  $n_{part} = 1.48$ . The Rayleigh length of the axial PSF's model was set to either  $z_R = 432 \mu\text{m}$  or  $z_R = 57.6 \mu\text{m}$  in the medium, and the location of the focus varied between  $\pm 1$  mm from the surface of the sample with a step size of  $20 \mu\text{m}$ . 500 averaged A-lines, with 1024 data-points per A-line, distorted by additive Gaussian noise with a standard deviation of 5% of the signal intensity were simulated. All the simulations were implemented in Matlab 2017b on a Dell Latitude with a dual core CPU (2.60 GHz) and 8 GB of RAM.

For each Rayleigh length, the method in section 2.1 was applied to estimate the model parameters  $C$ ,  $z_0$  and  $\mu_n$  ( $n = 1,2,3,4$ ), while fixing the  $z_R$  values to the known Rayleigh lengths, using the interior-point technique of Matlab (Curve Fitting Toolbox, Matlab 2017b; The MathWorks, Natick, MA) with a termination tolerance set to  $10^{-15}$ , and the maximum number of iteration and function evaluations set to  $10^6$ . The initial values for the unknown parameters were set to  $C$

$= 5.10^4$ ,  $z_0 = 0.6$  mm and  $\mu_1 = 3$  mm<sup>-1</sup>,  $\mu_2 = 3$  mm<sup>-1</sup>,  $\mu_3 = 2$  mm<sup>-1</sup> and  $\mu_4 = 1$  mm<sup>-1</sup>. In the process of fitting the model of Eq. 5.2 for homogeneous layers, a lower and upper bound was set for all parameters, i.e.  $0$  mm<sup>-1</sup>  $< \mu < 6$  mm<sup>-1</sup> for all layers,  $0 < C < 10^{10}$  (arbitrary units),  $0$  mm  $< z_0 < 1$  mm for focus inside and  $-1$  mm  $< z_0 < 0$  mm for focus above the sample.

To evaluate the accuracy, precision and feasibility of the proposed method numerically, the coefficient of variations (CoV) of the estimated parameters and the bias were calculated for the two selected Rayleigh lengths and different locations of focus around the surface of the sample.

### 5.2.3 Phantom experiments

To investigate the practical feasibility of the proposed method, we applied it to measurements obtained from a multi-layer phantom by two experimental OCT system with different Rayleigh lengths. The model parameters were estimated based on either a single or multiple B-scans. The sample consists of four layers with 0.25 wt%, 0.1 wt%, 0.05 wt% and 0.01 wt% of TiO<sub>2</sub> in silicone. The B-scans of the phantom were recorded for various locations of the focal plane from the sample's surface using two experimental systems. The first one is a Ganymede-II-HR Thorlabs spectral domain OCT system (SD-OCT) (GAN905HV2-BU) with an estimated Rayleigh length of 36  $\mu$ m in air. The Rayleigh length of the system was estimated by fitting the axial PSF to a set of measurements obtained by changing the focus location from a sample's surface [19]. The system has a center wavelength of 900 nm and a bandwidth of 195 nm and a scan lens with 18 mm focal length (LSM02-BB). The axial and lateral physical pixel size in air was  $1.27 \times 2.9$   $\mu$ m<sup>2</sup> with 1024 pixels per A-line. The second system is a swept-source OCT (SS-OCT) system [23] with an estimated Rayleigh length of 288  $\mu$ m in air. The system has a center wavelength of 1  $\mu$ m. The axial and lateral pixel size in air was  $3.3 \times 1.45$   $\mu$ m<sup>2</sup> with 1024 pixels per A-line. The refractive index of silicone was considered to be 1.44 [11] and assumed to be constant among the layers.

First, the focus position was set inside the sample, but close to sample's surface by probing the highest intensity in the area of interest during the acquisition. Next, 70 B-scans were obtained with various locations of the focal plane by changing the location of the lens in the sample arm with a physical step size of 20  $\mu$ m and 15  $\mu$ m

for the systems with large and small Rayleigh length, respectively. Then, the B-scans with the location of focus within a range of  $\pm 0.5$  mm around the initial focus location were selected.

Several post-processing steps were performed on the measured A-lines. The averaged noise level was obtained by averaging over a large number of A-lines without any sample in the sample arm, and subtracted from all A-lines. In addition, the signal was corrected for the measured roll-off values of 0.81 and 1.7 for the two systems with large and small Rayleigh length, respectively [17]. Next, the surfaces of the samples were segmented in each B-scan using a minimum cost path search applied to individual B-scans [24]; the locations of the other interfaces were derived from the known thicknesses of the layers. Finally, the averaged A-lines were created by averaging over the central 200 A-lines in each B-scan.

#### *Estimating the model parameters in a single B-Scan*

The method in section 2.1 was applied to estimate the model parameters as explained in section 2.2. The model was fit to the averaged A-lines from each B-scan, with different locations of focus, where the model parameters  $\mu_n$  ( $n = 1, 2, 3, 4$ ),  $C$ , and  $z_0$  were unknown and Rayleigh lengths were set to the values of the experimental system. The initial values were set to  $\mu_1 = 3.5 \text{ mm}^{-1}$ ,  $\mu_2 = 3 \text{ mm}^{-1}$ ,  $\mu_3 = 2 \text{ mm}^{-1}$ ,  $\mu_4 = 3 \text{ mm}^{-1}$ ,  $z_0 = 0.6 \text{ mm}$  for both set of measurements, and  $C = 10^3$  (arbitrary units) for the set of measurements with large and  $C = 10^7$  for the set of measurements with small Rayleigh lengths. We introduced an upper and lower bound for each model parameters to restrict the optimizer to a reasonable domain. The intervals were set to  $0 \text{ mm}^{-1} < \mu < 7 \text{ mm}^{-1}$ ; and  $0 \leq z_0 < 1 \text{ mm}$  for the location of focus inside and  $-1 \text{ mm} < z_0 < 0$  above the sample for both sets of measurements, and  $0 < C < 10^4$  for the set of measurements with large and  $0 < C < 10^{10}$  for the set with small Rayleigh lengths. Since the real values of the attenuation coefficients of the sample's layers are unknown, the correlation between the estimated attenuation coefficients and the concentrations of  $\text{TiO}_2$  in silicone was investigated for each set of measurements.

### *Estimating the model parameters using multiple B-Scan*

Multiple B-scans with different locations of focus were used to estimate the model parameters. The free running parameters  $\mu_1$  through  $\mu_4$  were considered to be common for all B-scans, while  $z_{o_i}$  and  $C_i$  in Eq. 5.3 were estimated for each B-scan individually. The Rayleigh length  $z_R$  was fixed to the known values of the experimental setups. We used the same initialization values and boundary conditions for the optimization process as reported earlier for the single B-scan experiments. In addition, different combinations of the averaged A-lines were used to investigate the possibility to improve the results.

Previously, we showed that in samples with different concentrations of  $\text{TiO}_2$  dispersed in silicone there is a linear relation between the  $\text{TiO}_2$  weight concentration and the estimated attenuation coefficients [17]. The linear relation was calculated by fitting a line to the estimated attenuation coefficients in the averaged A-lines using Matlab's *linear regression* (Statistics Toolbox, MATLAB 2017; The MathWorks, Natick, MA).

## **5.3 Results**

### *Simulation results*

The proposed method in section 2.1 was tested with the simulation of the OCT signal as described in section 2.2. The OCT images of a multi-layer sample and the averaged central 200 central A-lines are shown in Fig. 5.1 for  $z_R = 40 \mu\text{m}$  and  $z_R = 300 \mu\text{m}$  in air and an initial location of focus  $z_0 = 0.1 \text{ mm}$  inside the sample. The proposed method was applied to 200 averaged simulated A-lines and the unknown model parameters  $C$ ,  $z_0$ , and  $\mu_n$  ( $n = 1, 2, 3, 4$ ) were estimated for different locations of the focus and the two selected Rayleigh lengths.

As can be observed in Fig. 5.2(a), the focus is estimated accurately for the small Rayleigh length when it is located inside the sample. However, Fig. 5.2(b) shows for the large Rayleigh length, the estimation of the focus location was inaccurate because the effect of the focus on the intensity along an A-line cannot be distinguished from the signal decay caused by light attenuation. The CoV of the estimated attenuation coefficients of four layers and the corresponding estimation

bias are shown in Fig. 5.2(c-f) as a function of focus location for the two selected Rayleigh lengths. As can be seen, the CoV for both systems remains below 10% when focussing inside the sample. For  $z_R = 40 \mu\text{m}$  (small Rayleigh length), the bias of the estimated attenuation coefficients remains below 10% when the focus location is less than 0.5 mm inside the sample. For  $z_R = 300 \mu\text{m}$  (large Rayleigh length), the bias of the estimated attenuation coefficient is above 10% for  $\mu_1$  and  $\mu_2$  and below 10% for  $\mu_3$  and  $\mu_4$  if the location of the focus lies inside the sample. This bias is the result of the incorrect estimation of the focus.

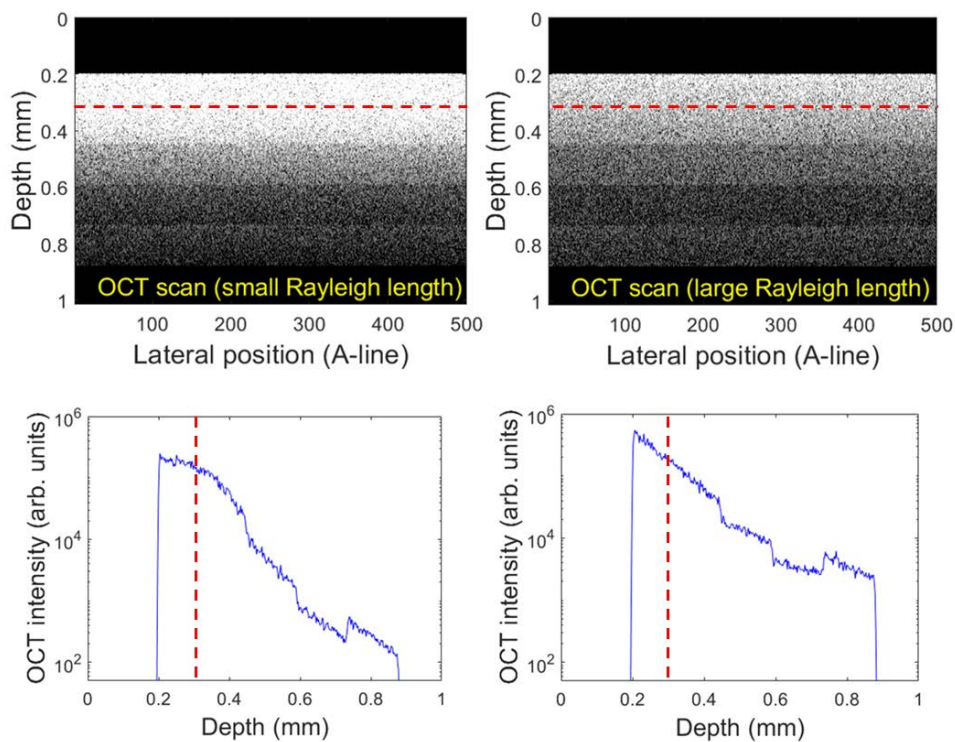


Figure 5.1 Top row) Two simulated OCT B-scans of a multi-layer sample with focus location at 0.1 mm inside the sample, shown by red dashed lines, for an OCT system with  $40 \mu\text{m}$  (left) and  $300 \mu\text{m}$  Rayleigh lengths; Bottom row) The averaged results of 200 central A-lines for the small (left) and the large (right) Rayleigh length systems.

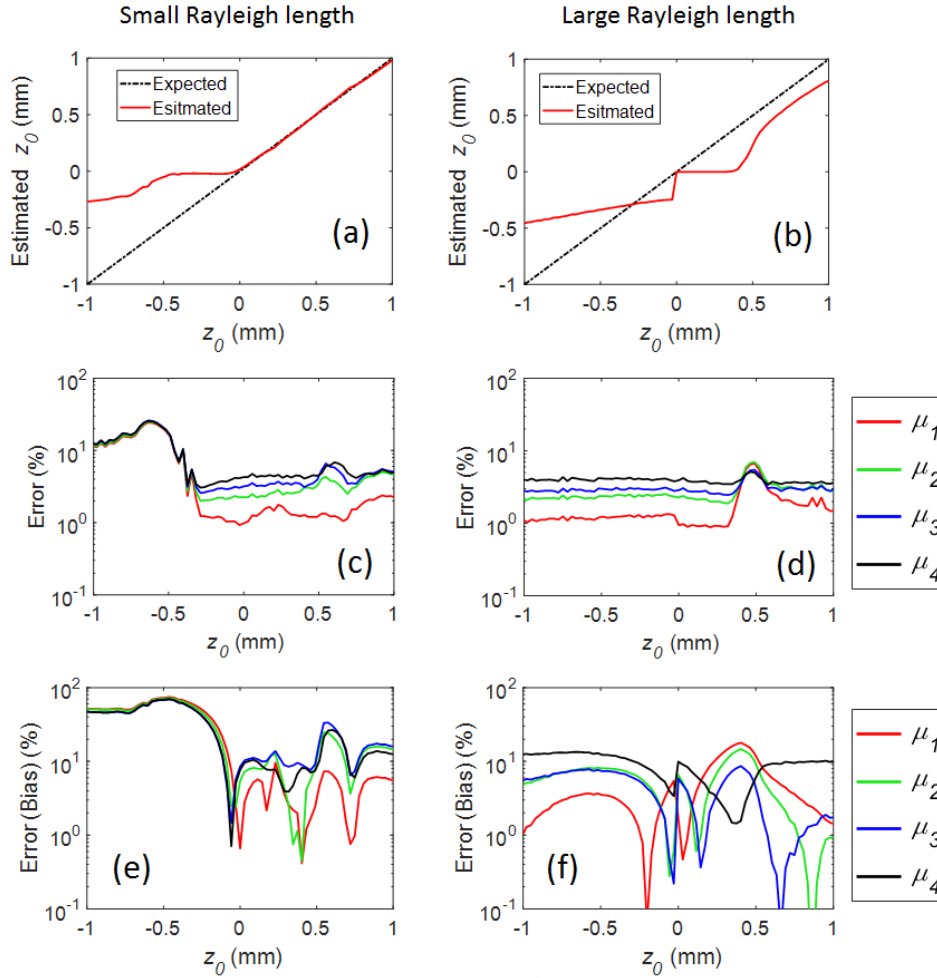


Figure 5.2 The results of fitting the model to the simulated OCT signals with a small (left column) and a large (right column) Rayleigh length. For both sets of data, the estimated focus position  $z_0$  (a,b), the error (CoV) of the estimated attenuation coefficients (c,d), and the bias of the attenuation coefficients (e,f), for all four layers are shown as a function of the imposed focus position.

The effect of the beam shape on the acquired OCT signal and therefore on the estimation of the attenuation coefficients is more significant for the smaller Rayleigh length. Therefore, for small Rayleigh lengths, an inaccurate estimation of the location of focus results in a less accurate estimation of the attenuation coefficients. This effect is shown in Fig. 5.2(a-d) where erroneous estimations of focus locations increase the CoVs for the smaller Rayleigh length, while there is no significant change of the CoVs for the larger Rayleigh length.

The linear relation between the estimated attenuation coefficients and the particle concentration of the respective layer as a function of focus location is

shown in Fig. 5.3 for both the small and the large Rayleigh length. This figure shows  $R^2$ -values indicating the goodness of the linear fit and the corresponding p-values. The  $R^2$ -values larger than 0.95 and 0.98 for small and large Rayleigh lengths, respectively, show a good correlation between the estimated attenuation coefficients with  $p < 0.01$  and the  $\text{TiO}_2$  concentrations for all focus positions.

In addition, Fig. 5.4 shows this linear relation between the estimated attenuation coefficients and the particle concentration of the respective layer in the averaged A-lines acquired with the focus set to 0.1 mm inside the sample as a function of the system's Rayleigh length from 0.005 mm to 1 mm. This figure shows  $R^2$ -values indicating the goodness of the linear fit and the corresponding p-values. The  $R^2$ -values larger than 0.92 show a good correlation between the estimated attenuation coefficients with  $p < 0.02$  and the  $\text{TiO}_2$  concentrations for all focus positions.

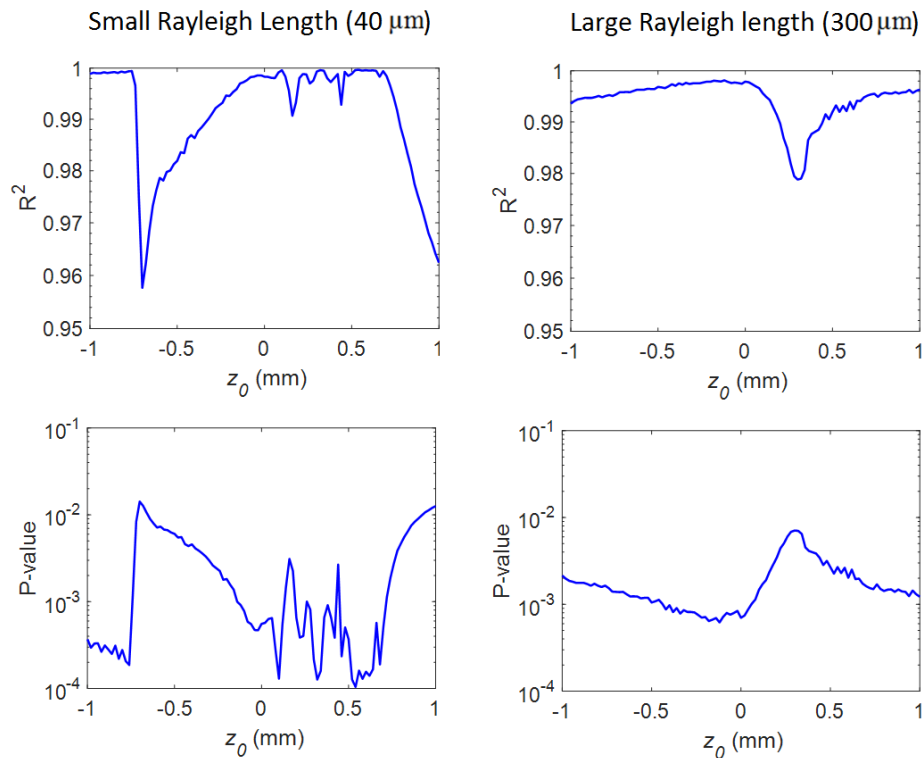


Figure 5.3 The linear relation between the estimated attenuation coefficients and the particle concentration of the respective layer; where  $R^2$  (top row) and p-values (bottom row) of the linear fit are shown as a function of focus position for a small (left column) and a large (right column) Rayleigh length.

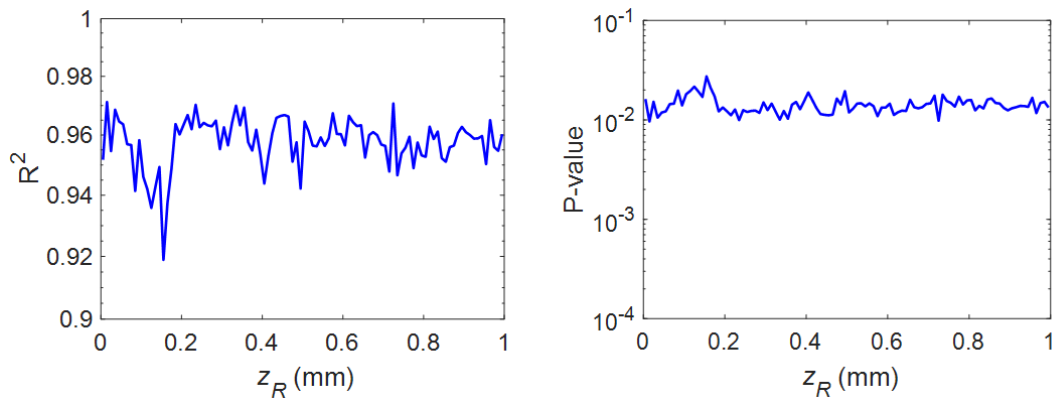


Figure 5.4 The linear relation between the estimated attenuation coefficients and the particle concentration of the respective layer; where  $R^2$  (left) and p-values (right) of the linear fit are shown as a function of Rayleigh length with focus set to 100  $\mu\text{m}$  inside the sample.

### *Experimental results*

As mentioned in the previous section, the experimental data of the multi-layer phantom were acquired with two experimental OCT systems with different Rayleigh lengths. Fig. 5.5 shows two typical examples of recorded B-scans obtained by the systems with the focus set to 100  $\mu\text{m}$  inside the sample. The result of fitting the model to the averaged OCT signals (over 200 central A-lines) for the two systems and a series of focus positions, both above and inside the sample, are shown in Fig. 5.6 and Fig. 5.7. As can be seen visually, an acceptable fit to the measurements was obtained when the focus location is within 0.25 mm of the pha-

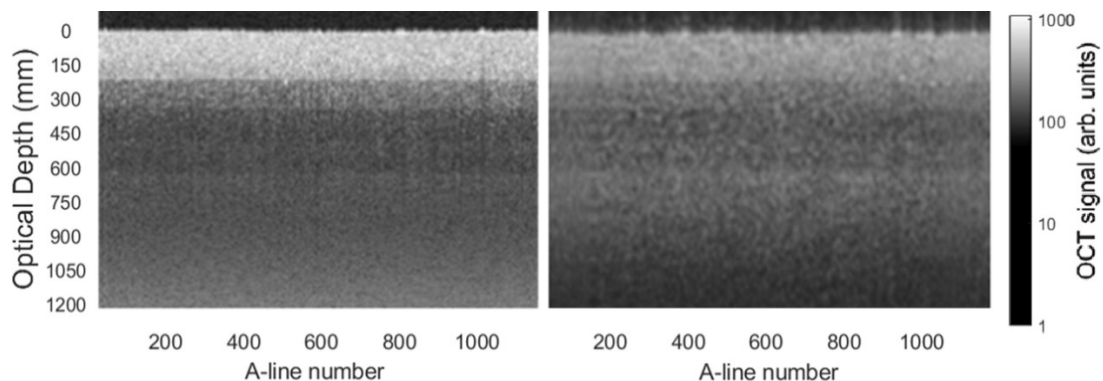


Figure 5.5 OCT B-scans of the multi-layer phantom obtained by a system with a small (left) and a large (right) Rayleigh length where the focus was set to 200  $\mu\text{m}$  inside the sample. The vertical axis indicates the optical distance from the surface of the sample.

-ntom's surface, in the set of measurement with small Rayleigh lengths and for all positions of focus for measurements with large Rayleigh lengths.

The estimated parameters for each averaged A-line are shown in Fig. 5.8 for both sets of measurement. We expect to have similar attenuation coefficient values for each layer of the sample irrespective of the focus position. However, it can be seen in Fig. 5.8 (top row) that the estimated attenuation coefficients vary significantly for different focus positions.

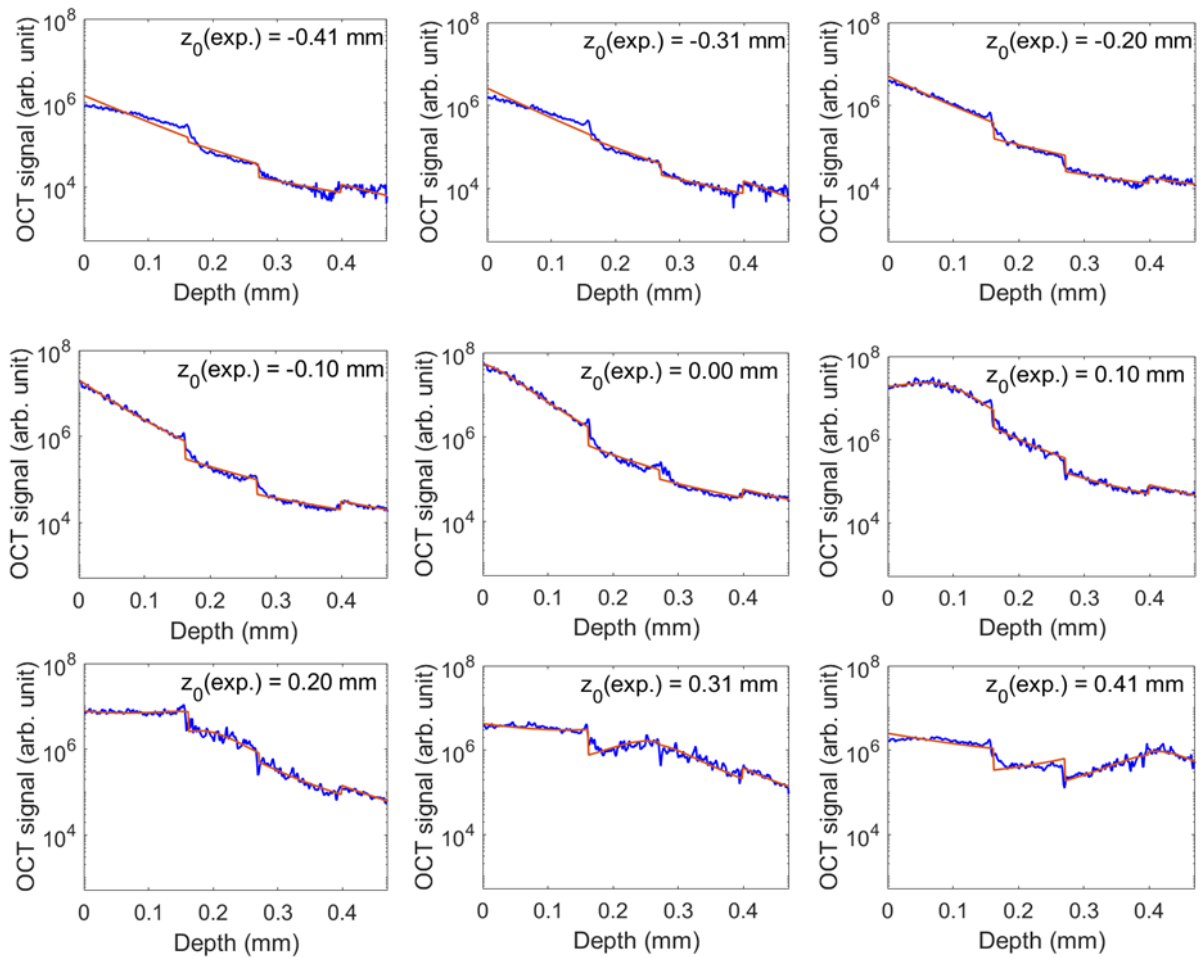


Figure 5.6 The results of fitting the model (red) to the average of the central 200 A-lines per B-scan (blue) obtained from the multi-layer phantom using the OCT system with the small Rayleigh length for a series of focus positions (as indicated in the plots).

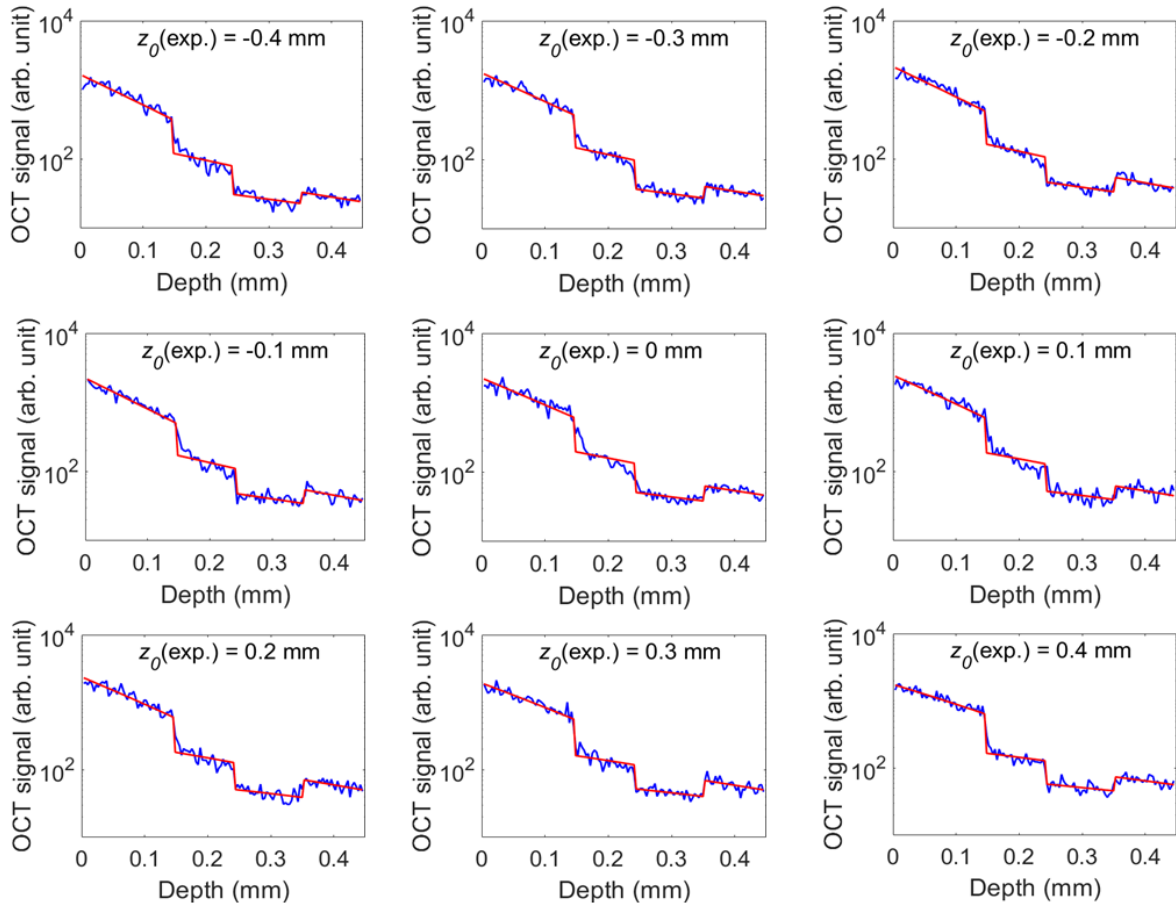


Figure 5.7 The results of fitting the model (red) to the averaged intensity of the OCT signal of the central 200 A-lines per B-scan (blue) obtained from the multi-layer phantom using the OCT system with the large Rayleigh length for a series of focus positions (as indicated in the plots).

The estimated focus positions are shown in Fig. 5.8 (middle row). For small Rayleigh length, there is a good correlation between the estimated and expected focus position. However, the focus position could not be estimated reliably in the data set obtained with the large Rayleigh length.

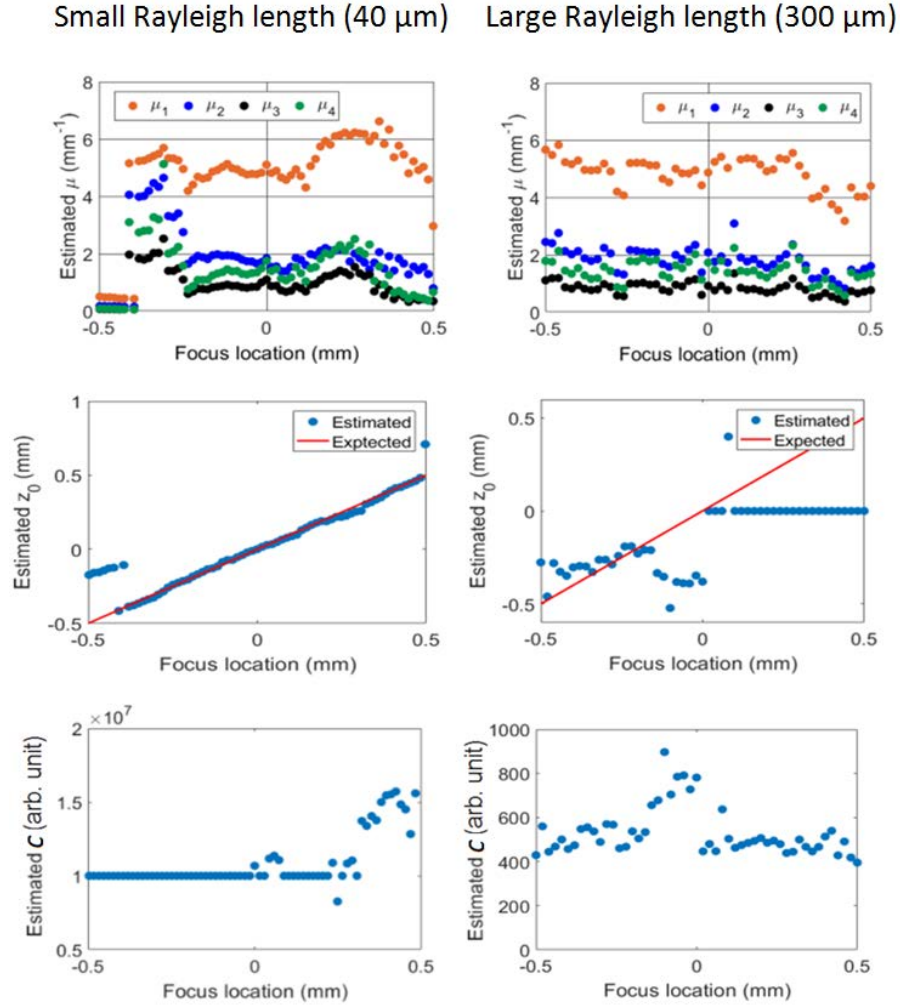


Figure 5.8 The estimated model parameters:  $\mu_i$  (top row),  $z_0$  (middle row) and  $C$  (bottom row) obtained by fitting the model to the averaged A-lines as a function of the imposed focus position for measurements obtained by an OCT system with a small (left column) and a large (right column) Rayleigh lengths.

In addition, we expected to observe a linear relation between the estimated attenuation coefficients and the particle concentration of the respective layer. Fig. 5.9 (top) shows this linear relation to the estimated attenuation coefficients in the averaged A-lines acquired with the focus set to 0.6 mm inside the sample for both set of measurements. Fig. 5.9 (middle) shows  $R^2$ -values indicating the goodness of the linear fit for all the averaged A-lines and Fig. 5.9 (bottom) shows the corresponding p-values. The  $R^2$ -values larger than 0.94 show a good correlation between the estimated attenuation coefficients with  $p < 0.02$  and the  $\text{TiO}_2$  concentrations for all focus positions, except for focus positions higher than 0.3

mm above the sample, in the measurements obtained with the small Rayleigh length.

In the next step, we investigated if using multiple averaged A-lines with different focus locations improves the estimation of the attenuation coefficients. For this, we considered the averaged A-lines recorded with a different number of focus positions, i.e. (2, 4, 8 and 16). The attenuation coefficients of the identical layers among the averaged A-lines were considered to be common in the estimation process. The selected focus positions at different depths and their estimated values are shown in Fig. 5.10 and Fig. 5.11 for the measurement obtained using the OCT system with the small or the large Rayleigh length, respectively. The imposed (expected) and estimated focus position correlate well in measurements obtained using the OCT system with the small Rayleigh length. However, as was expected, an inaccurate estimation of  $z_0$  was obtained in measurements obtained using the OCT system with the large Rayleigh length. The estimated attenuation coefficients for both set of measurements (with small and large Rayleigh lengths) are shown in Tables 5.1 and 5.2. In addition, the  $R^2$ -values of the linear fits to the estimated attenuation coefficients as a function of the particle concentration are also shown in these tables. For the measurements obtained with the small Rayleigh length, the  $R^2$ -values of the fits were higher than 0.99 ( $p = 0.003$ ) using 8 B-scans, which is slightly better than the results obtained using a single B-scan. For the measurements obtained with large Rayleigh length, the  $R^2$ -values of the fits is the highest 0.99 ( $p$ -value  $< 0.006$ ) when using 8 B-scans.

Small Rayleigh length (40  $\mu\text{m}$ )      Large Rayleigh length (300  $\mu\text{m}$ )

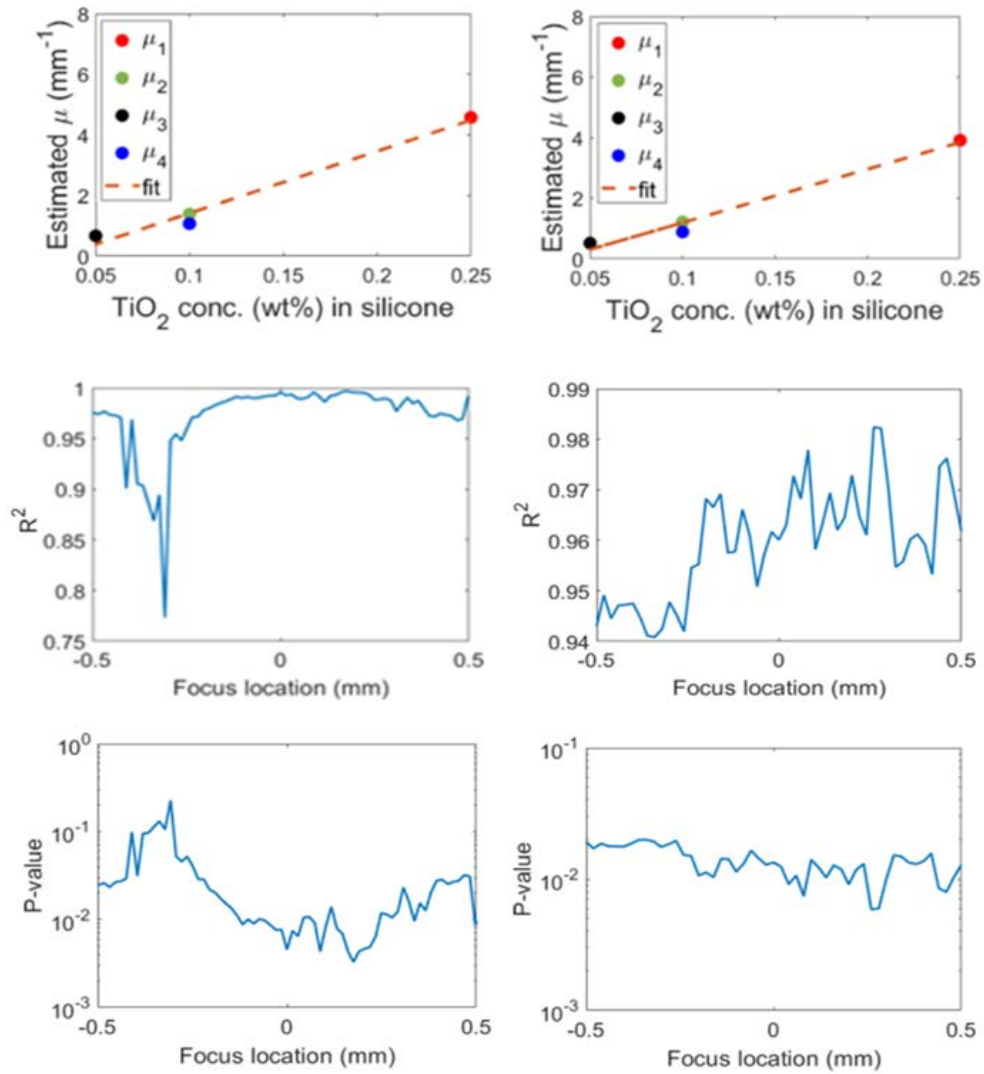


Figure 5.9 Linear fit to the estimated attenuation coefficients as a function of particle concentration (top row) as well as the resulting  $R^2$  (middle row) and p-values (bottom row) of the fit as a function of focus position for an averaged A-line with focus set to 60  $\mu\text{m}$  inside the phantom for measurements using an OCT system with a small (left column) and a large (right column) Rayleigh length systems.

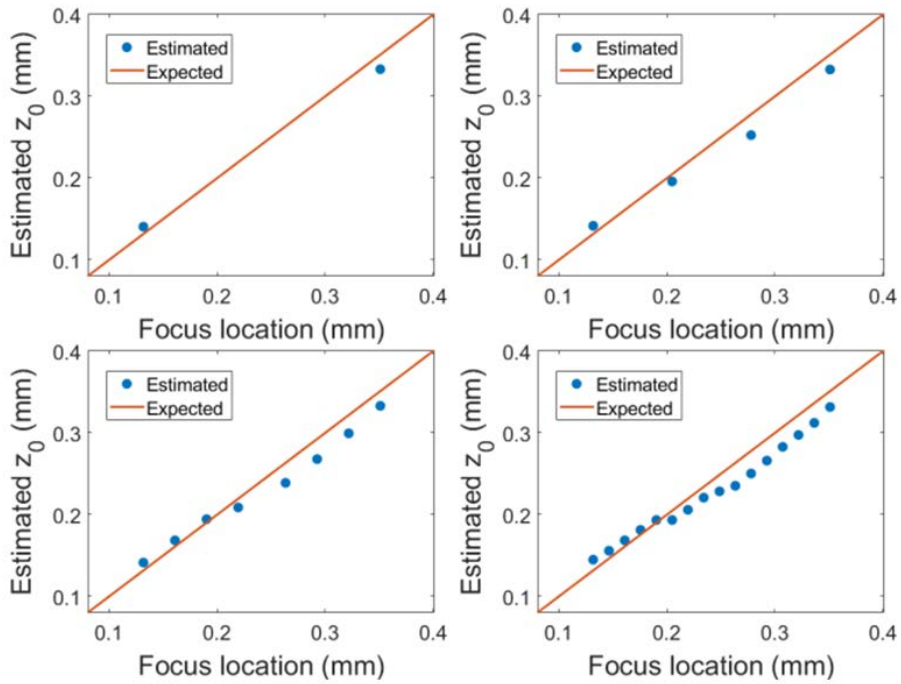


Figure 5.10 Estimated location of focus (blue dots) obtained using 2, 4, 8, and 16 B-scans recorded with different focus positions using the OCT system with the small Rayleigh length.

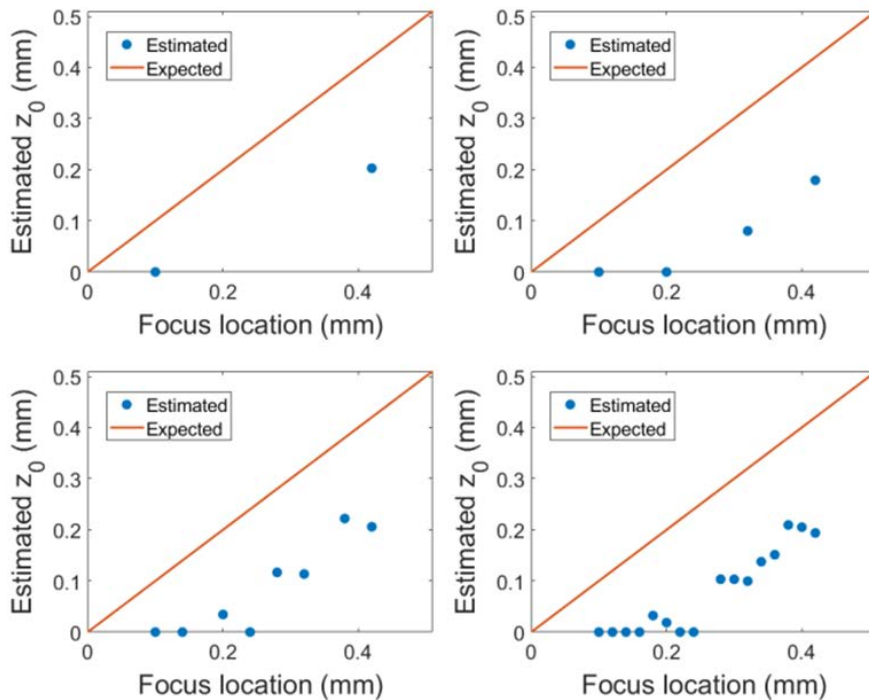


Figure 5.11 Estimated location of focus (blue dots) obtained using 2, 4, 8, and 16 B-scans recorded with different focus positions at depth using the OCT system with the large Rayleigh length.

Table 5.1 Estimated attenuation coefficients obtained using 2, 4, 8, and 16 B-scans acquired with different focus positions inside the sample for the four-layer phantom with different TiO<sub>2</sub> weight concentrations TiO<sub>2</sub> in silicone for the measurements obtained using the OCT system with the small Rayleigh length. The  $R^2$  and p-values of the linear fits to the estimated attenuation coefficients as a function of the TiO<sub>2</sub> concentration are shown for each combination of the averaged A-lines.

**Small Rayleigh length (36  $\mu\text{m}$ )**

B-scans	Layer				Linear regression	
	1	2	3	4	$R^2$	p-value
	Estimated attenuation coefficients ( $\text{mm}^{-1}$ )					
2	6.0	2.5	1.1	2.0	0.99	0.004
4	5.7	2.2	1.1	1.9	0.99	0.004
8	5.9	2.1	1.0	1.9	0.99	0.003
16	6.0	2.1	1.0	1.8	0.99	0.004

Table 5.2 Estimated attenuation coefficients obtained using 2, 4, 8, and 16 B-scans acquired with different focus positions inside the sample for the four-layer phantom with different TiO<sub>2</sub> weight concentrations TiO<sub>2</sub> in silicone for the measurements obtained using the OCT system with the large Rayleigh length. The  $R^2$  and p-values values of the linear fits to the estimated attenuation coefficients as a function of the TiO<sub>2</sub> concentrations are shown for each combination of the averaged A-lines.

**Large Rayleigh length (288  $\mu\text{m}$ )**

B-scans	Layer				Linear regression	
	1	2	3	4	$R^2$	p-value
	Estimated attenuation coefficients ( $\text{mm}^{-1}$ )					
2	5.5	2.1	1.0	1.9	0.97	0.008
4	5.6	2.2	1.0	2.0	0.98	0.008
8	5.4	2.0	1.0	1.8	0.99	0.006
16	5.5	2.0	1.0	1.8	0.98	0.005

## 5.4 Discussion

In this research, we introduced a method to estimate the attenuation coefficients of a multi-layer sample. A single-scattering model of the OCT signal was assumed while accounting for the system's roll-off, noise and focused beam shape. The model parameters of the focused axial PSF and the attenuation coefficients of each layer were simultaneously estimated from experimental OCT data.

The numerical study predicted the optimal performance, and hence the inherent limitations, of our model for two experimental systems with different Rayleigh lengths. The simulation results indicate that the proposed method can estimate the selected attenuation coefficients with an acceptable precision and accuracy ( $\text{CoV} < 10\%$ ) from the OCT signal obtained from a system with small Rayleigh length when focussing inside the sample and within 0.5 mm of the sample's surface. For the system with large Rayleigh length, while the precision of the of the estimated attenuation coefficient is acceptable ( $\text{CoV} < 10\%$ ), the bias is large when focus is inside the sample and between 0.1 mm to 0.5 mm from the sample's surface.

It has been shown that the average thickness of the retina and choroid of healthy eyes is about 250  $\mu\text{m}$  [25] and 270  $\mu\text{m}$  [26], respectively. To the best of our knowledge, in conventional ophthalmic OCT systems, the Rayleigh length is larger than 250  $\mu\text{m}$  to have chorioretinal structures within the depth of focus. For large Rayleigh lengths, the intensity and consecutively the attenuation coefficient values are less affected by the shape of the beam and therefore it is less critical for accurate estimation of the attenuation coefficient. In high resolution imaging, which in ophthalmology can be done with adaptive optics, correcting for the effect of focus to estimate the attenuation coefficient is crucial. We observed a strong linear correlation ( $R^2 > 0.92$ ,  $p\text{-value} < 0.02$ ) between the estimated attenuation coefficients and the particle concentration of the respective layer for different Rayleigh lengths.

Experimental results obtained from a single B-scan of a multi-layer phantom composed of layers with different weight concentrations  $\text{TiO}_2$  in silicone, show an acceptable fit to the measurements when the focus location is within 0.3 mm of the phantom's surface in the set of measurement with small Rayleigh lengths and for all

positions of focus for measurements with large Rayleigh lengths. We observed a good correlation between the estimated and expected focus position for the measurements obtained with the small Rayleigh length where for larger Rayleigh length this correlation was not observed. This is mainly because the larger the Rayleigh length, less changes in the signal intensity is caused by the shape of beam and therefore it is more difficult to obtain the Rayleigh length from intensity data using the model in Eq. 5.2. However, with increasing Rayleigh lengths, the intensity and consecutively the attenuation coefficient values are less affected by the shape of the beam and therefore it is less essential to take into account this effect. In ophthalmic imaging the Rayleigh length is usually large and therefore the effect of focus location is reduced. However, in finer microscopic scales using adaptive optics, correcting for the effect of focus to estimate the attenuation coefficient is crucial.

Previously, we showed that in samples with different concentrations of  $\text{TiO}_2$  dispersed in silicone there is a linear relation between the  $\text{TiO}_2$  weight concentration and the estimated attenuation coefficients [17]. Using a single B-scan, we could observe that the estimated attenuation coefficients vary significantly for different focus positions while expecting to have similar attenuation coefficient values for each layer of the sample. Despite of this large variation, we observed a strong linear correlation ( $R^2 > 0.94$ , p-value  $< 0.02$ ) between the estimated attenuation coefficients and the particle concentration of the respective layer, in the measurements obtained with both Rayleigh lengths except for focus positions higher than 0.3 mm above the sample, in the measurements obtained with the small Rayleigh length. Using multiple B-scans with different focus locations for the measurements obtained with the small Rayleigh length system, the  $R^2$ -values of the fits were higher than 0.97 (p-value  $< 0.008$ ) using 2, 3, 4 or 8 B-scans with different focus locations. The best result was obtained using the combination of 8 B-scans.

To reduce the complexity of the proposed model, we assumed the refractive index and  $C$  parameter to be constant for all depths. However, as mentioned previously, the backscattering coefficient  $\mu_{b,NA}(z)$  is proportional to  $p_{NA}(z)$ , which varies due to changes of the scatterers' phase function. We showed that we could obtain a linear relation between the estimated attenuation coefficient and different

concentration of  $\text{TiO}_2$  particles in silicone. This indicates that the effect of varying  $p_{NA}$  is not significant, but further investigation of this effect in retinal tissue measurements is required to study the effect of this assumption.

The clinical application of our proposed method for a multi-layer sample such as retinal tissue should be further investigated in future research. The limitations of our technique, i.e. setting the location of focus inside the sample and averaging rate, should be considered while acquiring the OCT scans. In clinical practice, the operator of the OCT system aims to focus on the surface of retina using a SLO camera, integrated into the OCT system. To increase the depth of focus in chorioretinal structures, the location of focus should be inside the retina. However due to the head movements, the focus location varies during acquisition. Further investigation is required to study the variation of focus location due to head movements.

## References

- [1] K. A. Vermeer, J. van der Schoot, H. G. Lemij, and J. F. de Boer, "RPE-normalized RNFL attenuation coefficient maps derived from volumetric OCT imaging for glaucoma assessment," *Invest. Ophthalmol. & Vis. Sci.* **53**, 6102-6108 (2012).
- [2] R. A. McLaughlin, L. Scolaro, P. Robbins, C. Saunders, S. L. Jacques, and D. D. Sampson, "Parametric imaging of cancer with optical coherence tomography," *J. Biomed. Opt.* **15**, 046029 (2010).
- [3] K. Barwari, D. M. de Bruin, E. C. Cauberg, D. J. Faber, T. G. van Leeuwen, H. Wijkstra, J. de la Rosette, and M. P. Laguna, "Advanced diagnostics in renal mass using optical coherence tomography: a preliminary report," *J. Endourol.* **25**, 311–3115 (2011).
- [4] K. Barwari, D. M. de Bruin, D. J. Faber, T. G. van Leeuwen, J. J. de la Rosette, and M. P. Laguna, "Differentiation between normal renal tissue and renal tumors using functional optical coherence tomography: a phase I in vivo human study," *BJU International* **110**, E415–E420 (2012).
- [5] P. H. Tomlins, O. Adegun, E. Hagi-Pavli, K. Piper, D. Bader, and F. Fortune, "Scattering attenuation microscopy of oral epithelial dysplasia," *J. Biomed. Opt.* **15**, 066003 (2010).
- [6] Q. Q. Zhang, X. J. Wu, T. Tang, S. W. Zhu, Q. Yao, B. Z. Gao, and X. C. Yuan, "Quantitative analysis of rectal cancer by spectral domain optical coherence tomography," *Phys. Med. Biol.* **57**, 10 (2012).

- [7] F. J. van der Meer, D. J. Faber, D. M. B. Sassoon, M. C. Aalders, G. Pasterkamp, and T. G. van Leeuwen, "Localized measurement of optical attenuation coefficients of atherosclerotic plaque constituents by quantitative optical coherence tomography," *IEEE Trans. Med. Imag.* **24**, 1369–1376 (2005).
- [8] D.J.Faber, F.J. van der Meer, M. C. G. Aalders, and T. G. van Leeuwen, "Quantitative measurement of attenuation coefficients of weakly scattering media using optical coherence tomography," *Opt. Express* **12**, 4353–65, 2004.
- [9] G. van Soest, T. Goderie, E. Regar, S. Koljenovic, G. L. J. H. van Leenders, N. Gonzalo, S. van Noorden, T. Oka-mura, B. E. Bouma, G. J. Tearney, J. W. Oosterhuis, P. W. Serruys, and A. F. W. van der Steen, "Atherosclerotic tissue characterization in vivo by optical coherence tomography attenuation imaging," *J. Biomed. Opt.* **15**, 11105-11114 (2010).
- [10] J. M. Schmitt, A. Knüttel, M. Yadlowsky, and M. A. Eckhaus, "Optical-coherence tomography of a dense tissue: statistics of attenuation and backscattering," *Phys. Med. Biol.* **39**, 1705-1720 (1994).
- [11] K. A. Vermeer, J. Mo, J. J. Weda, H. G. Lemij, and J. F. de Boer, "Depth-resolved model-based reconstruction of attenuation coefficients in optical coherence tomography," *Biomed. Opt. Express* **5**, 322-337 (2013).
- [12] A. I. Kholodnykh, I. Y. Petrova, K. V. Larin, M. Motamedi, and R. O. Esenaliev, "Precision of Measurement of Tissue Optical Properties with Optical Coherence Tomography", *Appl. Opt.* **42**, 3027-3037 (2003).
- [13] L. Thrane, H. T. Yura, and P. E. Andersen, "Analysis of optical coherence tomography systems based on the extended Huygens Fresnel principle," *J. Opt. Soc. Am. A* **17**, 484-490 (2000).
- [14] V. Duc Nguyen, D. J. Faber, E. van der Pol, T. G. van Leeuwen, and J. Kalkman, "Dependent and multiple scattering in transmission and backscattering optical coherence tomography," *Opt. Express* **21**, 29145-29156 (2013).
- [15] G. T. Smith, N. Dwork, D. O'Connor, U. Sikora, K. L. Lurie, J. M. Pauly, and A. K. Ellerbee, "Automated, depth-resolved estimation of the attenuation coefficient from optical coherence tomography data," *IEEE Trans. Med. Imaging* **34**, 2592–2602 (2015).
- [16] S. Stefan, K. S. Jeong, C. Polucha, N. Tapinos, and S. A. Toms, and J. Lee, "Determination of confocal profile and curved focal plane for OCT mapping of the attenuation coefficient," *Biomed. Opt. Express* **9**, 5084–5099 (2018).

- [17] B. Ghafaryasl, K. A. Vermeer, J. Kalkman, T. Callewaert, J. F. de Boer, and L. J. van Vliet, "Analysis of attenuation coefficient estimation in Fourier-domain OCT of semi-definite media," *Biomed. Opt. Express*, **11**, 6093-6107 (2020).
- [18] S. H. Yun, G. J. Tearney, B. E. Bouma, B. H. Park, and J. F. de Boer, "High-speed spectral-domain optical coherence tomography at 1.3  $\mu$  m wavelength," *Opt. Express* **11**, 3598-3604 (2003).
- [19] V. M. Kodach, D. J. Faber, J. van Marle, T. G. van Leeuwen, and J. Kalkman, "Determination of the scattering anisotropy with optical coherence tomography", *Opt. Express* **19**, pp. 6131-6140 (2011).
- [20] T. G. van Leeuwen, D. J. Faber, and M. C. Aalders, "Measurement of the axial point spread function in scattering media using single-mode fibre-based optical coherence tomography," *IEEE J. Sel. Top. Quant. Electr.* **9**, 227–233 (2003).
- [21] J. Kalkman, "Fourier-domain optical coherence tomography signal analysis and numerical modeling," *Int. J. Opt.* 2017, 1 (2017).
- [22] T. Callewaert, J. Dik, and J. Kalkman, "Segmentation of thin corrugated layers in high-resolution OCT images," *Opt. Express* **25**, 32816–28 (2017).
- [23] B. Braaf, K. A. Vermeer, K. V. Vienola, and J. F. de Boer, "Angiography of the retina and the choroid with phase-resolved OCT using interval-optimized backstitched B-scans," *Opt. Express* **20**, 20516–20534 (2012).
- [24] E. W. Dijkstra, "A note on two problems in connexion with graphs," *Numerische Mathematik* **1**, 269-271 (1959).
- [25] B. Alamouti, and J. Funk, "Retinal thickness decreases with age: an OCT study," *J Ophthalmol.* **87**, 899– 901 (2003).
- [26] V. Manjunath, M. Taha, J.G. Fujimoto, and J.S. Duker, "Choroidal thickness in normal eyes measured using Cirrus HD optical coherence tomography," *Am J Ophthalmol.* **150**, 325–329 (2010).



# 6 Automatic estimation of retinal nerve fibre bundle orientation in SD-OCT images using a structure-oriented smoothing filter

---

Optical coherence tomography (OCT) yields high-resolution, three-dimensional images of the retina. A better understanding of retinal nerve fibre bundle (RNFB) trajectories in combination with visual field data may be used for future diagnosis and monitoring of glaucoma. However, manual tracing of these bundles is a tedious task. In this work, we present an automatic technique to estimate the orientation of RNFBs from volumetric OCT scans. Our method consists of several steps, starting from automatic segmentation of the RNFL. Then, a stack of en face images around the posterior nerve fibre layer interface was extracted. The image showing the best visibility of RNFB trajectories was selected for further processing. After denoising the selected en face image, a semblance structure-oriented filter was applied to probe the strength of local linear structure in a discrete set of orientations creating an orientation space. Gaussian filtering along the orientation axis in this space is used to find the dominant orientation. Next, a confidence map was created to supplement the estimated orientation. This confidence map was used as pixel weight in normalized convolution to regularize the semblance filter response after which a new orientation estimate can be obtained. Finally, after several iterations an orientation field corresponding to the strongest local orientation was obtained. The RNFB orientations of six macular scans from three subjects were estimated. For all scans, visual inspection shows a good agreement between the estimated orientation fields and the RNFB trajectories in the en face images. Additionally, a good correlation between the orientation fields of two scans of the same subject was observed. Our method was also applied to a larger field of view around the macula. Manual tracing of the RNFB trajectories shows a good agreement with the automatically obtained streamlines obtained by fibre tracking.

B. Ghafaryasl, R. Baart, J.F. de Boer, K. A. Vermeer, L. J. van Vliet, Automatic estimation of retinal nerve fibre bundle orientation in SD-OCT images using a structure-oriented smoothing filter, *Medical Imaging 2017: Image Processing*, **10133**, 101330-101336 (2017).

## 6.1 Introduction

The retinal nerve fibre layer (RNFL) carries visual information from the eye to the visual cortex of the brain. The retinal nerve fibre bundles (RNFBs), which consist of retinal ganglion cell axons, may degenerate in the retina of glaucoma patients. A patient-specific RNFB trajectory pattern in combination with visual field data can give us a better understanding of glaucomatous damage [1]. However, manual tracing of the RNFBs in fundus images is time consuming, error-prone and grader-dependent. Recently, a method has been developed to create a map of RNFB trajectories using the mean RNFL thickness at each grid sector of the visual field [1,2]. However, this map is limited to the resolution of the visual field grid and does not use patient-specific information of RNFB trajectories. In this chapter, we present a method to automatically estimate the RNFB orientations in volumetric spectral-domain OCT (SD-OCT) images. Our method applies a 2D structure-oriented semblance filter to probe the orientation responses from an en face OCT image with visible trajectories of RNFBs.

## 6.2 Method

Since RNFBs traverse across the structure of the RNFL, their trajectory is not visible in a single C-scan. Therefore, to visualize the RNFBs, en face images oriented along the RNFL were extracted. In the first step, 3D macular SD-OCT scans were automatically segmented using coupled level sets [3] since the built-in segmentation of RNFL by the scanner was not accurate for some of the B-scans. Then, the en face image showing the best visibility of the RNFB trajectories was selected for further processing. This image was extracted from a  $3.9\ \mu\text{m}$  (1 pixel) thin slice located  $7.8\ \mu\text{m}$  (2 pixels) anterior to the segmented posterior nerve fibre layer interface (Fig. 6.1(a)). The horizontal band artifacts in the en face image results from the fast horizontal scanning direction. To eliminate these artifacts in the en face image, the following steps have been performed. First, the low frequencies of the en face image were removed using a 2D Gaussian filter (Fig. 6.1(b)). Second, since the banding artifact is the dominant orientation at each column of the en face image, a principal component analysis (PCA) was applied to the columns of an image and the image was reconstructed without the first four components, which are dominated by the horizontal band artifacts (Fig. 6.1(c)).

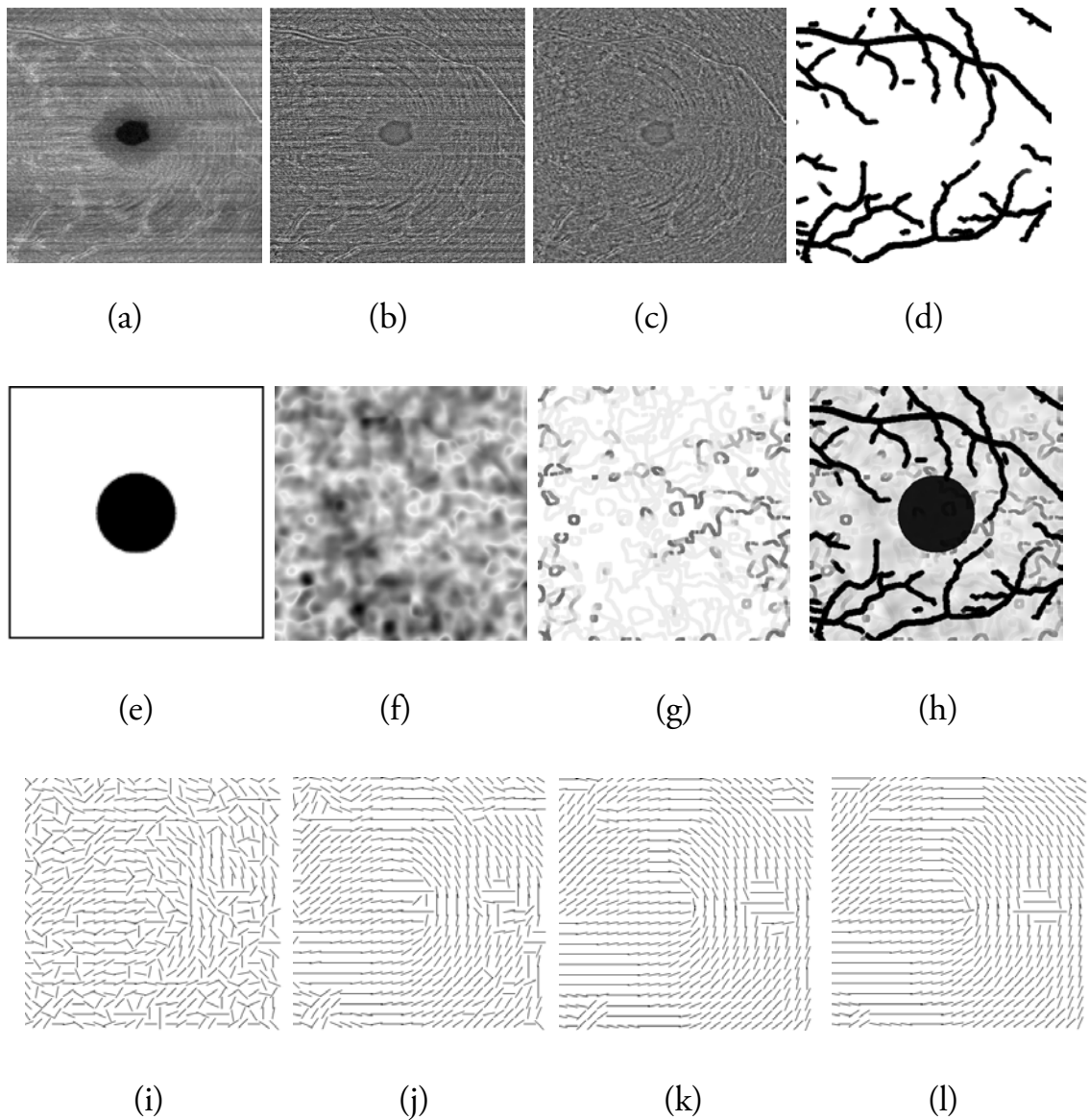


Figure 6.1 a) The en face image of a macular SD-OCT scan; b) after removing the low frequencies; c) after removing the horizontal band artifacts. d) The blood vessels mask. e) The macula mask. The confidence maps of: f) the variance of the residual between the best-fitted Gaussian kernel and the orientation measurements; g) the dilated inverted orientation gradient (white color shows the highest weight). h) The combined certainty weight image. i-l) The orientation fields for 0, 2, 30 and final result (after 32 iterations).

To estimate the orientation of the image structures, a 2D structure oriented semblance filter was used [6]. Semblance,  $s$ , is a measure of similarity along vector  $j'$ , smoothed along its orthonormal vector  $i'$  at each location in image  $I$ ,

$$s_{i',j'} = \frac{\langle \langle I \rangle_{j'}^2 \rangle_{i'}}{\langle \langle I^2 \rangle_{j'} \rangle_{i'}}, \quad (6.1)$$

where  $\langle . \rangle_k$  indicates smoothing along  $k$ , usually by a 1D Gaussian kernel. At each pixel, the orientation responses, which are the similarity measurements for each orientation of the filter, were obtained with  $N$  equally spaced orientations of the semblance filter between 0 and  $\pi$ . Stacking the filter outputs as a function of the probed orientation yields a so-called orientation space.

The orientation coordinate of this orientation space is periodic with 180 degrees, such that the orientations 0 and  $\pi$  are the same. Taking this into account, the following normalized Gaussian-based kernel for different  $\theta_i$  was used to find the best orientation response,

$$G_i(\theta) = \frac{g_i(\theta) + g_i(\theta + \pi) + g_i(\theta - \pi)}{\sum_{\phi \in \Phi} (g_i(\phi) + g_i(\phi + \pi) + g_i(\phi - \pi))}, \quad \theta \in \Phi, \quad (6.2)$$

where  $\Phi$  is a set of orientations and

$$g_i(\theta) = e^{\frac{-(\theta - \theta_i)^2}{2\sigma^2}}. \quad (6.3)$$

The standard deviation  $\sigma$  is set to the (uniform) orientation sampling pitch,  $\sigma = \pi/N$ . At each pixel, we calculated the variance of the residual between the Gaussian-based kernel centered at  $\theta_i$  and the orientation measurements. The dominant orientation at each pixel corresponds to the orientation with the minimum residual variance.

A normalized convolution was used to regularize the orientation responses  $F$  for all orientations  $\theta_i$ , using a certainty weight image  $C$  [7], such that:

$$R_s = \frac{(F \cdot C) * G}{F * G}, \quad (6.4)$$

where  $*$  indicates convolution,  $R_s$  is the regularized orientation response, and  $G$  is a Gaussian filter.

The certainty weight image was obtained by the scalar products of two confidence maps and two binary masks. The first confidence map is the relative

strength of the strongest response. This is the inverse of the variance of the residue between the best-fitted Gaussian kernel and the measured orientation responses, normalized by the maximum value of the residue variances over all orientations and pixels. The second confidence map is composed of a local consistency weight, which indicates the similarity of the orientations between neighboring pixels. This can be obtained by dilating the inverted gradient of the extracted dominant orientation image. Two binary masks were used to give zero weights to areas occupied by blood vessels and by the macula.

To detect the blood vessels, an en face image was created from an axial summation of the 3D-OCT data between the vitreous-RNFL interface and RPE in the segmented retina. Then, a vesselness enhancement filter [8] based on a Gaussian kernel was applied to the extracted en face image. The scale of the Gaussian corresponded to the width of the smallest vessel. The blood vessels were segmented by thresholding the filter response and removing connected components smaller than 20 pixels. Finally, the segmented blood vessels were dilated using a round structuring element. The macula mask was considered as a circle in the center of the en face image and has an average diameter of 1.5 mm.

The result of normalized convolution is a set of regularized orientation responses. Based this set of orientation responses we can repeat the same procedure and extract the dominant orientation for each pixel. From here the entire procedure can be repeated in an iterative manner. Each iteration of the normalized convolution yields further regularized orientation responses and new weights for the next iteration. The differences between consecutive orientation fields were calculated by,

$$d(f_n, f_{n-1}) = \sum_x \sum_y \left( \min \left( |f_n(x, y) - f_{n-1}(x, y)|, \left| \text{mod} \left( f_n(x, y) + \frac{\pi}{2}, \pi \right) - \text{mod} \left( f_{n-1}(x, y) + \frac{\pi}{2}, \pi \right) \right| \right) \right)^2 \quad (6.5)$$

where  $f_n(x, y)$  is the dominant orientation at pixel  $(x, y)$  for  $n^{\text{th}}$  iteration. The stopping criterion,  $d(f_n, f_{n-1}) \geq 0.9 \times \frac{\sum_{m=n-4}^{n-1} d(f_m, f_{m-1})}{4}$ , is used to terminate the iterative process.

### 6.3 Experiments and results

We obtained two consecutive three-dimensional macular OCT scans of three subjects using a Spectralis SD-OCT system (Heidelberg Engineering, Germany). The voxel size of all six scans was  $3.9\ \mu\text{m}$  in axial and  $11.3\ \mu\text{m}$  in both lateral directions. An en face image was subsequently extracted from the volume following anterior of the segmented posterior nerve fibre layer interface. The horizontal band artifacts were removed, as described previously. The standard deviation of the isotropic Gaussian filter to remove the low frequencies was set to  $56\ \mu\text{m}$ , by considering the width of the horizontal bands (Fig. 6.1(b-c)).

The distance over which the orientation and intensity of a nerve fibre is consistent was estimated to be  $135\ \mu\text{m}$ . This similarity distance,  $d_{sim}$ , was used for setting the parameters of the semblance filter and the normalized convolution. The standard deviation of the semblance Gaussian filter was set to  $d_{sim}/4$ . The number of orientations  $N$  was set to 16 between 0 and  $\pi$ . The standard deviation of the 1D Gaussian kernel to implement the semblance responses as a function of orientation was set to  $\pi/16$ . The standard deviation of the isotropic 2D Gaussian kernel as used in the normalized convolution was set to  $2 \times d_{sim}$ . The scale of the 2D isotropic Gaussian kernel for vessel enhancement was set to  $20\ \mu\text{m}$ . The segmented blood vessels were dilated by using an approximately round 2D structuring elements with a radius of  $d_{sim}/4$ . The blood vessels and macula masks are shown in Fig. 6.1(d-e). The confidence maps based on the variance of orientation residue and the dominant orientation gradient are shown in Fig. 6.1(f-g). The combined certainty weight image is shown in Fig. 6.1(h). The dominant orientation responses for 0, 2 and 30 iterations and final result (after 32 iterations). are shown in Fig. 6.1(i-l). The estimated orientation fields of six scans from three normal subjects are shown in Fig. 6.2.

In a second experiment, the scans of a normal subject was obtained for a larger field of view covering the temporal region of macula (Fig. 6.3). The estimated orientations are shown both as vector field (second column) and as streamlines (third column) [MATLAB 2013b and image processing Toolbox, The MathWorks, Inc]. To obtain the streamlines, the direction of the estimated vectors were forced to run from the right to the left side of the image, which is aligned with the

direction of the photoreceptors in the RNFB to the brain. The streamlines propagate along the orientation of the vectors in both directions, starting from a regular grid of points with a uniform spacing in both  $x$  and  $y$  direction over the entire image. The last column shows the comparison of some of the automatically estimated (red curves) and manually traced (dashed yellow curves) RNF bundles. The manual tracing was performed from the starting point of the streamline until the trajectory of RNF bundle is no longer visible by the human eye.

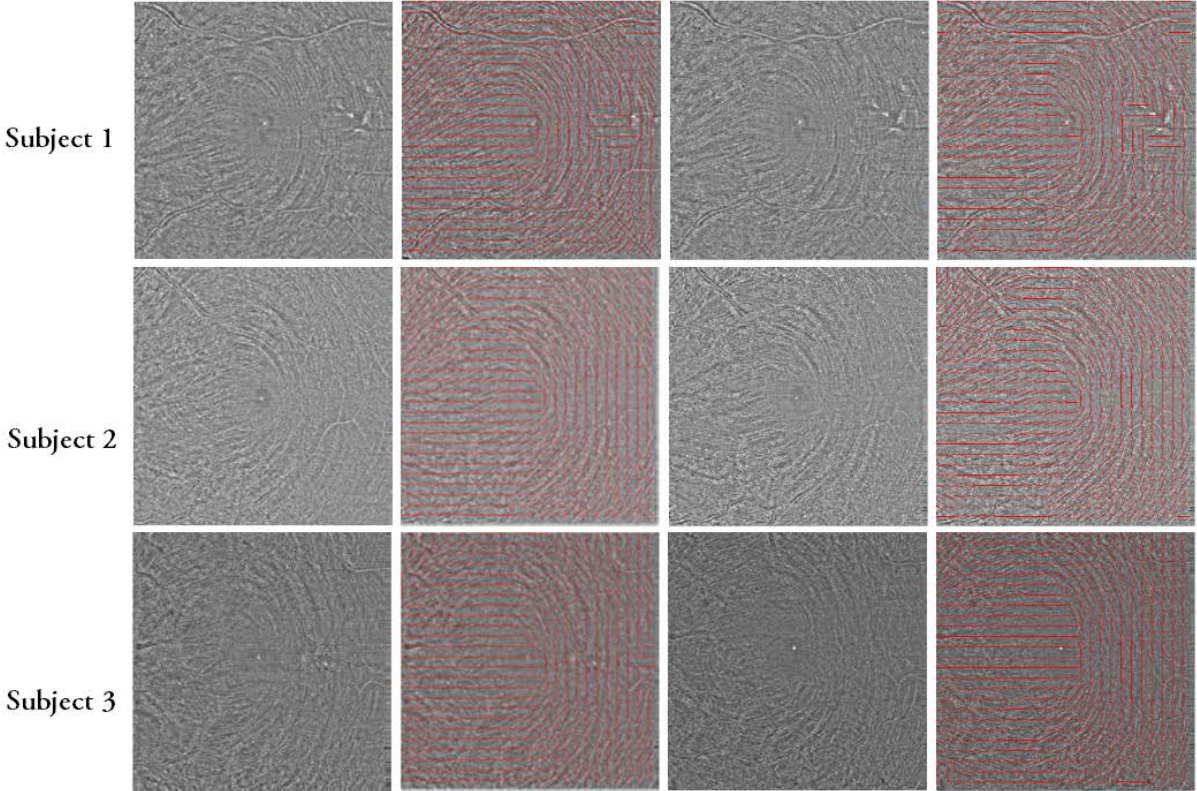


Figure 6.2 The en face images after removing the horizontal band artifacts and the estimated orientation field (superimposed in red) for three normal subjects and two subsequently made scans per each subject.

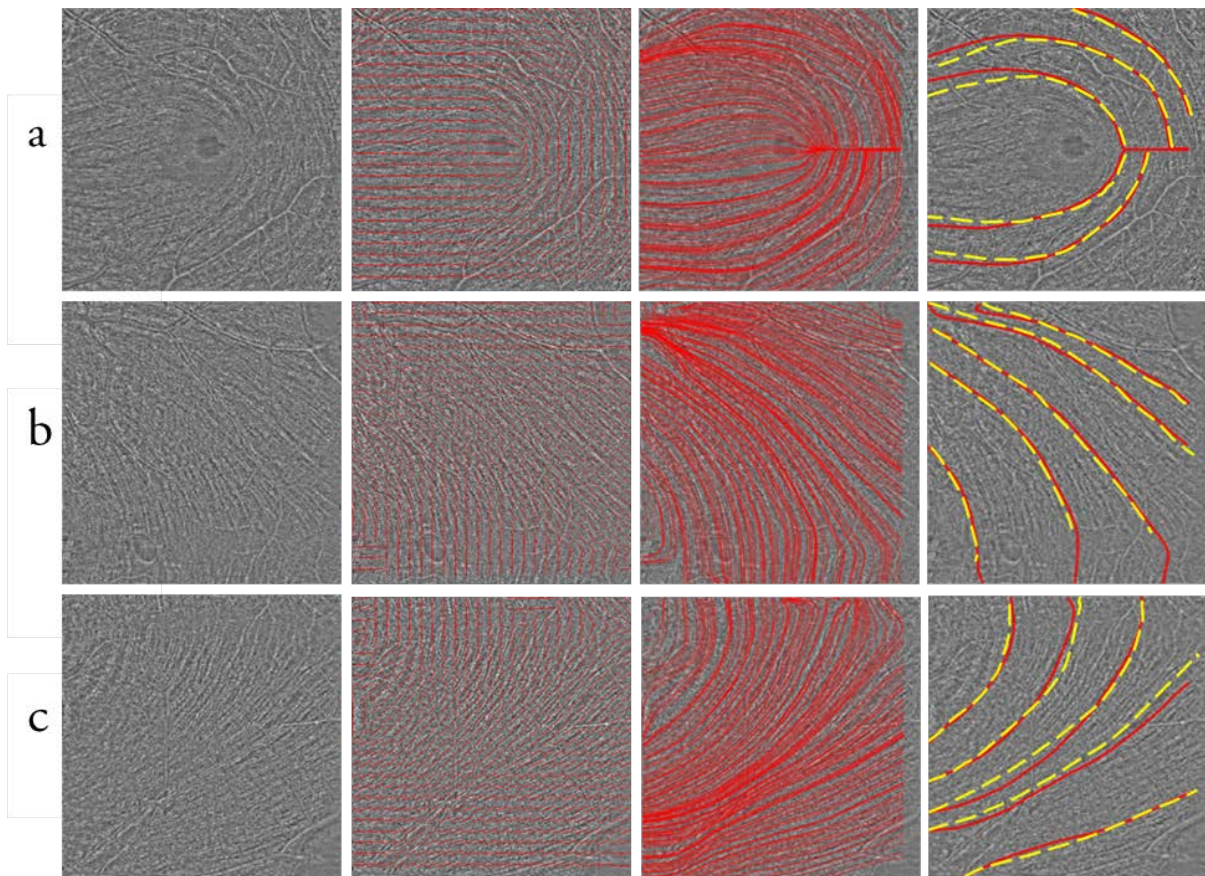
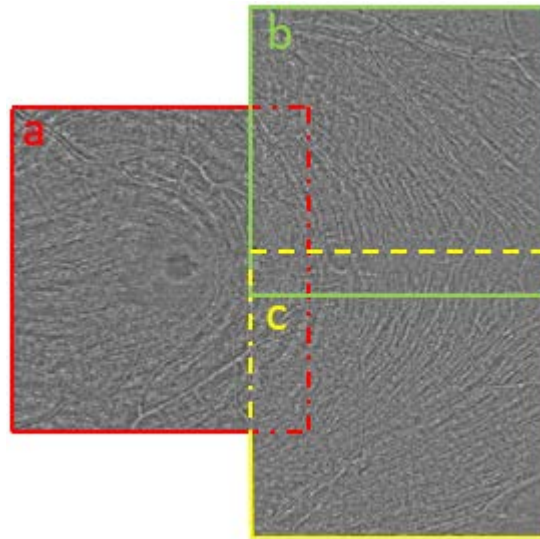


Figure 6.3 Top) A larger field of view of RNF bundle trajectories by stitching three en face images (a,b and c) obtained from the B-scans of macula and the temporal region. Bottom) First column: The enhanced en face images; second column: the vector field; third column: the estimated streamlines; fourth column: manually traced RNF bundles (dashed yellow curves) and the corresponding streamlines (red curve).

## 6.4 Conclusion

In this chapter, we presented an automatic method for estimating the orientation of RNFBs from volumetric SD-OCT images. The method is based on an orientation map estimated based on the responses of the structure-oriented semblance filter in 16 uniformly sampled probe orientations between 0 and 180 degrees. The estimated orientations show a good agreement with visual inspection of the RNFBs in en face images following the anterior of the segmented posterior nerve fibre layer interface. In Fig. 6.2 and subject 1, the orientation field at the bottom-left corner is influenced by the presence of a blood vessel. A more accurate vessel segmentation tool can improve the results for these regions. The automatic tracing of RNF bundles over a larger field of view shows an acceptable correlation with the manual tracing in the area where the bundles are visible.

## References

- [1] M. K. Garvin, M.D. Abramoff, K. Lee, M. Niemeijer, M. Sonka, Y. H. Kwon, "2-D pattern of nerve fibre bundles in glaucoma emerging from spectral-domain optical coherence tomography." *Investigative Ophthalmology & Visual Sciences*. **53**(1), 483-489 (2012).
- [2] K. Lee, H. Bogunovic, Y. H. Kwon, M. K. Garvin, A. Wahle, M. Sonka, "Automated Identification of Retinal Nerve Fiber Bundle Connectivity in 9-field SD-OCT." *Investigative Ophthalmology & Visual Sciences*. ARVO Annual Meeting. Seattle, WA. Abstract Number, 594 (2016).
- [3] J. Novosel, G. Thepass, H. G. Lemij, J. F. de Boer, K. A. Vermeer, van L. J. Vliet., "Loosely coupled level sets for simultaneous 3D retinal layer segmentation in optical coherence tomography." *Medical Image Analysis J.* **26** (1), 146-58 (2015).
- [4] W. H. Richardson, "Bayesian-based iterative method of image restoration", *J. Opt. Soc. Am.* **62**, 55–59 (1979).
- [5] L. B. Lucy, "An iterative technique for the rectification of observed distributions.", *Astronomy J.* **79**, 745–765 (1974).
- [6] D. Hale, "Structure-oriented smoothing and semblance." Center for wave phenomena report, **635**, 261–270 (2009).
- [7] D. Knutsson, C.F. Westin, "Normalized and differential convolution." *Proceedings CVPR*, 515-523 (1993).
- [8] A. F. Frangi, W. J. Niessen, K. L. Vincken, and M. A. Viergever, "Multiscale vessel enhancement filtering." *Lecture Notes in Computer Science*, 130–137 (1998).



## 7 Conclusion and future work

---

In this thesis, we aimed to provide better quantitative description of retinal tissue based on OCT data. In particular we investigated methods to obtain an unbiased and precise estimate of optical and structural properties of the RNFL. Our techniques may be used in combination with others for monitoring longitudinal changes in retinal tissue and diagnosis of diseases such as glaucoma in the future.

To investigate the forward model of the light we presented two methods to simulate the OCT signal for various focus locations above and inside semi-infinite samples with different attenuation coefficients in Chapter 2. The simpler model only uses the attenuation coefficient, the shape of the OCT beam and a scaling factor to model the OCT signal. The more complex simulation also takes into account the interference of the electrical fields in the sample and reference arms and several post-processing steps. In the area with larger SNRs, the simulation results using both methods were similar to each other. The thesis includes a method to estimate the sample attenuation coefficients by fitting an OCT light model to the OCT measurements. In this method, the parts of the OCT signal with the larger SNRs have more impact on the fit of the model to the signal. Therefore, we disregarded the differences between the OCT signals in the simulated OCT signals for small SNRs and used the simpler method as a model of the OCT signal. We concluded that there are differences between the simulation results and the measurements which were mainly caused by a mismatch between the parameter values of the simulation and the experimental set-up.

Previously, a depth-resolved space-variant method was developed to estimate the attenuation coefficients of inhomogeneous media. The existing method relies on the integration of the OCT signals at the larger depths, which may result in a variation of the estimated attenuation coefficients due to the presence of noise in regions where the OCT light was fully attenuated. To improve the existing method, two methods were introduced in Chapter 3 to improve the quality of the attenuation coefficient images: I) by subtracting the average noise signal from the OCT data; II) by excluding the noise region below the retina where the OCT light

was fully attenuated. The inter- and intra- Aline variations were calculated per scan to quantify the performance of our method. The results show that only excluding the noise region reduces the inter-A-line variation by 0.01, 0.03 and 0.07 in RPE, Choroid and Sclera, respectively, and the intra-Aline variation by 0.03 in Sclera. This method yields the largest improvement in the quality of the attenuation coefficient images in the sub-RPE region. As a consequence, the improved method may contribute to better visualization and segmentation of choroidal and scleral pathology.

As previously mentioned, the OCT model of Chapter 2 was used to develop a method to estimate the attenuation coefficients of a single-layer sample while compensating for the effect of the shape of the OCT beam in Chapter 4. The model parameters of the focused axial PSF and the attenuation coefficients were estimated simultaneously from experimental OCT data. A numerical study was performed to predict the performance and limitations of the proposed method for different experimental conditions. The numerical results predict that for a Rayleigh length smaller than 300  $\mu\text{m}$  the estimation error of attenuation coefficient is smaller than 10% when the location of the focused beam was inside the sample. To the best of our knowledge, Rayleigh lengths below 500  $\mu\text{m}$  are within the range of the Rayleigh lengths in clinical OCT systems. For the location of focus above the sample the estimation error is larger than 10% and not acceptable. Our method was evaluated on measured data obtained from a single-layer homogenous phantom from an experimental OCT system. An acceptable fit to the measurements was observed for different focus positions. The results showed an excellent correlation between the estimated attenuation coefficients in different B-scans and no descending bias was observed for a single or multiple B-scans. It has been shown previously that the measured attenuation coefficient falls below the expected values for increasing particles concentration due to an increase of multiple scattering, which was not included by the model in the current study. Applying a multiple-scattering model may result in a better correlation between the measurements and the OCT light model.

In applications such as ophthalmology, each retina layer has different optical properties. Therefore, in Chapter 5, we extended the previous method to estimate the attenuation coefficients of a multi-layer sample while compensating for the

effect of shape of the OCT beam. The extension of the aforementioned single-scattering model of the OCT signal in a multi-layer sample was assumed while accounting for the system's roll-off, noise and focused beam shape. The model parameters of the focused axial PSF and the attenuation coefficients were estimated simultaneously from experimental OCT data.

A Monte Carlo simulation was used to predict the performance of the method for OCT signals obtained from a system with either a small (40  $\mu\text{m}$ ) or a larger (300  $\mu\text{m}$ ) Rayleigh length. The numerical evaluation shows that when the focus is inside the sample, an acceptable estimation of the attenuation coefficient from the data with small Rayleigh length can be obtained. The precision of the estimated attenuation coefficients from the data with a larger Rayleigh length is acceptable, however a large bias due to incorrect estimation of the focus location was observed.

In experiments with a multi-layer phantom with different weight-concentrations of  $\text{TiO}_2$  in silicone, good fits of the model to the measurements were achieved using a single B-scan as well as multiple B-scans acquired for different focus positions. We observed using a single B-scan that there is a large variation between the estimated attenuation coefficients for different focus locations. However, for both small and large Rayleigh lengths, a linear relation, with  $R^2$  higher than 0.97 (p-value < 0.008), between the estimated attenuation coefficients and the particle concentration of the perspective layer was observed while using multiple B-scans.

Finally, to investigate the structural properties of the OCT data, an automatic method was presented to estimate the orientation of the retinal nerve fibre bundles from volumetric OCT data in Chapter 6. The method is based on a structure-oriented semblance filter which provides us with a measurement to identify the dominant orientation of the image structures. The estimated orientations show a good agreement with the manual tracing of the RNFBs. Integrating the RNFBs orientation map into the other diagnostic techniques like VF and SAP should be further investigated to help future glaucoma studies.

The proposed techniques in this thesis can be used in further investigation of the optical and structural characteristics of retinal tissues in chorioretinal diseases. The clinical applications of our proposed method for a multi-layer sample should be further investigated using retinal OCT scans. For this, the limitations of our

technique, i.e. setting the location of focus inside the sample and averaging rate, should be taken into account while acquiring the OCT scans. In clinical practice, the operators of the OCT system aim to focus on the surface of retina using an integrated SLO camera to obtain high quality images of retina. However, due to the head movements, the focus location varies during the acquisition time. Therefore, further improvement is required in the design of the OCT systems to automatically focus the OCT beam inside the sample to be able to use the proposed method in clinical systems. In addition, to obtain an accurate estimation of the RNFBs, the scans with high spatial optical resolutions are required. Hence, applying the proposed methods in clinical applications will be facilitated by the development of proper acquisition protocols and ideally will help to have an early diagnosis and treatment of chorioretinal diseases.

## 8 Summary

---

Early diagnosis of retinal diseases such as glaucoma will benefit from unbiased and precise estimation of both optical and structural properties of the RNFL as they provide a better understanding of the tissue characteristics. The main objective of this thesis was first to improve the estimation of the attenuation coefficients of layered samples and, second, to estimate the structural properties of RNFL.

Unbiased estimation of optical tissue properties such as the attenuation coefficient require a model of the recorded OCT signal. To study the characteristics of the OCT signal, in Chapter 2, two simulation methods were presented for homogeneous samples. In both methods single-scattering of the OCT light was assumed and the effect of the shape of OCT beam was taken into account. The more complex simulation also takes into account the interference of the electrical fields in the sample and reference arms and several post processing steps. Later in this thesis the simpler model was used to model the OCT signal since both simulation methods generated similar results.

In Chapter 3, we improved an existing depth-resolved method to estimate the attenuation coefficients. The existing method does not handle noise at the larger depths, where the OCT light is fully attenuated, which results in a variation of the estimated attenuation coefficient values. We introduced a technique to detect and exclude the noise regions from the OCT scans to improve the accuracy and reduce the Aline-by-Aline variation of the estimated attenuation coefficients. The results show a better accuracy of the estimated attenuation coefficient, especially in sub-RPE regions and a better quality of the attenuation coefficient images.

In Chapter 4, a method was presented to estimate the attenuation coefficients of a homogeneous medium accounting for the shape of the focused light beam. For this, the model presented in Chapter 2 was fitted to the measured OCT signal of a

homogeneous sample to estimate the model parameters. The presented method was first implemented for the semi-infinite samples and was tested for different concentrations of  $\text{TiO}_2$  in silicone for different locations of focus. In addition, a statistical and numerical analysis was performed to evaluate the presented method under various experimental conditions. The estimation result shows a reasonable correlation between the  $\text{TiO}_2$  weight-concentration and the estimated attenuation coefficient. While the method could estimate the attenuation coefficients of a uniform samples, most biological tissues such as the retina are layered, hence the method was extended in Chapter 5 to estimate the attenuation coefficients of the multi-layer samples. This method was tested on the simulation and measurements of a multi-layer phantom with different concentration of  $\text{TiO}_2$  in silicone with two systems: one with a small ( $40 \mu\text{m}$ ) and one with a larger ( $300 \mu\text{m}$ ) Rayleigh length. The numerical results show an acceptable estimation of the attenuation coefficients for the Rayleigh lengths less than  $0.5 \text{ mm}$  in air and acceptable for clinical application using clinical OCT systems. For both single- and multi-layer samples, a linear relation between the estimated attenuation coefficients and the particle concentration of the perspective layer was observed while using single and multiple B-scans.

In Chapter 6, an automatic technique was developed to estimate the orientation of RNFBs from volumetric OCT scans. The RNFB orientations of six macular scans from three subjects were used to evaluate the results. We observed a good correlation between the manual tracing and the estimated orientations of the RNFLs. RNFBs orientation in combination with other techniques such as VF and SAP can assist the ophthalmologists to have a more reliable measurement for an early diagnosis of retinal diseases such as glaucoma.

# 9 Publications

---

## Publications contributing to this thesis

**B. Ghafaryasl**, K. A. Vermeer, J. Kalkman, T. Callewaert, J. F. de Boer, L. J. van Vliet, “Attenuation coefficient estimation in Fourier-domain OCT of multi-layered phantoms,” *Biomed. Opt. Express*, **12**, 2744-2758 (2021).

**B. Ghafaryasl**, K. A. Vermeer, J. Kalkman, T. Callewaert, J. F. de Boer, and L. J. van Vliet, “Analysis of attenuation coefficient estimation in Fourier-domain OCT of semi-definite media,” *Biomed. Opt. Express*, **11**, 6093-6107 (2020).

**B. Ghafaryasl**, K. A. Vermeer, J. Kalkman, T. Callewaert, J. F. de Boer, L. J. van Vliet, “Accurate estimation of the attenuation coefficient from axial point spread function corrected OCT scans of a single layer phantom,” *Proc. SPIE 10483, Optical Coherence Tomography and Coherence Domain Optical Methods in Biomedicine*, 104832B (2018).

**B. Ghafaryasl**, K. A. Vermeer, J. F. de Boer, M. E.J. van Velthoven, L. J. van Vliet, “Noise-adaptive attenuation coefficient estimation in spectral domain optical coherence tomography data,” *Proc. International Symposium on Biomedical Imaging* (2016).

**B. Ghafaryasl**, J. Novosel, H. G. Lemij; J. F. De boer, K. A. Vermeer, L. van Vliet, “Automatic estimation of retinal nerve fiber bundle orientation in SD-OCT images,” *ARVO* (2014).

## Other publications

L.H.M. Pierrache, **B. Ghafaryasl**, S. Yzer, M. Khan, M. van Genderen, J. Schuil, N. Boonstra, J. Willem, R. Pott, J. de Faber, M. Sang, F. Cremers, C. Klaver, L. I. van den Born, “Natural history of *RPE65*-mediated inherited retinal dystrophies,” *Retina*, **40**, 1812-1828 (2020).

F. Visser, K.A. Vermeer, **B. Ghafaryasl**, A. Vlaar, H. C. Weinstein, J. F. de Boer, H. W. Berendse, MD, “In vivo exploration of retinal nerve fiber layer morphology in Parkinson’s disease patients,” *J. Neural Transmission*, **125**, 931-936 (2018).



# 10 Acknowledgments

---

Koen, I would like to thank you as my co-promotor for your excellent contribution into my research and many fruitful discussions we had to finish this work. Your brilliant logical and critical mind taught me how to be a better researcher.

Lucas, as my promotor, I fully appreciate your educational discussions and support in guiding me through this research despite your busy schedule. I will remember you as a compassionate leader and teacher.

Johannes, I enjoyed having many discussions with you in Amsterdam. Thank you for helping me to have a better understanding of OCT systems.

Jeroen, many thanks for your support and availability in all these years. I value your contributions which have enriched my knowledge, our research and publications.

I would also like to thank all the group members of the ImPhys; Anna, Bernd, Boling, France, Hamidreza, Jaap, Jelle H, Jelle S, Jeroen K, Jeroen H, Jaap, Jianfei, Joor, Juan Pedro, Lena, Leon, Gyllion, Marco, Mohammad, Mojtaba, Nadia, Robiel, Robert B, Robert N, Robert M, Sjord, Ted, Tian, Willem, Yan and Zhang for making this experience pleasant. Jelle H, Mohammad and Robert M, I enjoyed all our discussions during the coffee time and fruitful OCT related discussions. Tom, thank you for your contributions to my research in the laser lab. A special thanks to Annelies, Mandy, Ronald and Ron for all the help and support you provided.

Much appreciation to the group members of the Rotterdam Ophthalmic Institute; Juleke and Lisette (the honored members of JBL team) thank you for all the fun and laughter we had in the office and for accepting most of my requests in picking the Irish pubs for our social events. Henk, Gijs and Robin, thank you for all the fun experiments with OCT machines and your contribution. It was fun to work with you all. Sow-Yen, thank you for all your advice during the time my daughter, Myra, was a newborn, and your help regarding work whenever I needed it. Kedir and

Jelena, I will remember all the laughter, complaints, and good times together. Aletta, Aline, Angela, Annemiek, Caroline, Elrozy, Esmá, Grzegorz, Hejan, Jetty, Karin, Laurence, Mia, Marja, Mia, Netty, Olympia, Rene, Sonia, Tessa, Susan, Stijn, Verena, and Wout, thanks for making my experience at ROI enjoyable.

Although my research mainly took place at ROI and TUDelft I always felt welcomed by my colleagues at the VU University. Joy, Max, Valentina and Jelmer, it was a great pleasure to work with you. Thank you for all your help with data preparation and experiments. Boy, Kari, Luca, Fabio, and Mathi, it was fun having you as my colleagues even for a short time.

I would like to thank my lovely parents and parents-in-law for being a great support for me in this journey.

And above all, to my lovely wife Natalie. Honey, your prayers and support are the reason that this journey is finished. I will never forget your love, care and sacrifices. You did every possible thing by taking care of our beautiful Myra and Jason to give me space to work on my thesis. This book is devoted to you and above all, our Creator.

# 11 Curriculum Vitae

---

Babak Ghafaryasl was born on in Tehran, Iran on the 6 May 1981. He obtained his BSc degree in Medical Engineering from Tehran Azad University in 2005. Later he has been working as a research Engineer in Prime Vision (Delft, the Netherlands) and Pompeu Fabra University (Barcelona, Spain). Later in 2012 he obtained his MSc degree in Electrical Engineering from Linnaeus University in Växjö, Sweden. He started his PhD in 2014 in the department of imaging physics at Delft University of Technology. His project was on optical and structural characteristics of chrioretinal tissues, described in this thesis.

Since September 2018 he has been working as a scientific consultant and data scientist in Alten, seismic imaging group of Shell, and recently, in EUV projection group of ASML.